AFRL-OSR-VA-TR-2015-0131

MULTI-STABLE MORPHING CELLULAR STRUCTURES

Dennis McLaughlin
PENNSYLVANIA STATE UNIVERSITY

05/21/2015
Final Report

Air Force Research Laboratory
AF Office Of Scientific Research (AFOSR)/ RTA
Arlington, Virginia 22203
Air Force Materiel Command

REPORT DOCUMENTATION PAGE

Form Approved
OMB No. 0704-0188

PLEASE DO NOT RETURN YOUR FORM TO THE ABOVE ORGANIZATION.

1. REPORT DATE *(DD-MM-YYYY)*	2. REPORT TYPE	3. DATES COVERED *(From - To)*
05-14-2015	Final Report	08-15-2011 to 02-14-2015

4. TITLE AND SUBTITLE
Multi-Stable Morphing Cellular Structures

5a. CONTRACT NUMBER

5b. GRANT NUMBER
FA9550-11-1-0159

5c. PROGRAM ELEMENT NUMBER

6. AUTHOR(S)
Prof. Dennis K. McLaughlin (Pennsylvania State University)

5d. PROJECT NUMBER

5e. TASK NUMBER

5f. WORK UNIT NUMBER

7. PERFORMING ORGANIZATION NAME(S) AND ADDRESS(ES)
Pennsylvania State University
408 Old Main, University Park, PA 16802

8. PERFORMING ORGANIZATION REPORT NUMBER

9. SPONSORING/MONITORING AGENCY NAME(S) AND ADDRESS(ES)
Air Force Office of Scientific Research
875 N. Randolph Street, Room 3112, Arlington, VA 22203

10. SPONSOR/MONITOR'S ACRONYM(S)
AFOSR/ David Stargel

11. SPONSOR/MONITOR'S REPORT NUMBER(S)

12. DISTRIBUTION/AVAILABILITY STATEMENT
Unlimited

13. SUPPLEMENTARY NOTES
The PI at the start of the grant was Prof. Farhan Gandhi. In Aug 2012, Prof. Gandhi moved to Rensselaer Polytechnic Institute, and Prof. Dennis McLaughlin of Penn State took over as Administrative PI. A sub-contract was issued to Rensselaer for Prof. Gandhi to continue his work.

14. ABSTRACT
The first couple of years of the project focused primarily on three distinct areas. First, on experiments and numerical models toward a fundamental understanding of snap-through behavior of "cosine" arches. Second, on a demonstration of use of bi-stable elements in chord morphing applications. And third, on modeling an experiments focusing on the actuation of bi-stable von-Mises trusses using Shape Memory Alloys. Over the final phase, the project has focused on two specific areas. On the application side, a design of a span morphing system using bi-stable elements was developed, and demonstrated in an experiment. Furthermore, pneumatic artificial muscles were integrated in the unit cell of the cellular lattice for the purpose of modulus variation in one principle direction or another. Through analysis and experiment, the best unit cell geometric parameters that produced the largest change in modulus were identified. It was shown that maximum increase in modulus could be achieved by pressurizing either of the orthogonal muscle sets, rather than all the muscles simultaneously. The difference in mechanism by which modulus change was realized when pressurizing one set of muscles, or the orthogonal set, were identified

15. SUBJECT TERMS

16. SECURITY CLASSIFICATION OF:			17. LIMITATION OF ABSTRACT	18. NUMBER OF PAGES	19a. NAME OF RESPONSIBLE PERSON
a. REPORT	b. ABSTRACT	c. THIS PAGE			Prof. Dennis McLaughlin
U	U	U	UU		19b. TELEPHONE NUMBER *(Include area code)* 814-865-2560

Reset

INSTRUCTIONS FOR COMPLETING SF 298

1. REPORT DATE. Full publication date, including day, month, if available. Must cite at least the year and be Year 2000 compliant, e.g. 30-06-1998; xx-06-1998; xx-xx-1998.

2. REPORT TYPE. State the type of report, such as final, technical, interim, memorandum, master's thesis, progress, quarterly, research, special, group study, etc.

3. DATES COVERED. Indicate the time during which the work was performed and the report was written, e.g., Jun 1997 - Jun 1998; 1-10 Jun 1996; May - Nov 1998; Nov 1998.

4. TITLE. Enter title and subtitle with volume number and part number, if applicable. On classified documents, enter the title classification in parentheses.

5a. CONTRACT NUMBER. Enter all contract numbers as they appear in the report, e.g. F33615-86-C-5169.

5b. GRANT NUMBER. Enter all grant numbers as they appear in the report, e.g. AFOSR-82-1234.

5c. PROGRAM ELEMENT NUMBER. Enter all program element numbers as they appear in the report, e.g. 61101A.

5d. PROJECT NUMBER. Enter all project numbers as they appear in the report, e.g. 1F665702D1257; ILIR.

5e. TASK NUMBER. Enter all task numbers as they appear in the report, e.g. 05; RF0330201; T4112.

5f. WORK UNIT NUMBER. Enter all work unit numbers as they appear in the report, e.g. 001; AFAPL30480105.

6. AUTHOR(S). Enter name(s) of person(s) responsible for writing the report, performing the research, or credited with the content of the report. The form of entry is the last name, first name, middle initial, and additional qualifiers separated by commas, e.g. Smith, Richard, J, Jr.

7. PERFORMING ORGANIZATION NAME(S) AND ADDRESS(ES). Self-explanatory.

8. PERFORMING ORGANIZATION REPORT NUMBER. Enter all unique alphanumeric report numbers assigned by the performing organization, e.g. BRL-1234; AFWL-TR-85-4017-Vol-21-PT-2.

9. SPONSORING/MONITORING AGENCY NAME(S) AND ADDRESS(ES). Enter the name and address of the organization(s) financially responsible for and monitoring the work.

10. SPONSOR/MONITOR'S ACRONYM(S). Enter, if available, e.g. BRL, ARDEC, NADC.

11. SPONSOR/MONITOR'S REPORT NUMBER(S). Enter report number as assigned by the sponsoring/ monitoring agency, if available, e.g. BRL-TR-829; -215.

12. DISTRIBUTION/AVAILABILITY STATEMENT. Use agency-mandated availability statements to indicate the public availability or distribution limitations of the report. If additional limitations/ restrictions or special markings are indicated, follow agency authorization procedures, e.g. RD/FRD, PROPIN, ITAR, etc. Include copyright information.

13. SUPPLEMENTARY NOTES. Enter information not included elsewhere such as: prepared in cooperation with; translation of; report supersedes; old edition number, etc.

14. ABSTRACT. A brief (approximately 200 words) factual summary of the most significant information.

15. SUBJECT TERMS. Key words or phrases identifying major concepts in the report.

16. SECURITY CLASSIFICATION. Enter security classification in accordance with security classification regulations, e.g. U, C, S, etc. If this form contains classified information, stamp classification level on the top and bottom of this page.

17. LIMITATION OF ABSTRACT. This block must be completed to assign a distribution limitation to the abstract. Enter UU (Unclassified Unlimited) or SAR (Same as Report). An entry in this block is necessary if the abstract is to be limited.

Multi-Stable Morphing Cellular Structures (FA9550-11-1-0159)
Final Report, May 14, 2015

Farhan Gandhi

Professor, and Rosalind and John J. Redfern Jr. '33 Endowed Chair in Aerospace Engineering
Department of Mechanical, Aerospace and Nuclear Engineering, JEC Building, Room 5002
Rensselaer Polytechnic Institute, Troy, NY 12180, USA
Tel: (518) 276-3244, E-mail: fgandhi@rpi.edu

Over a period of 42 months (Aug 15, 2011 – Feb 14, 2015), a number of specific tasks were undertaken during the execution of this project. Broadly, they are categorized in the list below:

1. Experiments and numerical models toward a fundamental understanding of snap-through behavior of "cosine" arches.
2. Demonstration of use of bi-stable elements in chord morphing and span morphing applications, through modeling and experiments.
3. Actuation of bi-stable von-Mises trusses using Shape Memory Alloys – modeling and experimental validation.
4. Stiffness variation of cellular structures using pneumatic artificial muscle inclusions – fundamental analysis, experiments and parametric design studies to understand the possible changes in modulus in a specific direction and the impact of unit cell parameters and muscle states.

The results are presented in detail in the following papers:

Conference Proceedings:

C1. Pontecorvo, M., Barbarino, S., Murray, G., and Gandhi, F., "Bi-Stable Arches for Morphing Applications," 22nd International Conf. on Adaptive Structures and Technologies, Corfu, Greece, October 10-12, 2011.

C2. Moser, P., Barbarino, S., and Gandhi, F., "Helicopter Rotor Blade Chord Extension Morphing using a Centrifugally Actuated von-Mises Truss," Proceedings of the ASME 2012 Conference on Smart Materials, Adaptive Structures and Intelligent Systems, SMASIS2012, Sept. 19-21, 2012, Stone Mountain, Georgia, SMASIS2012-8053.

C3. Barbarino, S., Gandhi, F., and Visdeloup, R., "A Bi-Stable von-Mises Truss for Morphing Applications actuated using Shape Memory Alloys," Proceedings of the ASME 2013 Conference on Smart Materials, Adaptive Structures and Intelligent Systems, SMASIS2013, Sept. 16-18, 2013, Snowbird, Utah, SMASIS2013-3062.

C4. Barbarino, S., and Gandhi, F., "Shape Memory Alloy Actuated Morphing Cellular Frame using Bi-stable von-Mises Trusses with Variable Length Links," 22nd AIAA/ASME/AHS Adaptive Structures Conference at SciTech2014, Jan. 13-17, 2014, National Harbor, Maryland.

C5. Pontecorvo, M., Niemiec, R., and Gandhi, F., "Variable modulus cellular structures using pneumatic artificial muscles," Proceedings of the 2009 SPIE Conference on Smart Structures and Materials, San Diego, California, Mar. 9-13, 2014.

C6. Pontecorvo, M., Niemiec, R., and Gandhi, F., "Design studies on cellular structures with pneumatic artificial muscles for modulus variation," 25th Int. Conf. on Adaptive Structures and Technologies, Den Haag, The Netherlands, Oct. 6-8, 2014.
C7. Misiorowski, M., Pontecorvo, M., and Gandhi, F., "A Bi-Stable System for Rotor Span Extension in Rotary-Wing Micro Aerial Vehicles," 23rd AIAA/ASME/AHS Adaptive Structures Conference, AIAA Science and Technology Forum 2015, Jan 5-9, 2015, Kissimmee, Florida.
C8. Pontecorvo, M., Niemiec, R., and Gandhi, F., "Stiffness Control with Pneumatic Artificial Muscle Inclusions in a Cellular Honeycomb Unit," 23rd AIAA/ASME/AHS Adaptive Structures Conference, AIAA Science and Technology Forum 2015, Jan 5-9, 2015, Kissimmee, Florida.

Journal Papers:

J1. Pontecorvo, M., Barbarino, S., Murray, G., and Gandhi, F., "Bi-Stable Arches for Morphing Applications" *Journal of Intelligent Material Systems and Structures*, Vol. 24, No. 3, Feb 2013, DOI: 10.1177/ 1045389X12457252.
J2. Moser, P., Barbarino, S., and Gandhi, F., "Helicopter Rotor Blade Chord Extension Morphing using a Centrifugally Actuated von-Mises Truss," *Journal of Aircraft*, Vol. 51, No. 5 (2014), pp. 1422-1431. doi: 10.2514/1.C032299.

In addition, extended versions of papers C3, C6 and C7 were submitted to *Journal of Intelligent Material Systems and Structures*. Reviews have been received and the manuscripts revisions are being made for resubmission to the journal.

The articles J1, J2, C3, C6 and C7 are appended, and adequately describe the efforts under categories 1–4 (listed in the first paragraph) for this final report.

Article

Journal of Intelligent Material Systems and Structures

Journal of Intelligent Material Systems and Structures
24(3) 274–286

DOI: 10.1177/1045389X12457252
jim.sagepub.com
SAGE

Bistable arches for morphing applications

Michael E Pontecorvo, Silvestro Barbarino, Gabriel J Murray and Farhan S Gandhi

Abstract

This article examines the bistable behavior of an arch for morphing applications. The arch has a cosine profile, is clamped at both ends, and is restrained axially by a spring at one end. Fabrication and testing of several Delrin and NiTiNOL arch specimens (with varying arch height, thickness, and spring stiffness) were followed by ANSYS finite element modeling, and the ANSYS simulation results showed good overall agreement with the test results. A parametric study was conducted using the ANSYS model to assess the influence of arch thickness, height, and spring stiffness on the bistable behavior. The results indicated that lower arch thickness, larger arch height, and higher spring stiffness tend to promote bistability; lower arch thickness and height reduce peak strains as the arch moves between equilibrium states, but increasing spring stiffness has a smaller effect; and higher arch thickness, height, and spring stiffness increase the snap-through force, which in turn increases the actuation force requirement as well as load carrying capability of the bistable morphing arch. If the arch slenderness ratio is unchanged, change in arch span (size) does not change the maximum stress while increasing the peak snap-through force proportionally.

Keywords

Morphing, bistable arches, snap-through, finite elements, shape memory alloy, Delrin

Introduction

Bistable or multistable structures, which can undergo large deformation as they transition between two or more stable equilibrium positions, are of significant interest in morphing applications. A very attractive feature of such structures is that the equilibrium positions require neither any power nor any locking mechanisms to hold (Dano and Hyer, 2001). By coupling bistable structural elements to actuators to induce shape change, morphing systems or subsystems can be synthesized.

Elastic arches are classic examples of structures that can exhibit bistability. The buckling and/or bistable behavior of elastic arches has been extensively studied. The stability of elastic arches under static loading was first investigated by Timoshenko (1936). Timoshenko developed equations for the critical snap-through load of elastic arches for both symmetric and asymmetric buckling modes. Other researchers (Cheung and Babock, 1970; Fung and Kaplan, 1952; Gjeslvik and Bodner, 1962; Hoff and Bruce, 1953; Lock, 1966) also developed equations to predict the critical snap-through load and force–displacement behavior of arches. The arches investigated have been either circular or sinusoidal in shape and either clamped or pinned at their endpoints.

Gjeslvik and Bodner (1962), Fung and Kaplan (1952), and Cheung and Babock (1970) all conducted knife-edge loading experiments on elastic arches. However, Gjeslvik and Bodner were the only researchers to experimentally obtain force–displacement data for the arches in the negative stiffness region of the curve. Fung and Kaplan also performed a design study testing the effects of thickness to height ratio and spring stiffness on critical buckling load and arch stresses. It should be noted that although the arches in these studies snapped-through, they did not exhibit bistability. The primary focus of the researchers was accurately predicting the critical buckling load of the arches.

In addition to analytical studies and experiments, finite element simulations have also been used in the study of elastic arches. One of the earliest such studies was by Walker (1969). Pi and Trahair (1998) compare their finite element results to those from other

Mechanical, Aerospace and Nuclear Engineering, Rensselaer Polytechnic Institute, Troy, NY, USA

Corresponding author:
Michael E Pontecorvo, Mechanical, Aerospace and Nuclear Engineering, Rensselaer Polytechnic Institute, JEC 5002, Troy, NY 12180, USA.
Email: pontem@rpi.edu

researchers and in doing so provide a good summary of the computational work relating to elastic arches. Again, these studies generally focused on estimating the critical snap-through loads for pinned or clamped circular and sinusoidal arches.

Over the last decade, researchers have started to focus on the use of bistable structures for morphing applications. Schultz and Hyer (2004) examined morphing of unsymmetric composite laminates under piezoelectric actuation and later followed it up with experimental verification (Schultz et al., 2006). Schultz (2008) also developed a bistable device for potential application to wing twist morphing. At the University of Bristol, Diaconu et al. (2007) considered various approaches to using bistability for morphing airfoil and wing sections. Figure 1 shows a concept proposed in their study for wing chord morphing. Their efforts were continued by Daynes et al. (2009), Panesar and Weaver (2010), who focused on the development of a bistable trailing-edge flap, and Daynes et al. (2011), who focused on multistable engine air inlets.

Bistable elastic arches have also been considered for helicopter rotor blade morphing in recent studies by Johnson et al. (2009, 2010). In these studies, the researchers envisioned using a single bistable elastic arch to effectively extend the chord of a rotor blade. Figure 2 is a schematic of the concept. In this study, the arch was clamped at both ends, and much effort was devoted to the design of flexures to avoid high strains leading to failure when the arch transitioned from one stable equilibrium condition to the other. Furthermore, the designed arch with flexures was fabricated, and its force versus displacement behavior was experimentally determined and used to validate the ABAQUS finite element results.

As with Johnson et al. (2009, 2010), the present study focuses on bistable arches for morphing applications. However, rather than elaborately designing flexures, a novel cosine profile is considered, which can reduce peak stresses in the arch. Such bistable arches could be used either as individual morphing elements (e.g. similar to Figure 2) or as elements in multistable morphing honeycomb-like cellular structures. An example of a multistable cellular honeycomb-like structure with the cosine bistable arches is shown in Figure 3(a) configured for chord extension morphing of a helicopter rotor blade. Figure 3(b) is a top view of the same concept. The top illustration shows the cellular honeycomb in the retracted, first equilibrium state, while the bottom illustration depicts it in the extended alternate equilibrium state. In the present article, arches based on this cosine profile are fabricated, and their bistable behavior is examined under a quasi-static controlled displacement input. The experimental data are used to validate ANSYS finite element simulation results, and the validated finite element model is further used in a parametric design study to assess the impact of the arch's geometric parameters on its bistable behavior.

Modeling

The elastic arch considered in this article is defined by the cosine profile in equation (1), depicted schematically in Figure 4

$$y = \frac{\theta l}{2}\left(1 - \cos\left(\frac{2\pi x}{l - 2\lambda l}\right)\right) \tag{1}$$

A cosine profile is chosen because it creates an arch whose endpoints have zero slope, which reduces maximum local stresses in the arch as it transitions from one stable equilibrium position to the other; y is the vertical coordinate of the arch, x is the horizontal coordinate, l is the span of the arch, and θl defines the height of the arch. To further reduce maximum local stresses in the

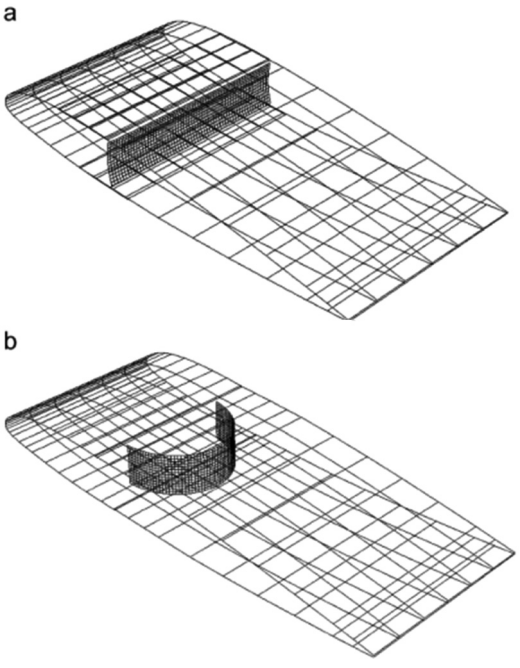

Figure 1. Bistable composite plate used for chord extension (a) retracted (b) extended (Diaconu et al., 2007).

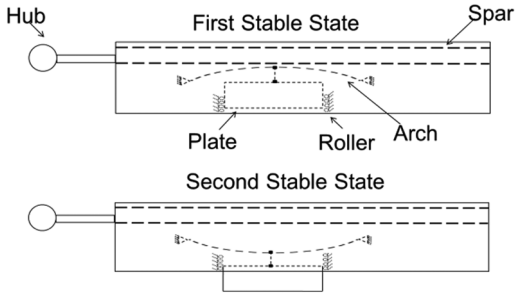

Figure 2. Top view of bistable arch used for chord extension (Johnson et al., 2010).

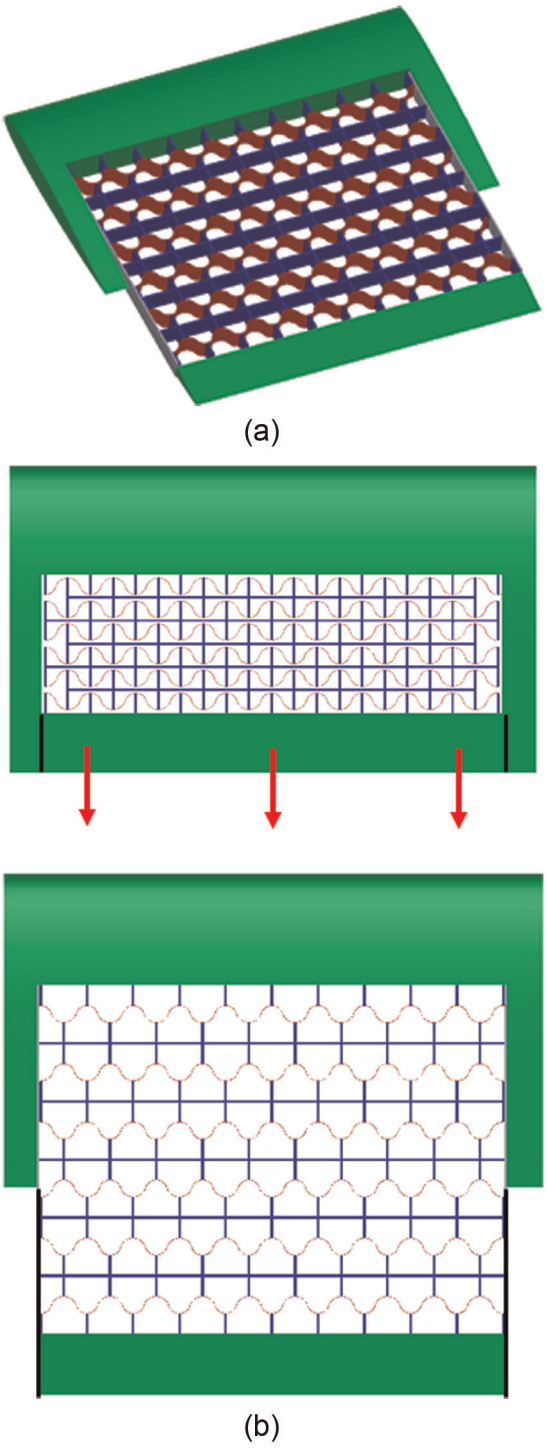

Figure 3. (a) Isometric view of bistable arches used for chord extension and (b) top view of bistable arches used for chord extension.

arch, a horizontal section of material of length λl is added to either side of the cosine curve. It should be noted that introduction of the section of length λl is also beneficial to the convergence of the ANSYS finite element model. Throughout the analysis, λ has a constant value of 0.05. The thickness of the arch is t, and the width of the arch is b. The left-hand side of the arch

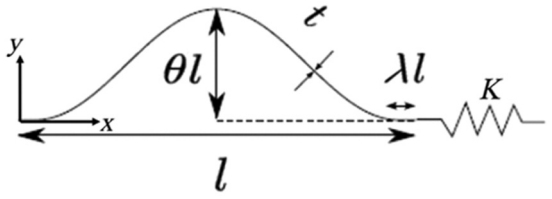

Figure 4. Schematic of the elastic arch model.

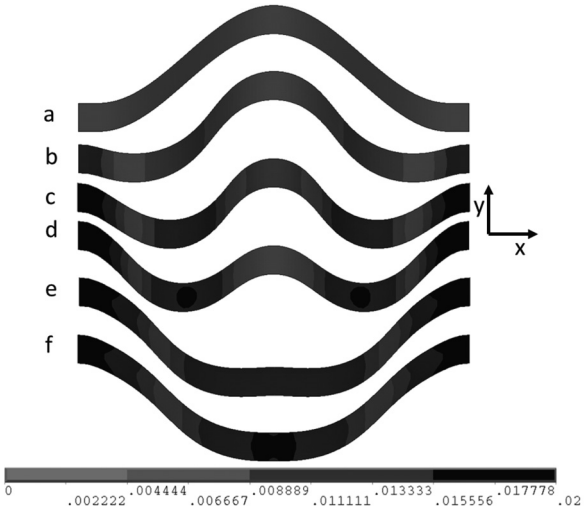

Figure 5. Symmetrical deformation of the arch (surface bending strains).

is clamped. The right-hand side of the arch is allowed to move in the x direction, while being restrained by a spring of stiffness K. A sufficiently stiff spring ensures bistability, while a spring that is too soft (vis-à-vis the arch) does not provide enough of an energy barrier to prevent the arch from springing back to the initial state on removal of the load.

Bistable behavior of cosine elastic arch

Figure 5 depicts the progression of arch deformation from one stable equilibrium position to the other. The scale in the figure represents strain level, with light gray corresponding to the lowest strains and black to the largest strains. Flexural bending, rather than axial compression, is the dominant mode of deformation in the arch. One of the main challenges associated with the arch is avoiding the large strains caused by bending.

Figure 6(a) illustrates the typical force versus displacement behavior of the bistable cosine elastic arch. The x-axis of the figure corresponds to the vertical displacement of the midpoint of the arch, positive downward. The y-axis corresponds to the vertical force required to hold the midpoint of the arch at that position. Figure 6(b) shows the corresponding strain energy in the system versus arch position. The lettered positions in Figure 5 correspond to the labeled points in Figure 6,

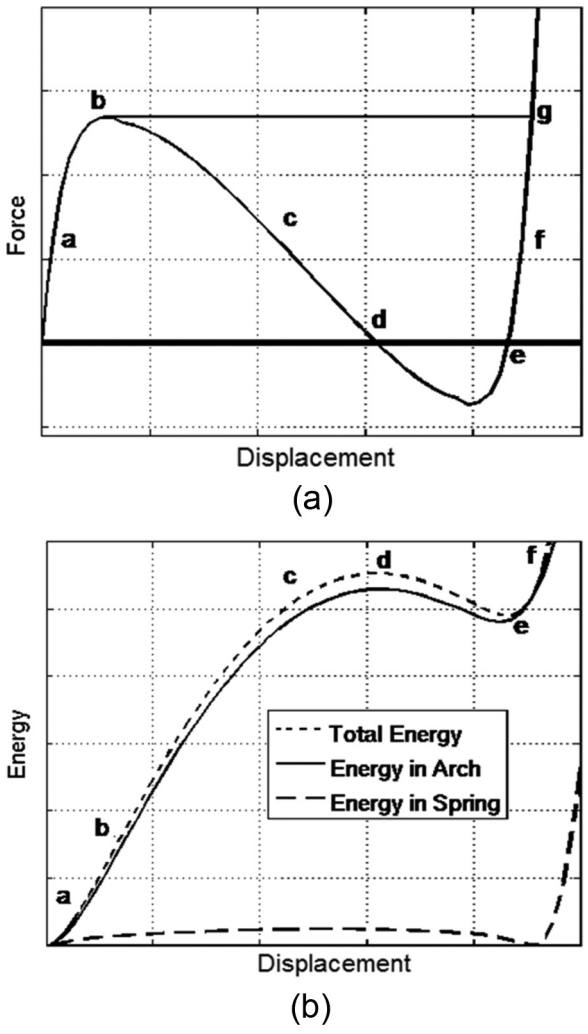

Figure 6. (a) Force versus displacement behavior of the cosine bistable elastic arch and (b) energy versus displacement behavior of the cosine bistable elastic arch.

with the origin and the point e on Figure 6 corresponding to the two stable equilibrium positions.

The arch can be moved between equilibrium positions in two ways. One way is to apply an increasing force to the midpoint of the arch. When force controlled, the curve in Figure 6(a) begins in its first equilibrium state and travels up the positive slope region around point a, to a maximum at point b. Once the force reaches point b, the arch snaps-through to point g at a constant force (along the straight line a–g). At this point, the force can be released and the arch will settle in its second equilibrium position at point e.

The second way to move the arch between equilibrium positions is to control the displacement of the midpoint of the arch. Under displacement control, the arch does not snap from point b to point g. Instead, the curve enters the region around point c. Here, the slope of the curve becomes negative, with the force required for increasing levels of deformation actually decreasing. At point d, the arch reaches an unstable equilibrium state, and immediately beyond point d, the force required is negative, indicating that the arch must actually be held back from naturally rushing toward the second stable equilibrium point e. It is in this negative force part of the curve that the stored energy in the spring and in the bending of the arch is being released. To move the arch beyond the point e into the region marked by point f would again require an increasing positive force. The experiments and simulations in this article only consider the elastic arch under displacement control inputs. Even though the arch does not snap-through per se, but rather travels along the negative stiffness portion of the force/displacement curve, the term "snap-through force" may still be used as a metric, since it provides an indication of both the load carrying capability of the arch at the equilibrium position and the magnitude of the actuation force required to morph the arch from one state to the other.

It should also be noted that while Figure 6(a) and (b) represents the behavior of a bistable arch, if the restraining spring stiffness is lower than a certain threshold (vis-à-vis the arch stiffness), the arch may snap-through but may not be bistable. In such a case, the negative stiffness portion in Figure 6(a) would still be present, but the region of the curve between points d and e would be above the x-axis, and there would be no energy minima corresponding to point e in Figure 6(b). Under force control, such an arch would snap-through but then return to the undeformed state on removal of the load. Further reduction in spring stiffness would eliminate snap-through behavior as well.

ANSYS model

The arch shown in Figure 4 is modeled using the finite element software ANSYS. The arch geometry is defined by 100 evenly spaced points, known as keypoints in ANSYS, that satisfy equation (1). This is equivalent to using 100 elements to model the arch. In the current study, BEAM3 elements were used. Although the cosine arch is represented in a piecewise linear manner with the BEAM3 elements, it was ascertained that the simulation results were very similar to those obtained using SHELL181 elements, at a lower computational cost and greater ease of convergence. The comparisons between results with BEAM3 and SHELL181 elements were carried out for three different geometries—a thin (0.8 mm) low ($\theta = 0.1$) arch, and two thick (3.2 mm) high arches ($\theta = 0.3$ and 0.4). For all three cases, the spring stiffness was held constant at 28,020 N/m, and Young's modulus of 200 GPa was used. A comparison between the maximum strains in the arch during snap-through showed a less than 5% difference in all cases. Thus, over the range of arch parameters studied, BEAM3 elements and SHELL181 elements produced very comparable results.

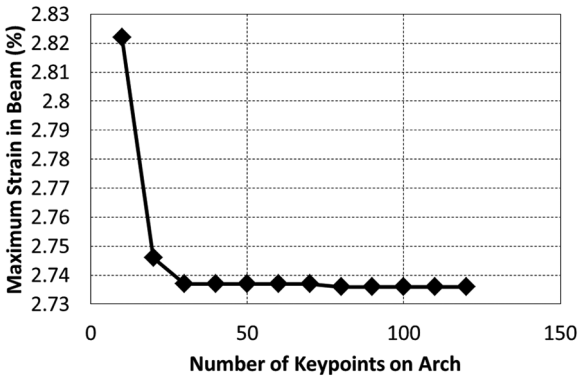

Figure 7. Convergence study of ANSYS model.

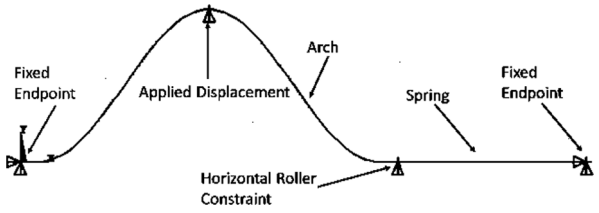

Figure 8. ANSYS arch model with boundary conditions applied.

A convergence study was also conducted to ensure that an adequate mesh size was used in the simulations. For an arch with Young's modulus of 200 GPa, spring stiffness of 28,020 N/m, thickness of 0.8 mm, and height of $\theta = 0.4$, Figure 7 shows the maximum bending strain as the arch snaps-through from one equilibrium condition to the other, versus the number of keypoints (or BEAM3 elements) used in the simulation. Clearly, the results have converged when 100 keypoints are used.

The BEAM3 elements require the initial Young's modulus, E, of the material of the arch as an input. The spring is modeled as a COMBIN14 element. All degrees of freedom of the leftmost keypoint on the arch and the rightmost keypoint on the spring are constrained to be zero. In-plane rotation and y displacement of the rightmost keypoint on the arch are also set to zero. The midpoint of the arch is constrained to move $-2\theta l$. The arch model with boundary conditions applied is shown in Figure 8.

A static, nonlinear solution with 100 substeps is used. ANSYS is provided the stress–strain curve for the arch material as an input. Initially, ANSYS calculates the stiffness of the arch based on the constant Young's modulus given to the BEAM3 elements. Then, iterations are made on the calculated local strains using the nonlinear stress–strain curve for the material to determine the correct stiffness and stress level at each point on the arch, until the program converges to a solution whereupon the force–displacement curve for the midpoint of the arch, as well as the maximum surface stress and strain at every point on the arch, is examined.

Figure 9. Delrin arches.

Experimental procedure

Arch fabrication

Preliminary simulations predicted that for reasonable values of arch thickness and height, the arch would easily undergo local strains well in excess of 0.2% as it deformed from one equilibrium state to the other. With typical metals such as steel and aluminum plastically deforming at strains greater than 0.2%, they were not considered suitable for experiments in this study. For most cases and geometries considered in this study, the maximum strains remained below 7%–8%. This led to the choice of superelastic NiTiNOL (which exhibits up to 7%–8% strain when undergoing austenite to martensite phase transformation) as a material for arch fabrication. An additional material used in the experiments in this study was Delrin because it is a polymer that has high elastic strain capability (substantially higher than NiTiNOL) and is easy to work with.

Delrin arches of varying thickness and height were waterjet cut from a 0.02-m-thick sheet of DuPont Delrin II 150SA NC010 (see Figure 9). The waterjet cut through the thickness of the sheet such that the width of every arch was the thickness of the sheet. This way, Delrin arches were produced in a one-step process. The arches had zero stress in their initial state and required no molding or heating to generate their shape. In addition, a Delrin dogbone specimen conforming to American Society for Testing Materials (ASTM) standard D638-10 was cut from the same sheet.

The superelastic NiTiNOL arches originated from strips cut from a NiTiNOL sheet on the waterjet machine. Based on the availability, the superelastic, 56.1% nickel NDC SE 508 alloy was chosen. Unlike the Delrin sheet, the NiTiNOL sheet had a much lower 5.08e−4 m thickness. Therefore, the arches were fabricated such that their thickness was the thickness of the strips cut from the NiTiNOL sheet.

After being cut, the NiTiNOL strips were bent into steel arch-shaped molds of two different geometries (arch heights) and annealed (see Figure 10 for the NiTiNOL arch specimens). A dogbone specimen conforming to ASTM standard E8/E8M-09 was also heat

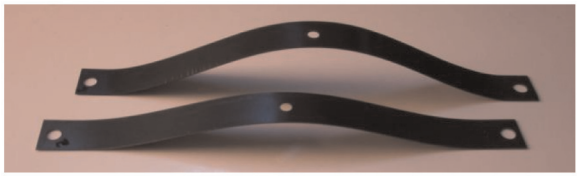

Figure 10. NiTiNOL arches.

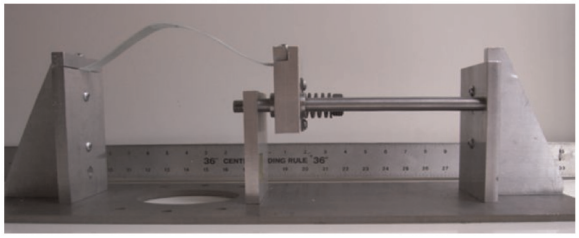

Figure 11. Arch testing fixture.

treated along with each arch. The arches were heated to approximately 500°C for between 3 and 4 min and then water quenched. The NiTiNOL arches were separately annealed, and because the process was not exactly the same both times, they exhibit different material properties.

Material characterization

In order to accurately predict the behavior of the arches using ANSYS simulation, one must input the initial Young's modulus of the arch material as well as a table of values representing the stress–strain curve for the material. To characterize these properties for Delrin and NiTiNOL, the dogbone specimens were tensile tested on an Instron Model 5866 following their respective ASTM standards.

Arch testing

The displacement-controlled bistable behavior of the Delrin and NiTiNOL arches was tested by placing them in a fixture that mimicked the boundary conditions of the model. A picture of the fixture is seen in Figure 11.

The fixture consists of a steel plate that is designed to be bolted to the base of an Instron machine. A fixed support clamps the left side of the arch in place. The right side of the arch is clamped in a similar manner to a second support. This second support is mounted on two steel rods by a set of linear ball bearings such that it is free to slide in the horizontal direction. Through the middle of the right support runs a fixed threaded rod. Threaded onto that rod is a spring. One end of the spring is fixed to the rod, while the other end is bolted to the right support. As the right support slides in the horizontal direction, the spring deforms exactly like the spring in the model.

The midpoint displacement of the arch is controlled by an Instron Model 5811 machine. Figure 12 shows a schematic representation of the setup. The fixture

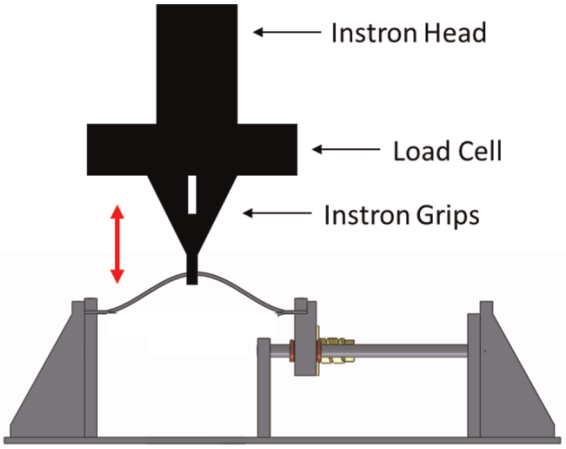

Figure 12. Diagram of the arch test setup.

holding the arch is bolted to the base of the Instron machine. A 445-N load cell is bolted to the moving head of the Instron. The load cell is connected via a bolt to the midpoint of the arch. The double-headed arrow in the diagram indicates the motion of the Instron head.

One limitation of this setup is that it does not allow the midpoint of the arch to move in the horizontal direction as it would in the model. The springs used in the test, however, are very stiff compared to the arch, minimizing rightward motion of the midpoint of the arch. Observations during testing reveal that constraining motion of the midpoint in the horizontal direction does not adversely affect the symmetric deformation of the arch. This observation is confirmed by the conclusions reached in the parametric study (section "Parametric study"), which show that the springs used in the test were stiff enough that they approached the condition of a rigid boundary.

Another possible source of error in this setup is the presence of small initial stresses in the arch. For every test, the two supports were placed exactly 0.2032 m apart. Although the arches were all designed to have that span, small imperfections in the arch fabrication, as well as spring-back after heat treatment in the NiTiNOL arches, may have altered the unstressed span of the arches. When placed in the fixture, it is possible that the difference between actual and intended spans slightly prestressed the arches. Arch height was measured after each arch was placed in the fixture.

The arch test matrix is presented in Table 1. The parameter combinations chosen for testing were intended to help validate the ANSYS simulation over a range of values. Nominal arch heights of $\theta = 0.1$ and $\theta = 0.2$ were tested. Most specimens were tested with a spring stiffness of 140,101 N/m, but one Delrin specimen was also tested at a lower spring stiffness of 28,020 N/m. Each cell in the matrix contains the specimen designation followed by the thickness of the specimen in millimeter.

Table 1. Arch test matrix

θ	Arch material and spring stiffness		
	Delrin		NiTiNOL
	140,101 N/m	28,020 N/m	140,101 N/m
0.1	D4: 1.6	—	HT-2: 0.5
0.2	D2: 2.5	D1: 1.4	HT-1: 0.5
	D3: 2.2	—	—

Specimen designation: thickness in millimeter.

Each arch was moved from 0 to approximately $2\theta l$m of vertical midpoint deflection, with the test repeated up to four times. For all cases, the Instron head was moved at low, constant rate of 0.0508 m/min so as to minimize inertial effects and maintain the quasi-static loading condition. Data were collected at a frequency of 2 Hz.

Experimental results and validation

Material characterization results

Tensile test results on the Delrin dogbone specimen are presented in Figure 13. The x-axis is percent strain and the y-axis is stress in megapascal. Three curves are plotted in this figure. The dashed and dotted curves represent loading and unloading up to 3% strain, whereas the solid curve represents loading to 8% strain.

Delrin, being a polymer, has a nonlinear stress–strain curve. For small strains (up to 1.5%–2%), however, the curve is relatively linear. It is from this portion of the curve that the slope is measured. The calculated slope of 3.17 GPa is the initial Young's modulus of the material input to the ANSYS finite element model. ANSYS is also given the loading and unloading curves for 3% strain. This way, ANSYS can correctly predict the stress–strain behavior of the arch when both loading and unloading.

Figures 14 and 15 display tensile test results from the two NiTiNOL dogbone specimens, denoted as HT-1 and HT-2, respectively. For NiTiNOL, only the loading curve to 8% strain is used in ANSYS. Both specimens (which differ slightly in terms of the heat treatment used) start in the austenite phase, transition to the martensite phase at nearly zero slope, and then recover stiffness in the martensite phase (although this stiffness is somewhat lower than the austenite stiffness).

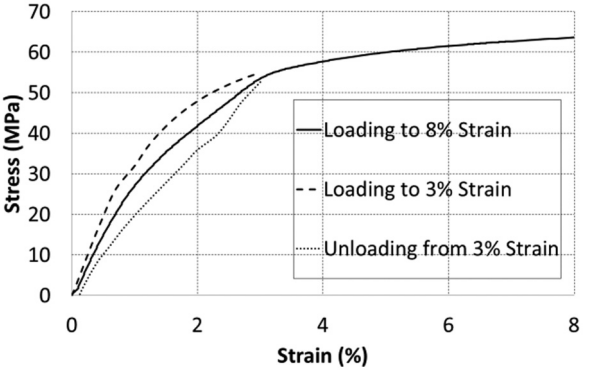

Figure 13. Delrin tensile test results.

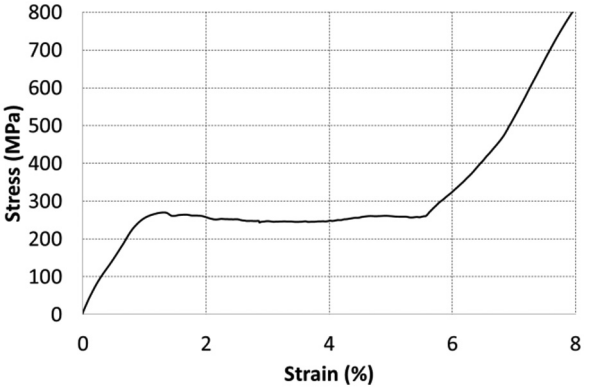

Figure 14. NiTiNOL HT-1 tensile test results.

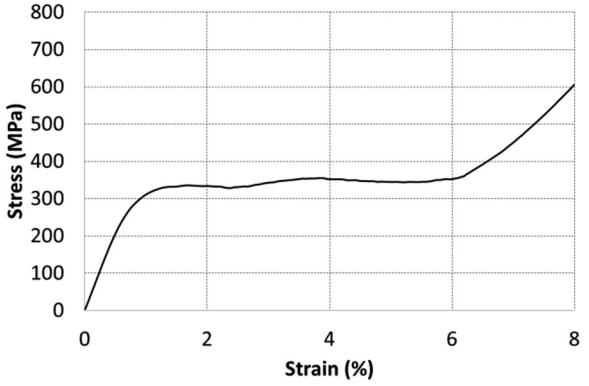

Figure 15. NiTiNOL HT-2 tensile test results.

Arch testing and simulation results

The experimental and simulation results for the bistable behavior of the Delrin arches under controlled displacement are presented in Figure 16. Each plot presents data for a single arch. The symbols correspond to experimental data from different cycles. For any cycle, only a fraction of the experimental data points are shown on the figure for improved clarity. The ANSYS finite element simulation results are plotted as solid or dashed lines.

In all cases, the experimental data show a hysteretic behavior, with variation between the loading and unloading paths in a single cycle. The loading and unloading curves converge near the beginning and end of the cycle, but diverge around the negative stiffness portion of the curve. The ANSYS simulation shows a similar trend. This hysteresis is caused by the fact that

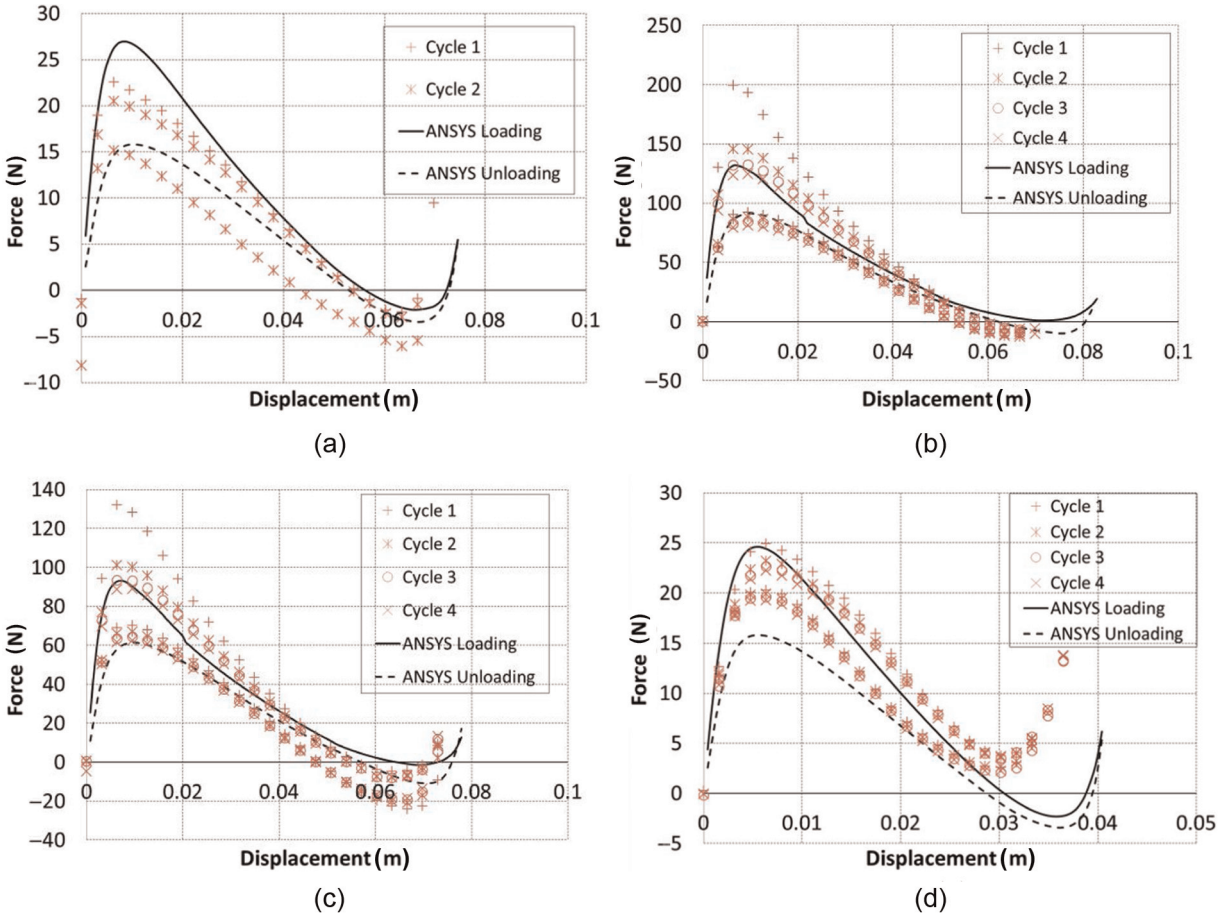

Figure 16. Delrin arch test results: (a) D1 (θ = 0.179, K = 28,020 N/m, t = 1.4 mm), (b) D2 (θ = 0.199, K = 140,101 N/m, t = 2.5 mm), (c) D3 (θ = 0.187, K = 140,101 N/m, t = 2.2 mm), and (d) D4 (θ = 0.097, K = 140,101 N/m, t = 1.57 mm).

the loading and unloading stress–strain curves of the material differ. Similar results where the experiment showed hysteresis can be found in the work of Johnson et al. (2010) and Schioler and Pellegrino (2004). Schioler and Pellegrino too attribute the hysteresis to the material they used (like the Delrin and NiTiNOL in the present study) not being perfectly elastic.

Another point to note about the Delrin arch tests is that the first experimental cycle always has the highest maximum (snap-through) force. Later cycles show a reduction in maximum force, suggesting perhaps the influence of stress relaxation in the clamped arch.

In Figure 16(a) to (c), the arches all show a bistable behavior, and even though ANSYS overpredicts the location of the second stable equilibrium position by up to 7.7%, there is good overall correlation between simulation and experiment in terms of load levels. The location of the second equilibrium position mainly depends on the arch geometry and shape. Therefore, the small discrepancy can be attributed to fabrication or the test setup not exactly reproducing the boundary conditions of the simulations. For the arch in Figure 16(d), however, the finite element simulation predicts a bistable behavior, while the experiment indicates that the arch would not exhibit bistability. Agreement in peak snap-through force between simulation and experiment and general agreement in the force–displacement behavior in the negative stiffness region at under 0.025 m displacement in Figure 16(d) suggest the possibility that the arch deformation in the experiment may not have been symmetric beyond 0.025 m. Moreover, this case corresponds to a very shallow arch, which is very sensitive to geometric or fabrication imperfections.

The experimental and simulation results for the NiTiNOL arches are plotted in Figure 17. The results for specimen HT-1 (Figure 17(a)) display similar trends to those observed in the Delrin arch results in Figure 16, with the second equilibrium position again overpredicted, in this case by 10.3%. The absence of any hysteresis in the simulation results is due to the fact that for NiTiNOL, only the experimental loading curves of the material (Figures 13 and 14) were measured and used as inputs to ANSYS. The simulation shows good overall agreement with the experimental data for the NiTiNOL HT-1 arch.

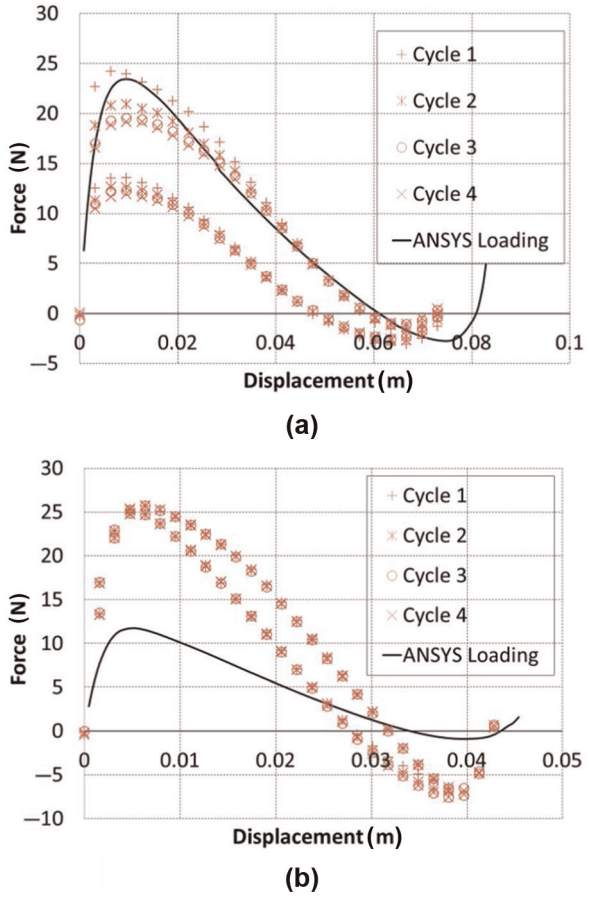

Figure 17. NiTiNOL arch test results: (a) HT-1 (θ = 0.199, K = 140,101 N/m, t = 0.5 mm) and (b) HT-2 (θ = 0.109, K = 140,101, N/m t = 0.5 mm).

Table 2. Arch parameter variations (constant spring stiffness)

Maximum strain (%)		θ			
		0.4	0.3	0.2	0.1
Thickness (mm)	0.8	2.89	2.62	1.99	0.92
	1.6	5.48	4.68	3.32	1.84
	3.2	10.60	8.84	6.66	3.68

For the second NiTiNOL arch (HT-2), the correlation between test and ANSYS simulation (Figure 17(b)) is much poorer. The minimum and maximum values of force predicted by the simulation and measured by experiment differ by 86.5%. It appears likely that the source of error lies with the experiment in this case. The arch height in Figure 17(b) is lower than that in Figure 17(a), and with other parameters (spring stiffness and arch thickness) being equal, a reduction in peak snap-through force would be expected. While this is seen to be true with the ANSYS simulation results, the experimentally measured peak forces in Figure 17(b) are surprisingly higher and comparable to those for a higher arch in Figure 17(a). Possible sources of error in the experiment include imperfect alignment between the arch midpoint and the Instron head or significant prestress in the arch.

Overall, the Delrin and NiTiNOL arch experiments indicate that the ANSYS model and simulations can provide an adequate predictive capability for the bistable behavior of the cosine arch over a wide range of parameter variations (such as arch height, thickness, material, and restraining spring stiffness).

Parametric study

Using the validated ANSYS simulation, a parametric study is conducted. Given an arch material of steel and a fixed span of 0.2032 m, the three main parameters that can be varied are the arch height (defined by the parameter θ), the arch thickness, t, and the spring stiffness, K. In all the results presented in this section, the midpoint displacement of the arch is normalized by the height of the arch. At a normalized displacement of 1, the arch midpoint is at the same vertical position as its endpoints. At a normalized displacement of 2, the arch midpoint is exactly twice the arch height from the first equilibrium position and a little beyond the second stable equilibrium position.

In the first set of parameter variations, the spring stiffness, K, is held constant at 28,020 N/m, and arch thickness, t, and height, θ, are varied. Table 2 encapsulates the three different thicknesses and four different arch heights considered, and the force–displacement behavior for these arches is presented in Figure 18. The value in each cell in Table 2 is the maximum strain in the arch as it moves from its first equilibrium position to a normalized displacement of 2. In this table, cells with a light-gray background indicate arch configurations that exhibit bistability, cells with clear background correspond to arches that exhibit snap-through behavior but not bistability, and cells with a hatched background correspond to configurations that exhibit neither snap-through behavior nor bistability. In addition to the desire for bistability for morphing applications, it is desirable for the arch to have low maximum strain as this would increase fatigue life as well as allow greater flexibility in the choice of materials for arch fabrication.

Of the three arch thickness values considered, the thickest arch does not show any bistability (Figure 18(c)). The two thinner arches (Figure 18(a) and (b)) display a bistable behavior for sufficient arch height. Based on the results in Figure 18, the thicker the arch, the greater the required arch height for it to exhibit bistability. From Figure 18(a) and (b), it is observed that the critical snap-through force increases as the arch height increases, eventually tapering off. Comparing Figure 18(a) and (b) reveals that critical snap-through

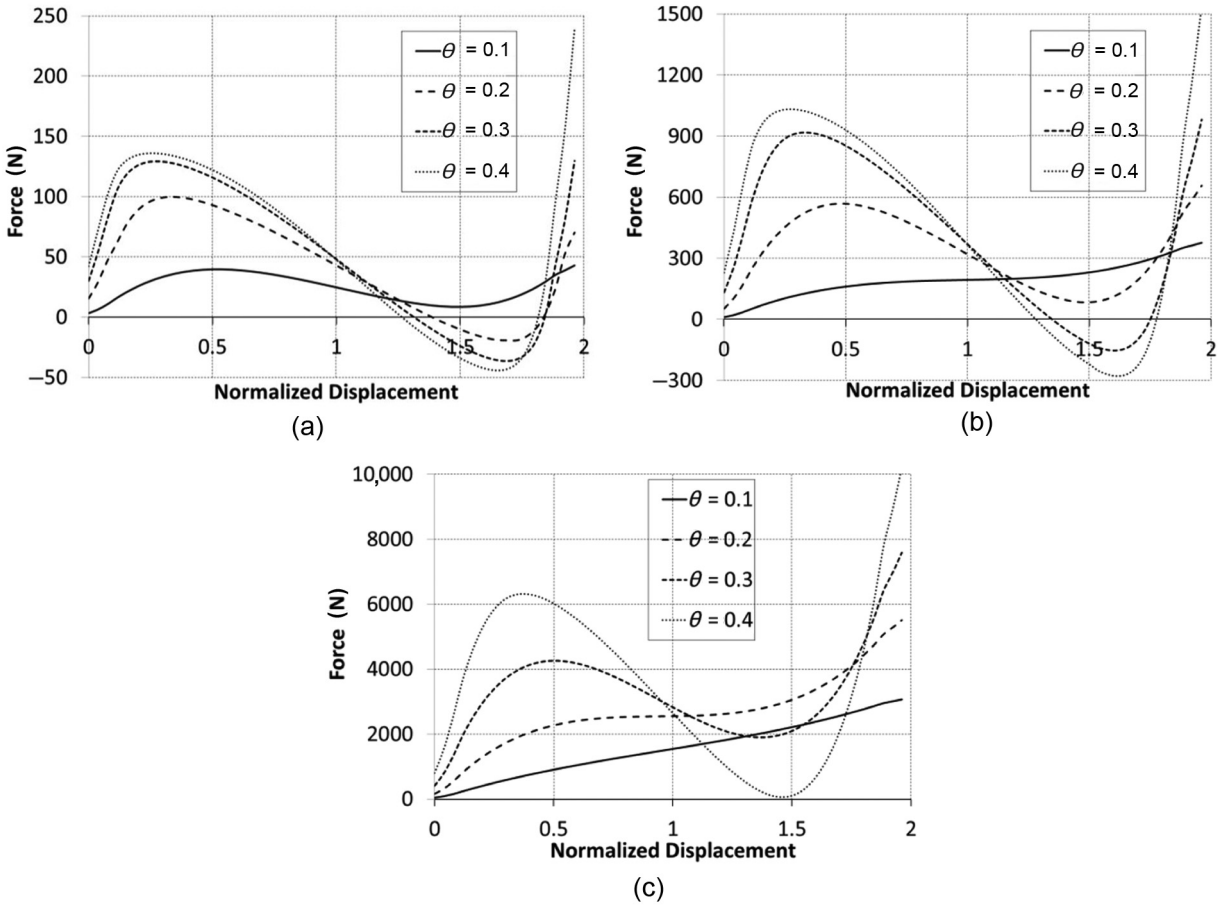

Figure 18. Behavior of cosine arches for variations in arch height and thickness (spring stiffness constant): (a) arch thickness = 0.8 mm, (b) arch thickness = 1.6 mm, and (c) arch thickness = 3.2 mm.

force also increases as the arch thickness increases. An increase in snap-through force with increasing arch height or thickness implies a higher actuation force requirement to move the arch from one equilibrium state to the other, but the stiffness and the load carrying capability in either equilibrium position also increase.

It can be seen from Table 2 that among the arches that are bistable (cells with a light-gray background), increasing thickness and arch height also increases the maximum strains in the arch. Thus, shallower, more slender arches would then be preferable from a strain and actuation force standpoint, provided they can meet the actuation stroke (shallower arches would have a smaller actuation stroke) and load carrying capability requirements.

In the second set of parameter variations, the arch thickness is held constant at 0.8 mm, while the spring stiffness, K, and arch height, θ, are varied. Table 3 encapsulates the range of stiffness values and arch heights considered, and the force–displacement behavior for these arches is presented in Figure 19.

As with Table 2, the value in each cell in Table 3 represents the maximum strain in the arch, and the fill indicates the exhibition of bistability (light-gray), snap-through behavior (clear), or neither (hatched). A comparison of Figure 19(a) to (d) indicates that the arches are more likely to exhibit bistability as the spring stiffness increases. Thus, with a soft spring in Figure 19(a), only the high arches ($\theta = 0.2$ and 0.3) are bistable, but with increasing spring stiffness (see Figure 19(c) and (d)), even the shallow arches exhibit bistability. Increasing spring stiffness shows a large increase in snap-through force for the shallower arches and a smaller increase in snap-through force for higher arches (compare Figure 19(a) to (d)). An examination of the bistable configurations in Table 3 indicates that increasing the spring stiffness has a relatively small effect on increasing the arch strains,

Table 3. Arch parameter variations (constant thickness)

Maximum strain (%)		θ			
		0.4	0.3	0.2	0.1
K (N/m)	∞	2.99	2.70	2.15	1.21
	28,020	2.89	2.62	1.99	0.92
	10,533	2.80	2.47	1.69	0.92
	4,424	2.71	2.22	1.66	0.92

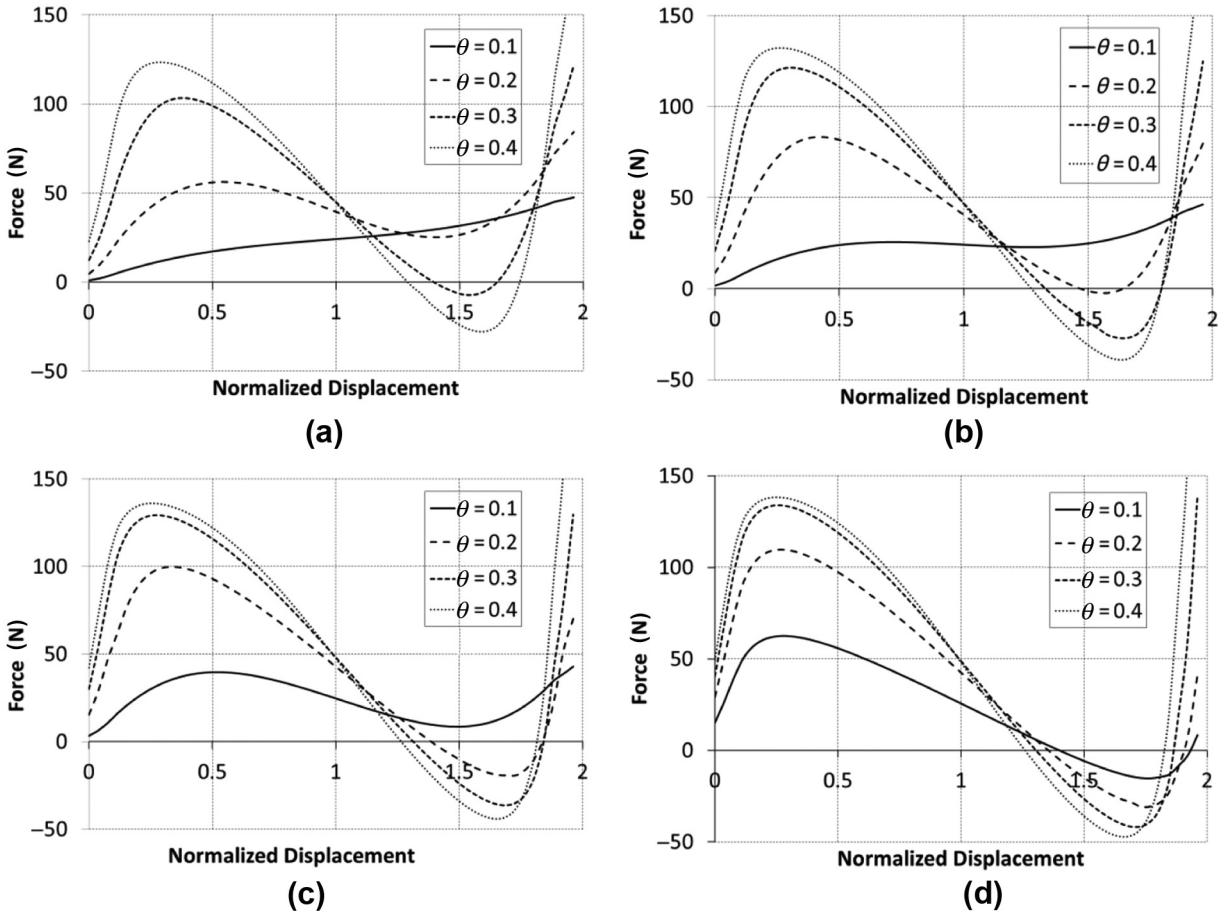

Figure 19. Behavior of cosine arches for variations in arch height and spring stiffness (arch thickness constant): (a) K = 4424 N/m, (b) K = 10,533 N/m, (c) K = 28,020 N/m, and (d) K = rigid boundary.

much less so than increasing arch height or arch thickness do.

In a third set of parameter variations, the span of the arch is varied from 0.2032 to 1.6362 m, while the arch thickness is held constant at 0.8 mm, the arch height, θ, is held constant at 0.4, and the spring is modeled as infinitely stiff (rigid boundary). Figure 20 shows the force versus normalized displacement curves for the four span lengths. While all four cases are bistable, the snap-through force for each arch decreases by a factor of 4 each time the arch span is doubled. Also, as seen in Table 4, the maximum strain in the arch decreases by a factor of 2 when the span is doubled.

Finally, the arch span was again varied, but this time, the arch thickness was also modified such that the slenderness ratio remained unchanged. The resulting force versus normalized displacement curves are displayed in Figure 21. Again, all four cases are bistable, but each time the span doubles, the snap-through force also doubles, while the maximum strain in the arch (listed in Table 5) remains unchanged as expected.

Based on the observations reported in the previous two paragraphs, as long as the restraining spring is sufficiently stiff (so as to effectively act as a rigid boundary), the results in Table 2 hold for an arch of any span as long as the slenderness ratio is the same, and the peak snap-through forces in Figure 18 would scale directly with the change in span. It was verified that these observations hold for arches of various heights.

Table 4. Span variation (constant thickness)

Strain (%)		l (m)			
		l = 0.2032	2l	4l	8l
Thickness (mm)	t = 0.8	2.95			
	t		1.48		
	t			0.74	
	t				0.37

Conclusion

This article examines the bistable behavior of an arch for morphing applications. The arch has a cosine profile, is clamped at both ends, and is restrained axially by a spring at one end. Several Delrin and NiTiNOL arch

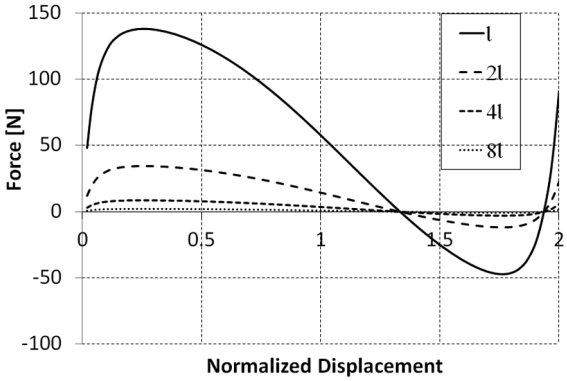

Figure 20. Bistable behavior of cosine arches for variations in arch span (arch thickness, height, and spring stiffness held constant).

Table 5. Span variation (increasing thickness)

Strain (%)		l (m)			
		l = 0.2032	2l	4l	8l
Thickness (mm)	*t* = 0.8	2.95			
	2*t*		2.95		
	4*t*			2.95	
	8*t*				2.95

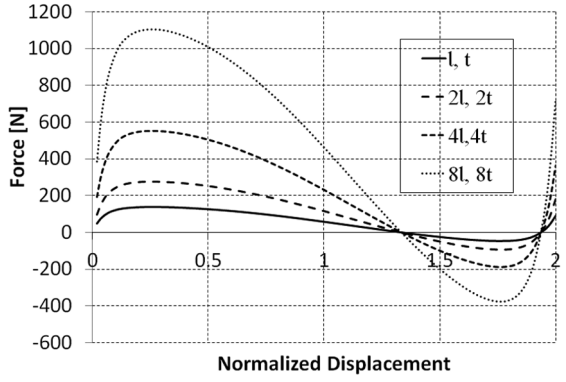

Figure 21. Bistable behavior of cosine arches for variations in arch span (increasing arch thickness, arch height, and spring stiffness held constant).

specimens were fabricated and tested under a controlled displacement input in an Instron machine. The specimens tested varied in height and thickness and used two different spring stiffnesses. An ANSYS finite element model of the arch was set up, and the simulation results showed good overall agreement with the experimental results. The validated ANSYS model was subsequently used to conduct parametric studies to assess the influence of arch thickness, height, span, and spring stiffness on the bistable behavior. From the simulation results, the following observations could be made:

1. Slender arches tend to show bistability, but as the arch thickness increases, a larger arch height is generally required for bistability.
2. Larger spring stiffness tends to lead to bistability, but as the restraining spring softens, a larger arch height is required for bistability.
3. Increasing arch height, thickness, and spring stiffness increases the snap-through force, not only indicating larger actuation force requirement to morph but also providing higher stiffness and load carrying capability in the two equilibrium states.
4. Increasing arch height and thickness also increases the maximum strains in the arches as they transition from one equilibrium position to the other. In comparison, increasing spring stiffness results in relatively small increases in maximum strain.
5. Thus, of the arches that do exhibit bistability, lower arch height and thickness would be preferable to reduce strain (increasing the range of usable materials and improving fatigue life) and morphing actuation force requirement. If required, higher spring stiffness could be used to increase the load carrying capability of the arch, although this would increase the morphing actuation force requirement as well.
6. While lower arch height leads to lower maximum strains and actuation force, it results in a smaller morphing stroke for a given arch length.
7. For a stiff spring restraint, increasing arch span while holding the slenderness ratio constant results in no change in maximum stress, while the peak snap-through force increases directly.
8. An understanding of the influence of parameter variations on the different metrics allows for the design of a bistable arch to meet morphing requirement specifications.

References

Cheung MC and Babock CD Jr (1970) An energy approach to the dynamic stability of arches. *Journal of Applied Mechanics* 37: 1012–1018.

Dano ML and Hyer MW (2001) Snap-through of unsymmetric fiber reinforced composite laminates. *International Journal of Solids and Structures* 39(1): 175–198.

Daynes S, Nall SJ, Weaver PM, et al. (2009) On a bistable flap for an airfoil. In: *AIAA structures, structural dynamics, and materials conference*, 4–7 May 2009, Palm Springs, California.

Daynes S, Weaver PM and Trevarthen JA (2011) A morphing air inlet with multiple stable shapes. *Journal of Intelligent Material Systems and Structures* 22: 961–973.

Diaconu CG, Weaver PM and Mattonni F (2007) Solutions for morphing airfoil sections using bistable laminated composite structures. In: *AIAA structures, structural dynamics, and materials conference*, 23–26 April 2007, Honolulu, Hawaii.

Fung YC and Kaplan A (1952) *Buckling of low arches as curved beams of small curvature*. U.S. National Advisory Committee for Aeronautics Technical Note no. 2840, November.

Gjeslvik A and Bodner SR (1962) The energy criterion and snap-buckling of arches. *Journal of the Engineering Mechanics Division-ASCE* 88(5): 87–134.

Hoff HJ and Bruce VC (1953) Dynamic analysis of the buckling of laterally loaded flat arches. *Journal of Mathematical Physics* 32: 276–288.

Johnson T, Frecker M and Gandhi F (2009) A bistable mechanisms for chord extension morphing rotors. In: *Proceedings of the 2009 SPIE conference on smart structures and materials*, San Diego, CA, 8–12 March.

Johnson T, Gandhi F and Frecker M (2010) Modeling and experimental validation of a bistable mechanism for chord extension morphing rotors. In: Proc. SPIE 7643, 76432B: 1–12.

Lock MH (1966) Snapping of a shallow sinusoidal arch under a step pressure load. *AIAA Journal* 4: 1249–1256.

Panesar AS and Weaver PM (2010) Optimization of blended bistable laminate for morphing flap. In: *AIAA structures, structural dynamics, and materials conference*, 12 - 15 April 2010, Orlando, Florida.

Pi YL and Trahair NS (1998) Nonlinear buckling and post-buckling of elastic arches. *Engineering Structures* 20(7): 571–579.

Schioler T and Pellegrino S (2004) Multi-configuration space frames. In: *AIAA/ASME/ASCE/AHS/ASC structures, structural dynamics, and materials conference*, 19 - 22 April 2004, Palm Springs, California.

Schultz MR (2008) A concept for airfoil-like active bistable twisting structures. *Journal of Intelligent Material Systems and Structures* 19: 157–169.

Schultz MR and Hyer MW (2004) A morphing concept based on unsymmetric composite laminates and MFC piezoceramic actuators. In: *Proceedings of the 45th AIAA/ASME/ASCE/AHS/ASC structures, structural dynamics & materials conference*, 19–22 April 2004, Palm Springs, California, *12th AIAA/ASME/AHS adaptive structures conference, 6th AIAA non-deterministic approaches forum, 5th AIAA Gossamer spacecraft forum*.

Schultz MR, Hyer MW, Williams RB, et al. (2006) Snap-through of unsymmetric laminates using piezocomposite actuators. *Composites Science and Technology* 66: 2442–2448.

Timoshenko SP (1936) *Theory of Elastic Stability*. McGraw-Hill, New York.

Walker AC (1969) A nonlinear finite element analysis of shallow circular arches. *International Journal of Solids and Structures* 5: 97–107.

Helicopter Rotor-Blade Chord Extension Morphing Using a Centrifugally Actuated Von Mises Truss

Patrick Moser*
Swiss Federal Institute of Technology, Zurich 8092, Switzerland
and
Silvestro Barbarino† and Farhan Gandhi‡
Rensselaer Polytechnic Institute, Troy, New York 12180

DOI: 10.2514/1.C032299

Previous studies have shown that chord extension morphing over a spanwise section of helicopter rotor blades can reduce main rotor power requirements in stall-dominant flight conditions while being able to increase the maximum gross weight, altitude, and flight speed capability of the aircraft. This study examines a centrifugally driven, fully passive chord morphing mechanism for helicopter rotor blades. It is based on a von Mises truss connected to a rigid extension plate that deploys through a slit in the trailing edge. When the rotor revolutions per minute increases beyond a critical value, the chordwise component of centrifugal force on the assembly results in the deployment of the plate beyond the slit in the trailing edge, effectively increasing chord length. On reducing the revolutions per minute, a retraction spring pulls the plate back within the confines of the blade. This study presents the design process, iterations, and final design solution for a configuration that undergoes 20% chord extension. A prototype was fabricated and tested on the bench top as well as on a rotor test stand at rotational speeds simulating more than 60% full-scale centrifugal loads. The test results demonstrate that the concept works. However, effects such as friction lead to revolutions-per-minute requirements different from those predicted by simulation.

Nomenclature

C	=	viscous damping coefficient
CF	=	centrifugal force
COR	=	center of rotation
c	=	chord
dt	=	time step
F	=	force applied at the von Mises truss vertex
K_{system}	=	spring at the base of the von Mises truss
K_{retract}	=	spring at the vertex of the von Mises truss
L	=	von Mises truss link length or Lagrange operator
m	=	mass concentrated at the von Mises truss vertex
Q	=	generalized force
q, $\dot{q}$	=	generalized coordinate and its derivative
T	=	kinetic energy
V	=	elastic potential energy
x, $\dot{x}$, $\ddot{x}$	=	von Mises truss vertex degree of freedom and its derivatives
θ_0	=	von Mises truss initial angle

I. Introduction

HELICOPTER rotor blades are susceptible to stall when operating at high speed, high altitude, or high gross weight. Recent studies [1–3] suggest that chord extension morphing is highly effective in alleviating stall and can expand the flight envelope boundaries (allowing the aircraft to fly higher, heavier, and faster) as well as reduce power requirement and vibration levels near the envelope boundaries.

Rotor-blade chord extension can itself be realized in a number of different ways. One approach is to elastically deform the blade structure in the chordwise direction as examined in [4]. Alternatively, a thin splitting plate can be extended through a slit in the blade's trailing edge over a certain spanwise section, as illustrated in Fig. 1. The deployment and retraction can be achieved by a motor that actuates a morphing truss. Although the first approach would, in principle, lead to an aerodynamically cleaner profile, the energy requirement associated with elastically deforming the structure, as well as the requirement for flexible or sliding skins that can extend in-plane while carrying pressure out-of-plane, make it more challenging. The second alternative, using an extendable trailing-edge plate (TEP), first suggested in [1] and further examined in [2,3,5], appears to be a lower-risk technology.

Khoshlahjeh et al. [2,3] considered a TEP deployed between 63 and 83% span on a UH-60A Blackhawk helicopter, resulting in a 20% chord increase relative to the baseline blade. The simulation results in [3] show reductions of up to nearly 17% in rotor power requirement for operation at high gross weight and altitude as well as increases of around 20 kt in aircraft maximum speed capability, 1500 lb in maximum gross weight capability, and 1800 ft in maximum altitude.

As an alternative to the morphing truss in Fig. 1, Johnson [6] proposed using the snap-through action of a bistable elastic arch to move the TEP in the chordwise direction, from a retracted position within the confines of the blade to a deployed position extending beyond the baseline trailing edge. However, the very high strains in the bistable arches during snap-through presented a great challenge, both significantly limiting the materials that can be used and increasing the likelihood of structural failure. Also, Johnson's study had difficulty identifying an actuation mechanism (with required stroke and force capability) suitable for the bistable arch.

Recognizing the challenges associated with the use of motors for actuation in the large centrifugal fields that the helicopter blades experience, Prabhakar et al. [7] proposed exploiting the change in centrifugal force associated with revolutions-per-minute change for rotor span morphing. In their work, they demonstrated, on the hover stand, a telescoping rotor with a fixed inner portion and a sliding spring-restrained outer portion increasing its span by over 25% with revolutions-per-minute increase.

Received 5 February 2013; revision received 10 February 2014; accepted for publication 14 February 2014; published online 18 June 2014.

*Student, Mechanical Engineering Department, Main Building, Ramistrasse 101.

†Research Associate, Mechanical, Aerospace, and Nuclear Engineering Department, 110 8th Street. Member AIAA.

‡Rosalind and John J. Redfern Jr. '33 Endowed Chair in Aerospace Engineering, Mechanical, Aerospace, and Nuclear Engineering Department, 110 8th Street. Associate Fellow AIAA.

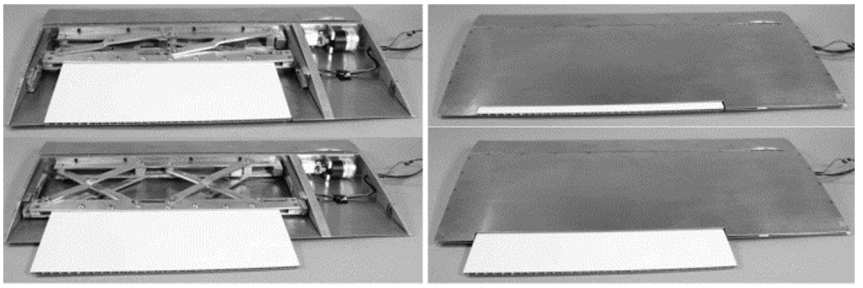

a) Bench-top prototype

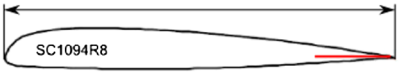

b) Baseline chord

c) Baseline chord + TEP extension

Fig. 1 Chord extension morphing with extendable TEP [1].

Based on an assessment of the prior work in rotor morphing discussed previously, the present study focuses on achieving chord extension morphing through the deployment/retraction of a trailing-edge plate (TEP) enabled by a von Mises truss in conjunction with a change in rotor revolutions per minute. The von Mises truss replaces the bistable elastic arch in [6] as a device that deploys/retracts the TEP, while the change in centrifugal force associated with change in revolutions per minute is used as the enabler. Because no actuators are used, the system is completely passive and eliminates the need to transfer actuation power into the rotating system. The paper presents analytical modeling and conceptual design of the system, followed by fabrication, and culminating in bench-top test and validation and preliminary rotor testing on the hover stand.

II. Concept and Analysis

The von Mises truss is a mechanical system first introduced by von Mises in 1923 [8] to model the stability of a shallow arch. As shown in Fig. 2, it consists of two pinned–pinned rigid members whose independent ends can slide laterally against the springs denoted as k_{system}. In the absence of the retraction spring k_{retract}, when the force F at the vertex exceeds a critical value, the truss "snaps through" and assumes the configuration shown in the dashed lines. This is another stable equilibrium position of the truss, and so if the force is removed, it remains in this configuration without any requirement for locking. The absence of any locking requirement along with the large possible "stroke" makes a von Mises truss attractive for morphing applications.

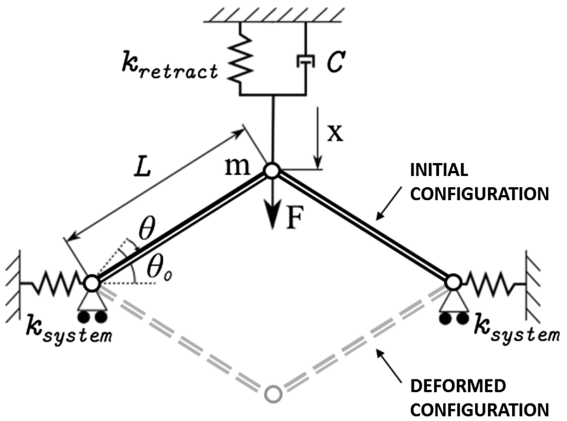

Fig. 2 Schematic representation of a von Mises truss, with additional retraction spring and damper.

Figure 3 represents the force versus vertex displacement behavior of a "bistable" von Mises truss under the conditions of displacement control (solid line) and force control (dashed line). Note that, in the current study, the origin of the force F is the chordwise component of the centrifugal force. If the revolutions per minute, and correspondingly the chordwise component of centrifugal (CF) force, were to exceed a critical value, then the von Mises truss would snap through along the horizontal dashed line in Fig. 3. Return to the original configuration, however, requires a negative force. Although a reduction in revolutions per minute would reduce the chordwise CF force, it would not make it negative, which makes retraction problematic. The retraction spring k_{retract} is introduced to pull the von Mises truss back to the original configuration when the revolutions per minute (and correspondingly the chordwise component of CF force) reduce.

Figure 4 shows the modified force versus vertex displacement behavior of the von Mises truss with a retraction spring (shown in Fig. 2). As in Fig. 3, the solid and the dashed lines represent behavior under displacement and force control, respectively. In Fig. 4, although the system snaps through, it no longer exhibits bistable behavior (unlike Fig. 3, the curves do not cross zero force at nonzero displacement). Thus, if the force F was reduced or removed after the system snapped through, it would simply snap back and return to the original equilibrium position. This is very attractive in the present application because an increment in revolutions per minute and chordwise component of CF force can snap the von Mises truss and deploy the TEP, and a reduction in revolutions per minute can conversely snap back the truss and retract the TEP.

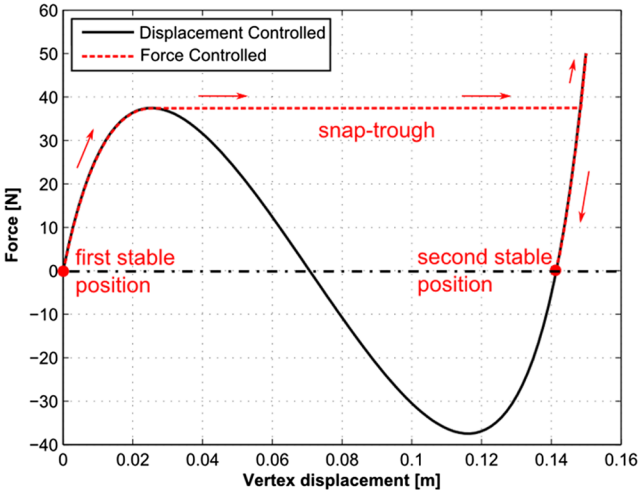

Fig. 3 Bistable behavior of a von Mises truss.

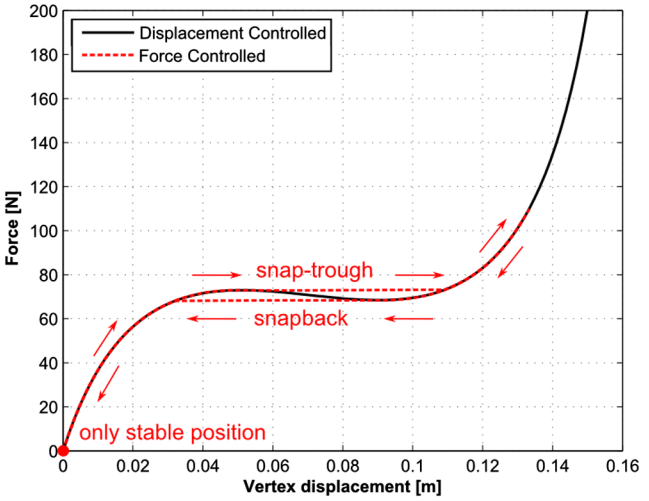

Fig. 4 Snap-through behavior of a von Mises truss.

The governing equation of motion for the von Mises truss with retracting spring and dashpot, depicted in Fig. 2, are obtained by deriving expressions of the kinetic energy T and elastic potential energy V of the system and introducing them in Lagrange's equation:

$$Q = \frac{\mathrm{d}}{\mathrm{d}t}\left(\frac{\partial L}{\partial \dot{q}}\right) - \frac{\partial L}{\partial q} \quad \text{with} \quad L = T - V \tag{1}$$

The generalized coordinate q corresponds to the vertex truss degree of freedom, x, and the generalized force Q corresponds to the force F at the vertex. After substitutions and simplifications, the equation of motion can be obtained, as given next:

$$F = m\ddot{x} + C\dot{x} + k_{\text{retract}}x + \frac{2k_{\text{system}}(-x + L\sin[\theta_0])(-\cos[\theta_0] + \sqrt{1-(-[x/L]+\sin[\theta_0])^2})}{\sqrt{1-(-[x/L]+\sin[\theta_0])^2}} \tag{2}$$

In addition to k_{system}, k_{retract}, and F, which have been previously defined, L and θ_0 are the geometric parameters describing the von Mises truss (see Fig. 2), m represents the effective mass (lumped at the vertex), and C represents any damping in the system. x and its derivatives represent the vertex vertical displacement, velocity, and acceleration, respectively, of the truss vertex. If the time derivatives are ignored, then the equation describes the static behavior of the von Mises truss with a retracting spring.

To verify the accuracy of the analytical model, the static behavior of the von Mises truss was validated against nonlinear finite-element simulation results using ANSYS 13.0, and the two sets of predictions were found to be in excellent agreement for several combinations of the truss parameters (see Fig. 5).

The curves shown in Figs. 3 and 4 are from a static analysis. For a controlled displacement input, the truss is seen to exhibit negative stiffness behavior over a portion of the total stroke but does not experience snap-through. Static and dynamic simulations at low to moderate rates and damping will appear fairly similar. However, for a controlled force input, a static analysis does not yield the points on the horizontal portion of the curve representative of snap-through. As the force increases beyond the critical value, the displacement becomes very large (system jumps branches), and the horizontal portion of the curve is filled in by deduction. A dynamic simulation, on the other hand, would not only capture the snap-through portion of the curve but would also result in transient oscillations at the end of the event. The transient oscillations can be dissipated through the presence of damping [9]. It should be noted, as explained in [10], that a von Mises truss would display snap-through but no negative stiffness under force control (while the reverse is true under displacement control).

Figures 3 and 4, showing results for specific values of geometric parameters ($L = 0.1$ m, $\theta_0 = 45$ deg) and spring stiffnesses ($k_{\text{system}} = 2000$ N/m, $k_{\text{retract}} = 0$ and 1000 N/m), were primarily meant to highlight the difference between force and displacement control as well as the difference between a von Mises truss without a retracting spring that displays bistability and one with a retracting spring that displays snap-through but not bistability. Variation in spring stiffness parameters would result in changes in behavior as shown in Figs. 6 and 7. From Fig. 6, for $k_{\text{retract}} = 0$, it can be observed that increasing k_{system} leads to increase in stiffness of the von Mises truss at the equilibrium positions and higher critical snap-through force, but the behavior always remains symmetric about zero force. Figure 7 shows the effect of increasing the retraction spring stiffness for a constant $k_{\text{system}} = 2000$ N/m. The main effect is on the symmetry of the curves about zero force. It is observed that, for low values of k_{retract}, the system is still bistable, but the critical force to retract is lower than the force to deploy. As k_{retract} increases further, the curves move above the force axis, and the system will exhibit snap-through but not bistability. The combination of values k_{system} and k_{retract} determine the force levels at which snap-through and snapback occur and are important design parameters in the present study. Finally, if k_{retract} increased even further, the system would no longer display snap-through, displaying instead a nonlinear force versus displacement behavior.

III. System Design

Because the final goal was to experimentally demonstrate centrifugally induced chord extension and retraction in a rotor test,

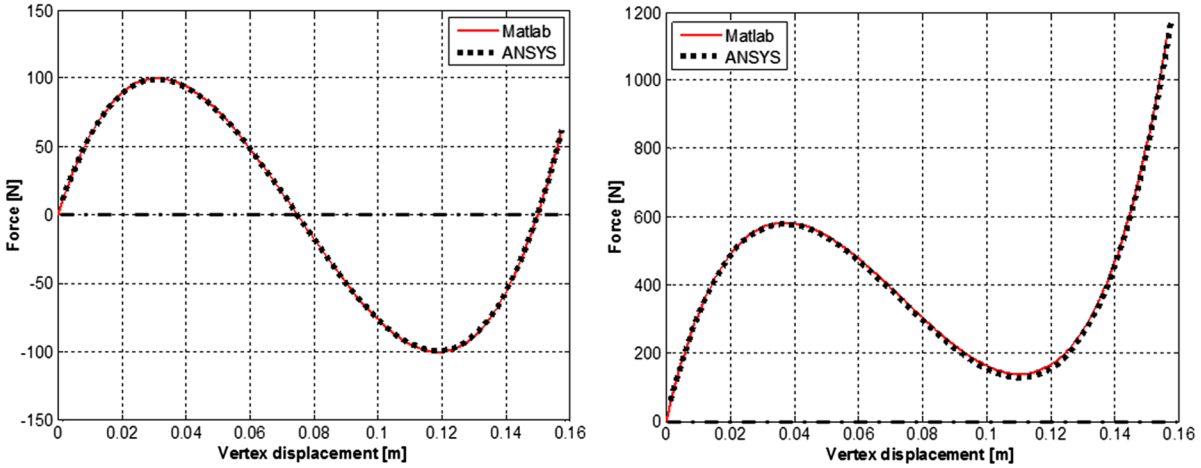

a) Bi-stable behavior **b) Snap-through behavior**

Fig. 5 Matlab vs ANSYS simulation of a von Mises truss for two diverse sets of parameters: a) bistable, and b) snap-through behavior.

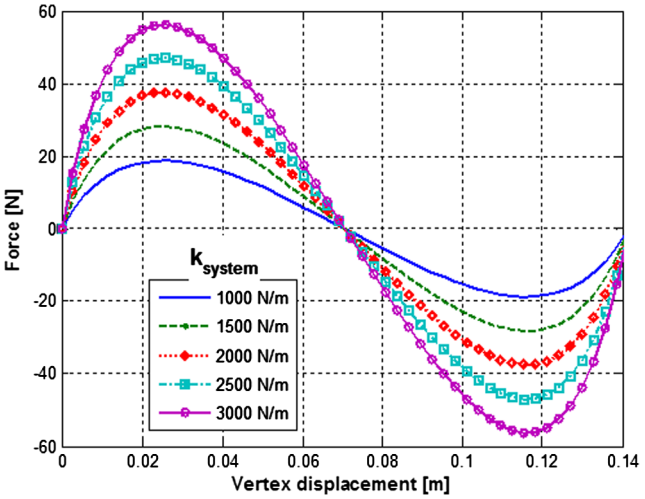

Fig. 6 Effect of system spring stiffness on force/displacement behavior of von Mises truss ($k_{\text{retract}} = 0$).

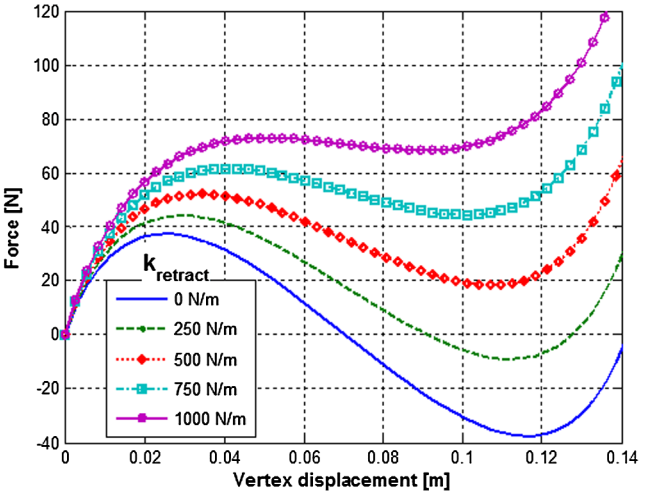

Fig. 7 Effect of retraction spring stiffness on force/displacement behavior of von Mises truss ($k_{\text{system}} = 2000$ N/m).

the geometric and operational limits of the chosen Pennsylvania State University rotor test facility (also known as the Adverse Environment Rotor Test Stand, or AERTS) were taken into consideration from the onset. Active rotor tests at the Penn State rotor test facility are frequently conducted using the boom and paddle setup schematically represented in Fig. 8. The overall diameter is 2.73 m, as indicated in the figure. The paddle can accommodate various types of active or morphing rotor sections and test these prototypes in the presence of realistic, near-full-scale centrifugal accelerations.

The paddle frame, illustrated in Fig. 9, has a 30.5 cm span, 40.6 cm chord, and with a NACA 0015 airfoil, has a maximum thickness of 6.1 cm. The space from the leading edge to 25% chord is for the main rotor spar, and the region aft is available for the chord morphing section. Because the objective was to increase effective chord by 20%, the trailing-edge plate (TEP) has to have a chord length greater

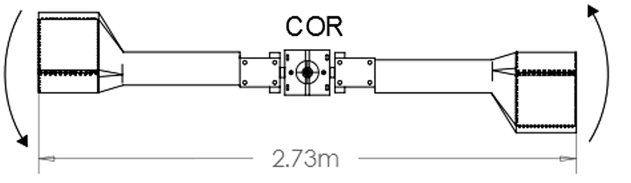

Fig. 8 Schematic top view of the boom and paddle setup used in the Penn State hover test facility.

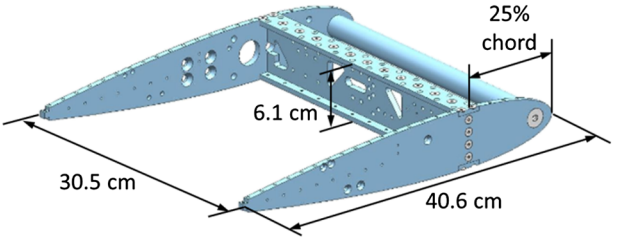

Fig. 9 Paddle frame (test section) for chord morphing mechanism.

than 20%. A plate with 40% chord length was used, and because it should be fully contained in the airfoil in the retracted state, this limited the space available to the morphing von Mises truss (see Fig. 10). Leaving a little room for fixtures and a bumper at the rear of the spar, the von Mises truss, whose vertex connects to the TEP, could occupy the space between 32.75 and 60.25% chord, placing the spanwise axis of symmetry at 46.5% chord. The overall stroke of the von Mises truss is 27.5% chord. However, some space is allocated at the trailing edge (7.5% chord) to accommodate the initial motion of the TEP before reaching the snap-through condition. Therefore, only 20% chord is effectively available past the trailing edge. At the 46.5% chord line, space is allocated in the spanwise direction to the system springs, based on availability and consideration of their length and stroke. This sets the von Mises truss link lengths L and the angle θ_0. The retraction spring is situated in the spar.

The system and retraction springs, in addition to fitting within the available space constraints, must provide the required stiffness for deployment and retraction of the extension plate at desired rotor revolutions-per-minute values. In [2,3], the benefits of chord extension morphing were examined based on a UH-60A Blackhawk helicopter. The rotor radius of the Blackhawk is 8.18 m, and its nominal rotor speed is 27 rad/s [11]. To replicate the spanwise centrifugal accelerations on a morphing system situated between 63 and 83% span on the UH-60A would require the Penn State rotor stand to operate at a speed of around 568 rpm. However, test-section

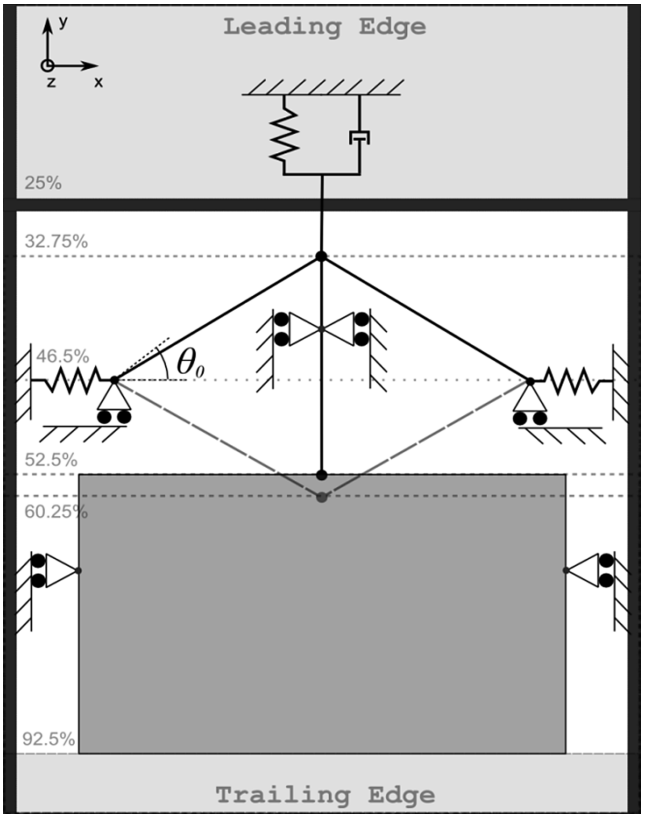

Fig. 10 Schematic showing the layout and geometric constraints in the design of the chord morphing mechanism within the test paddle.

mass and safety considerations dictated that it was not possible to exceed an operational speed of 500 rpm. Accounting for the mass of the morphing system, the system and retraction spring stiffnesses were selected with the following design goals in mind: nominal revolutions per minute: 451.13 (100.0%); deployment revolutions per minute: 484.97 (107.5%); maximum revolutions per minute: 496.25 (110.0%); and retraction revolutions per minute: 462.41 (102.5%).

In [2,3], the effect of a trailing-edge plate, extending from 63 to 83% span on the UH-60A was considered. The CF acceleration at the midspan location of the prototype (radial location of 1.2125 m from center of rotation) and at the nominal design revolutions per minute (451.13 rpm) was determined to be 62.15% of the CF acceleration on the UH-60A at 73% span (midspan of the chord-extension section). A successful test would thus demonstrate operation of the mechanism at roughly 62% full-scale CF loads. This is important because survivability and operability of mechanisms in high-g environments is always a challenge.

As stated earlier, the actuation force comes from the chordwise component of the centrifugal (CF) force on the section. At a given rotational speed, any mass m within the rotor blade at a distance r from the center of rotation (COR) experiences a CF force normal to the velocity vector, as depicted in Fig. 11. Although mass on the 25% chord line would experience only a spanwise CF force, any chordwise offset results in both spanwise and chordwise components of the CF force, as given next:

$$\mathrm{CF} = mr\omega^2 = mr\left(\mathrm{RPM} \times \frac{2\pi}{60}\right)^2 \tag{3}$$

$$\mathrm{CF}_{\mathrm{span}} = \mathrm{CF}\cos\left(\arctan\left(\frac{-y_{\mathrm{c.g.}}}{x_{\mathrm{c.g.}}}\right)\right) \tag{4}$$

$$\mathrm{CF}_{\mathrm{chord}} = \mathrm{CF}\sin\left(\arctan\left(\frac{-y_{\mathrm{c.g.}}}{x_{\mathrm{c.g.}}}\right)\right) \tag{5}$$

One of the complicating factors associated with CF-force-based actuation is that, as the von Mises truss and plate deploy, the CF force on the assembly increases due to the increased aft chordwise offset of the assembly. In other words, the CF force on the system is greater in the deployed position than in the retracted position. This, in turn, requires a stronger retraction spring to pull the system back at reduced revolutions per minute. And the increased stiffness of the retraction spring changes the system behavior from one that exhibits snap-through (as shown in Fig. 4) to one that no longer does so (see Fig. 12). Even so, the von Mises truss can undergo the desired very large stroke and deploy/retract the extension plate (TEP).

Another factor is that an iterative procedure has to be used to calculate the deflection. The solid curve in Fig. 12 corresponds to an independently applied force, whereas the dashed curve corresponds to the deformation of the von Mises truss vertex (and correspondingly the deployment position of the TEP) with increase in revolutions per minute. The issue with the dashed curve is that the CF force itself

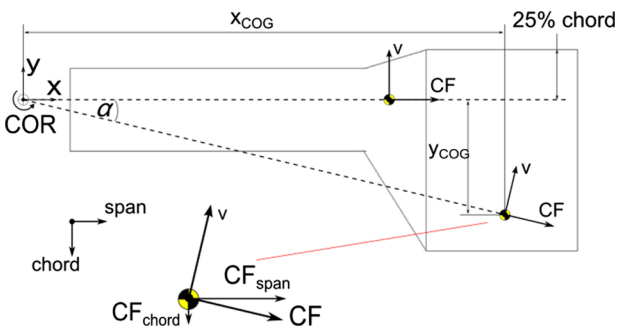

Fig. 11 CF force and its spanwise and chordwise components.

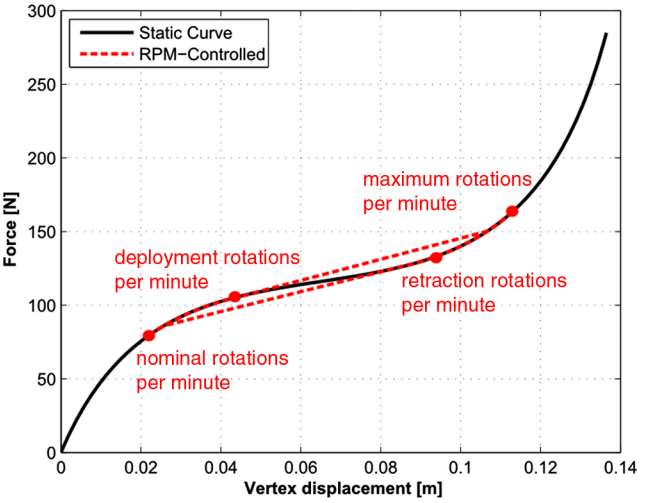

Fig. 12 Static curve for a von Mises truss with a stiff retracting spring in parallel.

depends on the deformed position, hence the need for an iterative solution scheme and the identification of spring stiffnesses and mass tuning through iteration.

The analytical model used in the simulations and design had a few simplifications. To calculate the centrifugal force that actuates the system, the mass of each of the components (such as the von Mises truss links, the extension plate, etc.) was assumed to be concentrated at its c.g. In reality, the centrifugal acceleration varies with position, for example from the inboard end to the outboard end of the extension plate. To verify the validity of this approximation, a finite-element model was created and spun in ANSYS 13.0. Likewise to the static analysis (Fig. 5), the two approaches produced similar predictions with negligible discrepancies. In addition, all springs are assumed to behave linearly and in accordance with manufacturer-provided specifications, and friction effects have been neglected.

The quasi-static response of the proposed chord morphing mechanism, obtained by neglecting the velocity and acceleration terms in Eq. (2), over full revolutions-per-minute operation cycle is shown in Fig. 13. Deployment is predicted at 481 rpm, and the system is observed to retract at 463 rpm.

The quasi-static response not only is affected by the system and retraction spring stiffnesses but also depends on the mass of the components of the assembly. An increase in plate mass shifts the response toward lower revolutions per minute, and vice versa, as illustrated in Fig. 14. The masses of the links of the von Mises truss also affect the response. Increasing mass on the outboard link at the "base" of the von Mises truss reduces the required revolutions-per-

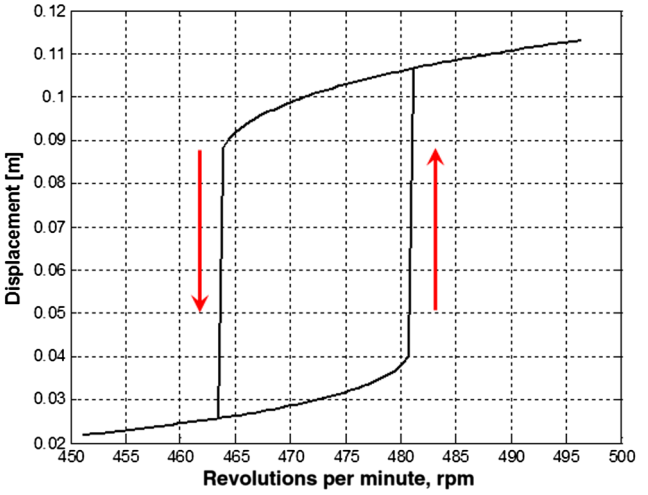

Fig. 13 Static response of the morphing mechanism under a full cycle in revolutions-per-minute variation.

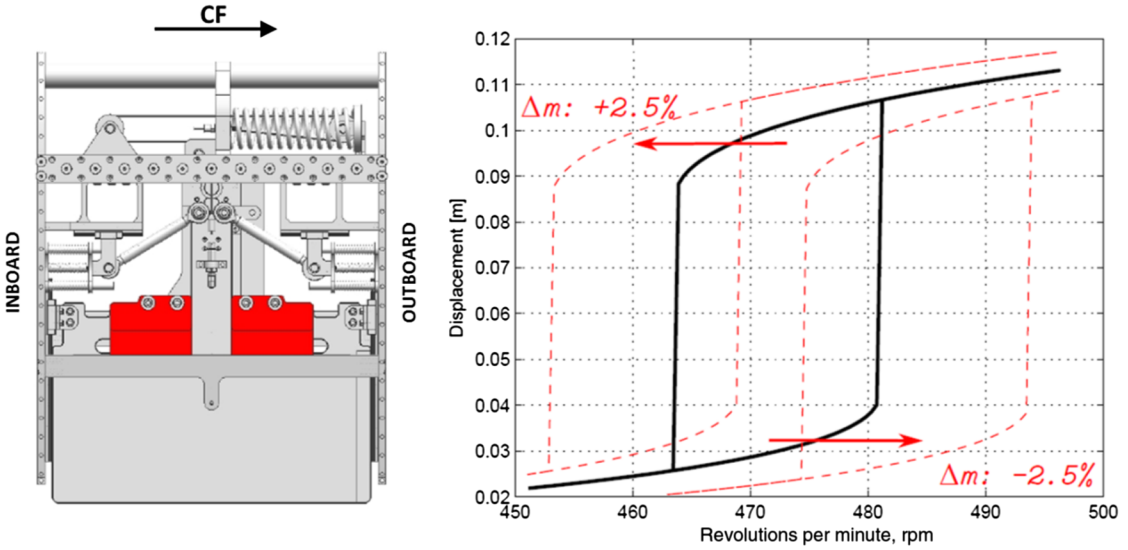

Fig. 14 Effect of plate mass variation on the static response of the morphing mechanism.

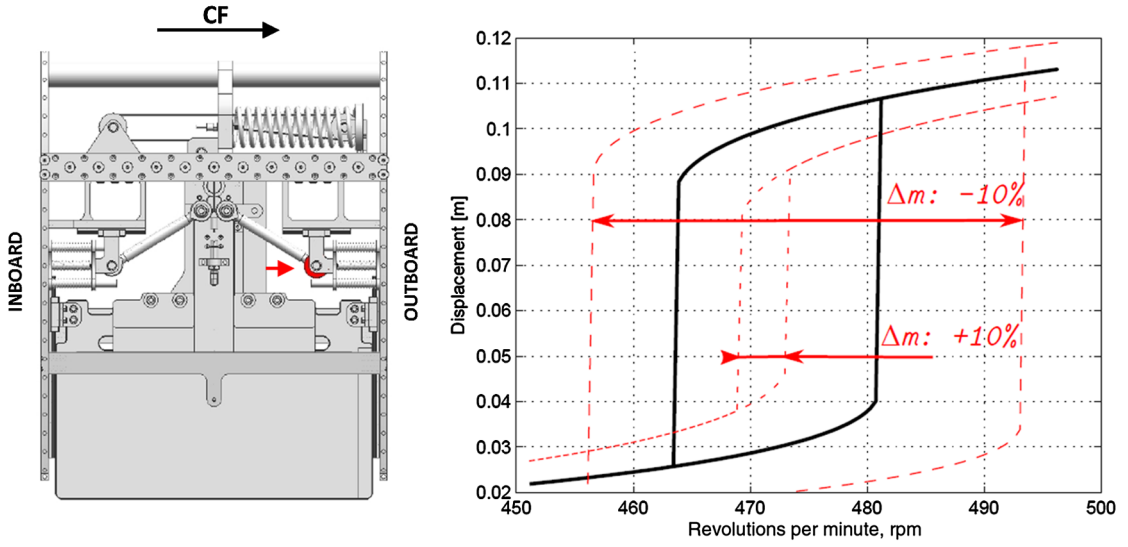

Fig. 15 Effect of von Mises truss link mass variation on the static response of the morphing mechanism.

minute variation for complete two-way actuation, and vice versa (see Fig. 15). The opposite is true on the inboard link; reducing the mass at the base of the von Mises truss also reduces the required revolutions-per-minute variation for two-way actuation.

The dynamic response, with the inclusion of the velocity and acceleration terms, is shown in Fig. 16. At the ends of the deployment and retraction portions of the cycle, transient oscillation in response is observed. If the damping coefficient were increased ($C = 1\ \mathrm{N \cdot s/m}$ used in Fig. 16), the transients would settle much quicker [9]. It should be noted that the salient features of the response (deployment and retraction revolutions per minute, the stroke, etc.) are well captured even with the quasi-static analysis.

IV. Prototype Design and Fabrication

The design of the prototype involved an iterative process. Based on geometric considerations (Figs. 9 and 10), desired deployment and retraction rotational speeds specified in the previous section, and estimated component masses, system and retraction spring stiffnesses were selected. Using these stiffnesses, the deployment and retraction behaviors were simulated, and then the component masses and spring stiffnesses were again readjusted until the predicted deployment and retraction behavior closely matched the target behavior. During this process, only commercial off-the-shelf springs were considered. Linear miniature slide bearings were used at the ends of the extension plate, the ends of the von Mises truss, and along the rail under the connection element linking the von Mises truss vertex to the extension plate, to guide the motion of the system. A

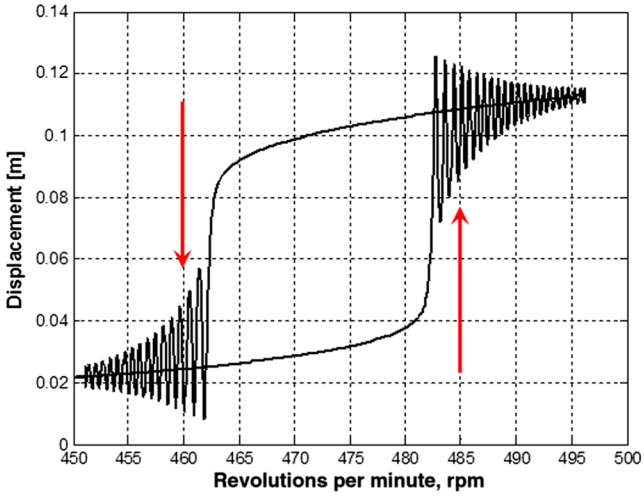

Fig. 16 Dynamic response of the morphing mechanism under a full cycle in revolutions-per-minute variation.

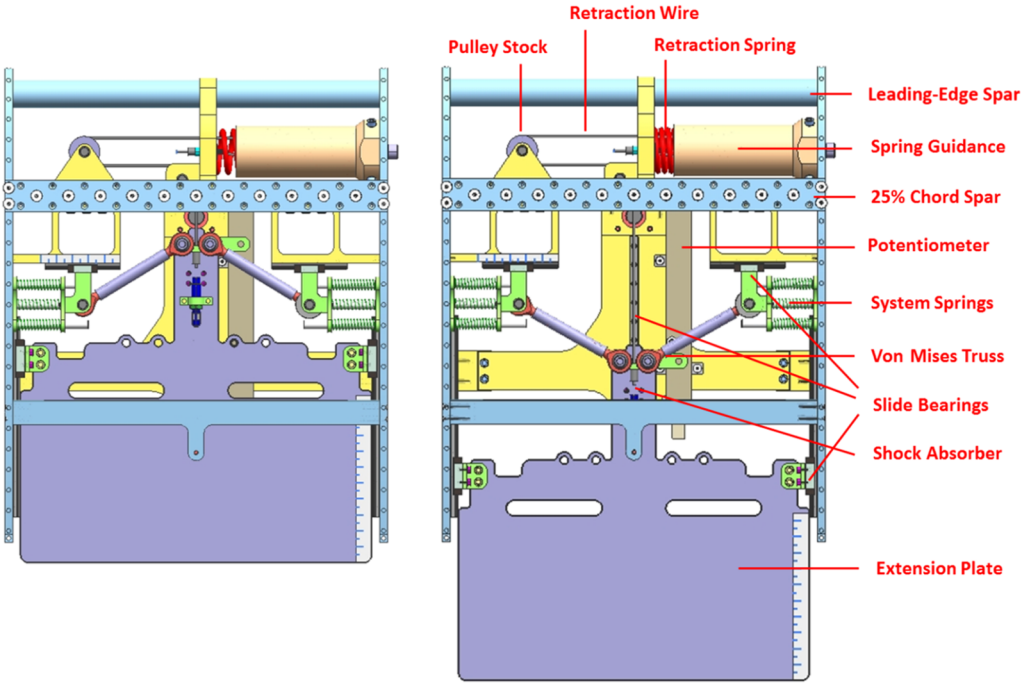

Fig. 17 CAD drawing of prototype with various components shown (top view, skin removed).

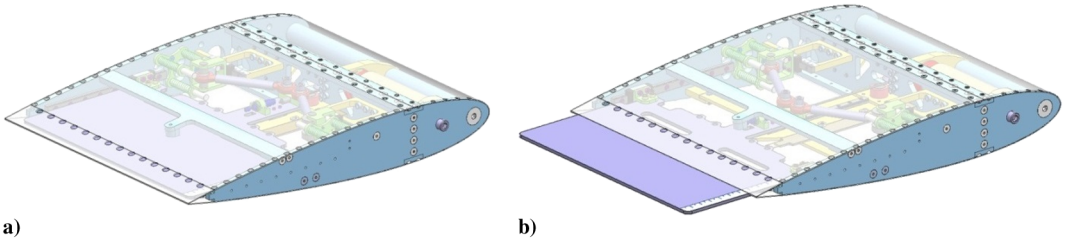

Fig. 18 CAD drawing of prototype in a) retracted, and b) deployed state (isometric view, translucent skin).

CAD drawing of the prototype is shown in Figs. 17 and 18, and a summary of the main features of the prototype are reported in Table 1. A picture of the fabricated prototype is shown in Fig. 19.

Additional components introduced to ensure smooth functioning included internal guides for the springs to prevent buckling and shock absorbers at both ends to absorb and dissipate energy on completion of TEP deployment and retraction. To measure the deformation, rulers as well as a linear potentiometer from SpectraSymbol (SoftPot 150 mm) connected to a V-Link wireless voltage node from MicroStrain were used.

The predicted c.g. of the entire test section, based on the CAD model, was in good agreement with experimental measurement. The two-dimensional c.g. was determined by measuring the weight of the test section at three distinct points independently and using a weighted average to find the center. Its position is at 39.6% chord (0.161 m from the leading edge) when the extension plate is retracted and at 43.8% (0.178 m from the leading edge) when deployed. When the von Mises truss and the extension plate transition from the retracted to the deployed positions, the aft chordwise motion of the c.g. is about 17 mm. The dummy mass used in the second paddle to balance the rotor was built to match the c.g. of the test section in the retracted state.

A safety factor of 2 was used for dimensioning all the structural components of the prototype due to design loads. All components were analyzed after creating a finite-element model in ANSYS 13.0 of the main structural load-carrying elements. Two-dimensional shell elements were used to model the structural components, and body forces were applied to the structure by means of the OMEGA command, which simulates the rotational environment and accelerations.

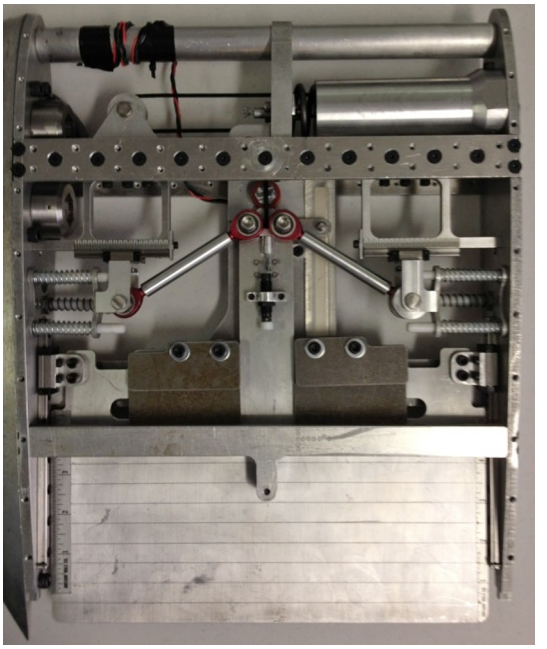

Fig. 19 Fabricated experimental prototype in its retracted configuration (skin removed).

Table 1 Summary of the main features of the experimental prototype

Parameter	Value
System truss link length L	92.7 mm
Initial truss angle θ_0	44.5 deg
System spring k_{system}	2399.24 N/m
Retraction spring $k_{retract}$	7145.17 N/m
System stroke	111.7 mm
Chord extension	20% c
Test section mass	3.09 kg
Mechanism mass	1.65 kg
Extension plate mass	0.40 kg

Loads from the von Mises truss mechanism were applied locally on the rails of the bearings where the loads are actually transferred into the surrounding structure. The stress distribution for the main structural elements is shown in Fig. 20. All components satisfied the safety factor. Local peak stresses are due to the nodal application of distributed forces and are not critical. Additionally, the safety of all load-carrying bolts has been verified to guarantee a safe operation, and the bearings have been chosen to withstand twice the present loads at 500 rpm.

Finally, some considerations can be made regarding the weight penalty associated with the chord morphing device. The fabricated prototype is only one possible implementation of the proposed design, limited by the volume within the rotor test section and the fabrication capabilities and materials readily available. Most of its components have been designed with quite large safety factors, thus introducing some weight penalties.

A full-scale system could use the larger blade volume (in particular, span) to reposition some of the components (e.g., the retraction spring) and reduce the complexity of the final design (e.g., elimination of the pulley). An operational system would also make use of more advanced fabrication techniques and materials (e.g., composites) to limit the total weight. Changes in the mass of the different parts should then be accounted for when considering the available centrifugal chordwise accelerations of the full-scale system and tailoring the system to deploy/retract to the desired revolutions per minute. The design procedure discussed in this paper demonstrates that the designer has several degrees of freedom to act on the behavior of the system.

Therefore, the weight impact of the proposed structural configuration on a full-scale operational system is difficult to estimate. Considering only the main components of the proposed system, the weight penalty that the chord morphing device introduces on a full-scale blade can be roughly estimated in 1–2% of the total weight, with the heaviest element of the prototype being the rigid plate. In an operational environment, this could be replaced with a much lighter composite plate.

V. Experimental Testing and Results

Bench-top and rotor-stand tests were carried out to verify the performance of the proposed morphing mechanism.

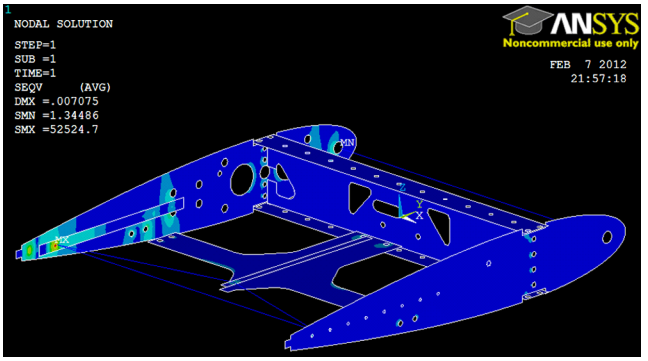

Fig. 20 ANSYS finite-element stress analysis on the main structural components.

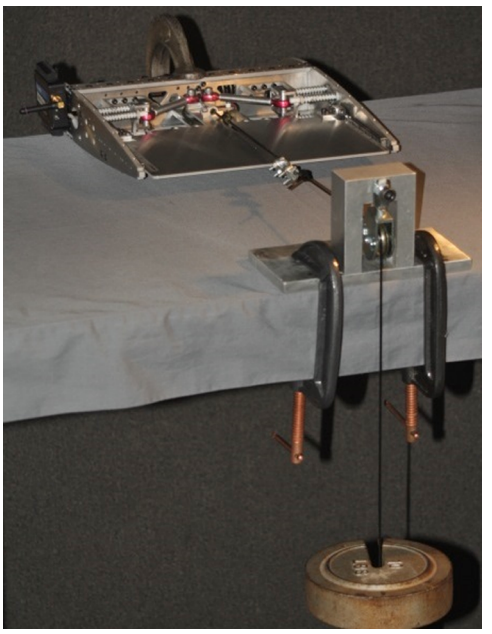

Fig. 21 Bench-top test setup.

Figure 21 shows the prototype clamped to a bench with weights applied in conjunction with a pulley to introduce a force at the vertex of the von Mises truss. This simulates the actuation force F, which induces the system to snap. Force was increased in 0.9 kg (8.9 N) steps up to 22.2 kg (218 N), and the displacement was measured at each step by the potentiometer. A similar procedure was followed upon unloading. The test was repeated three times, and the experimental data along with analytical prediction results are shown in Fig. 22.

The measurements show good repeatability, but two observations can be made. First, the test data exhibits hysteresis around the analytical predictions, and this could be attributed to frictional effects. Second, the analytical prediction curve is not placed quite in the center of this hysteresis loop. This suggests that the effective stiffness of the retraction spring may be a little higher than assumed.

Next, the mechanism was tested on the Penn State rotor test facility to demonstrate the chord extension and retraction induced by revolutions per minute and CF force change. The prototype was mounted at the end of one of the booms by bolting the rib to the boom at three points. A second paddle with a dummy mass was attached to the other boom for mass balancing purposes. Figure 23 shows the setup ready to test on the Penn State rotor test facility. The deployment of the mechanism and the resulting chord extension shifts the c.g. aft and

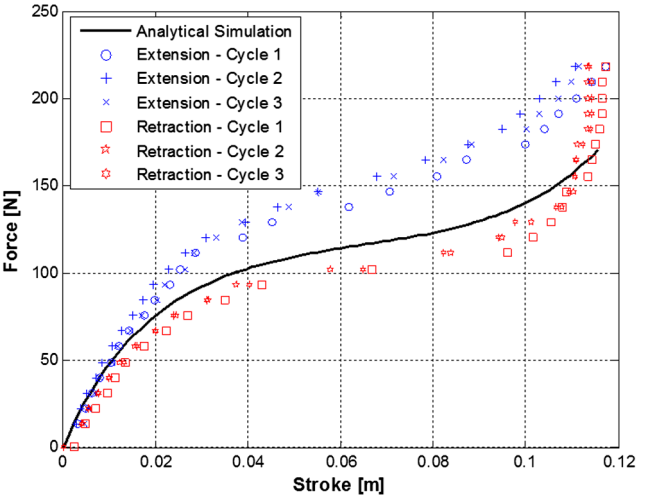

Fig. 22 Bench-top test results.

Fig. 23 Setup on the Penn State rotor test facility.

could have been expected to induce large vibratory loads due to rotor imbalance. However, this was found not to be the case, and no excessive vibratory loads were measured in several tests.

Starting from zero, the rotor speed was increased in steps up to a value above the predicted deployment revolutions per minute. In the first set of tests, the system did not deploy within the desired revolutions-per-minute range. The weight of the extension plate was then increased by attaching a 325 g mass to achieve deployment within the operating revolutions-per-minute range. Figure 24 shows the experimental as well as the analytical prediction results. With the increased extension plate mass, the predicted deployment revolutions per minute dropped to 346 rpm, while the test results show the plate deploying at 434 rpm. A comparable discrepancy was observed in the rotational speeds corresponding to plate retraction (the analytical prediction was 323 rpm, whereas the plate actually retracted at 230 rpm in the rotor test).

These discrepancies may be attributed to a couple of possible factors. First, the friction effects, especially at the pin joints at the ends of the links of the von Mises truss. Additionally, imperfections in alignment and symmetry could make it more difficult for the chordwise component of the CF force to deploy the extension plate and the retraction spring to move it back. For example, the differences in the spanwise components of the CF force on the two links of the von Mises truss could lead to asymmetric loads on the system that resist the truss's motion. Although these discrepancies should drive new efforts to overcome them, the results of the rotor test demonstrate that the idea of using a von Mises truss connected to an extension plate and having a change in rotor revolutions per minute deploy and retract the plate has been experimentally shown to be achievable.

Figure 25 shows photographs from the rotor test with the extension plate in retracted configuration at low revolutions per minute and in the deployed configuration at 434 rpm. These images were taken

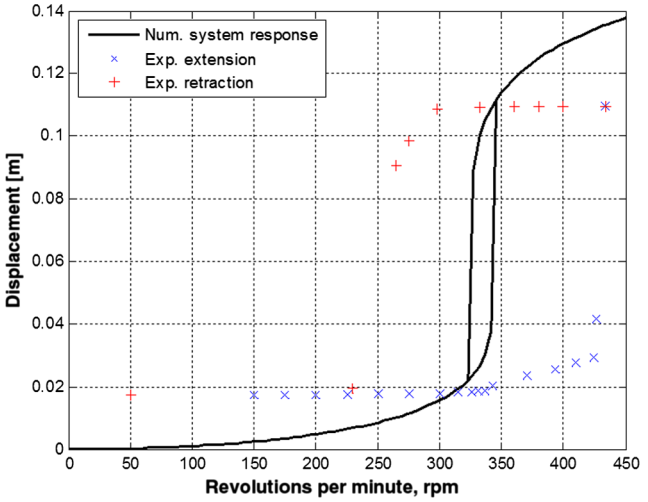

Fig. 24 Rotor test results.

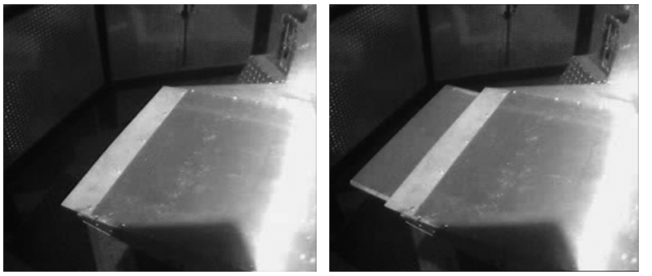

a) **b)**

Fig. 25 Images of trailing-edge plate during the rotor test taken with synchronized stroboscopic lamps a) retracted at low revolutions per minute, and b) deployed at high revolutions per minute.

using stroboscopic lamps in the rotor test facility. The deployment of the plate results in a 20% increase in effective chord, as expected.

VI. Friction Effects and Model Refinements

Experimental data from the bench-top test (Fig. 22) show presence of hysteresis not being modeled. This suggests that some sort of friction in the prototype opposes motion, increasing linearly with the vertex displacement. It should be noted that this hysteresis proved to be repeatable and roughly symmetric with respect to the estimated static behavior (Fig. 22). Possible sources of this type of friction could be the pulley–cable system connected to the retracting spring or small misalignments in the three rails that support the rigid plate and make its motion more and more difficult as the plate deploys. Limitations in the fabrication process and precision of the technology demonstrator and design choices made to keep costs low are deemed to be contributing factors. The authors envision that friction could be reduced significantly with design improvements and manufacturing precision on a full-scale production blade.

Nonetheless, the model was updated to account for this effect. An empirically fit friction factor F_{friction} was added to the basic static behavior (positive or negative depending on the direction of motion) of the von Mises truss as a function of the displacement x of its vertex, as reported in Eq. (6):

$$F_{\text{friction}} = \frac{x \cdot F_{\text{friction}}^{\max}}{x_{\max}} \tag{6}$$

where $x_{\max}$ is the maximum displacement of the vertex, and $F_{\text{friction}}^{\max} = 40$ N is the maximum value of correction added to the system for $x = x_{\max}$.

Additionally, the static curve predicted by the model does not lie perfectly in the middle of the hysteresis loop. The retracting spring k_{retract} was identified as the main contributor for this discrepancy. Experimental testing of the adopted spring alone in an Instron machine measured a stiffness constant of 7680.55 N/m, versus the nominal value of 7145.17 N/m considered in Table 1. Therefore, this was accounted for in the improved model.

Figure 26 shows a much improved correlation between the bench-top test data and the updated model, which takes into account the real spring constant for the k_{retract} and a suitably estimated amount of friction linearly increasing with the von Mises truss vertex displacement.

The dynamic analysis of the proposed morphing mechanism was updated similarly. The same correction for k_{retract} and the amount of friction was used. The dynamic model was also refined to consider the presence of mechanical stops in the prototype due to the presence of shock absorbers at both ends. These reduce the overall stroke (and, therefore, the initial angle θ_0) and introduce a preload in the system springs k_{system} of the von Mises truss mechanism. The introduction of these corrections within the model produces a much better correlation with the experimental data (Fig. 27), illustrating the necessity of a much wider range of revolutions-per-minute variation for full two-way actuation, as measured in the experiments. However, the reader is reminded that displacement versus revolutions-per-minute behavior can be tailored by minimizing friction and adjusting the

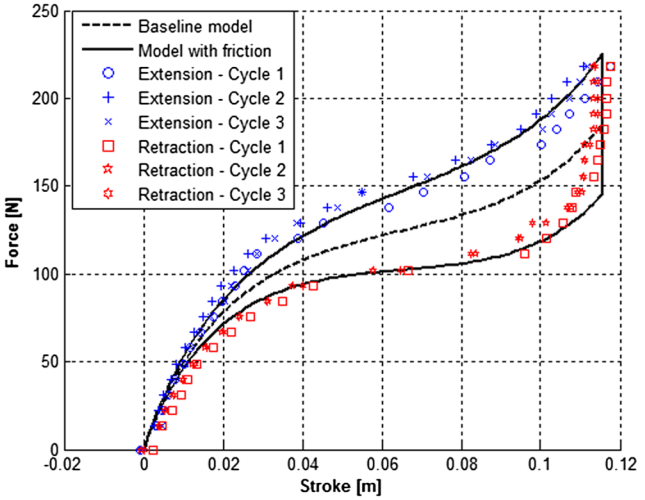

Fig. 26 Improved model correlation with the bench-top test results.

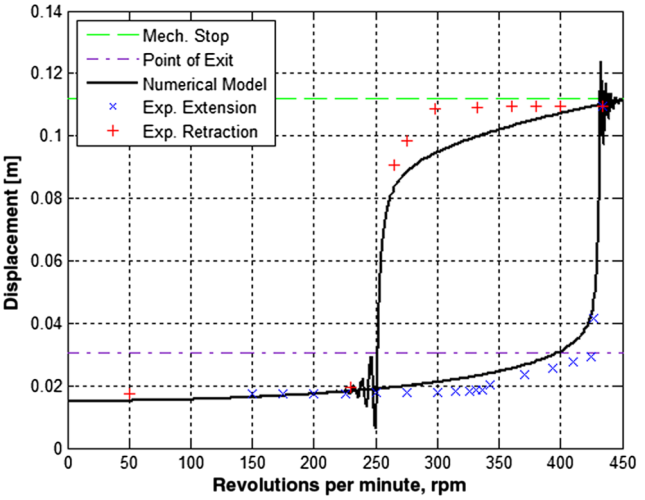

Fig. 27 Improved model correlation with the rotor test results.

plate and especially the link mass. The necessity to fine-tune each available feature of the proposed design and account early at the modeling stage for additional effects, such as friction, is of great importance when scaling up to the UH-60. In this case, a combination of larger spanwise CF load (that could produce higher friction loads) and lower chordwise loads (to actuate the von Mises truss) could impact negatively on the working of the entire device if not properly accounted for.

VII. Conclusions

Helicopter rotor-blade chord morphing can alleviate stall and improve the rotor craft performance when flying close to the flight envelope boundaries. In this paper, the authors have presented a novel approach to realize a passive, revolutions-per-minute-controlled chord morphing mechanism. Emphasis has been put on the actuation concept, the analytical model of the system, based on a von Mises truss, the design and fabrication of a prototype, and the experimental verification of the system behavior in both quasi-static bench-top test and rotor test.

The following conclusions can be drawn.

Analytical simulation: Passive, revolutions-per-minute-controlled actuation of the chord morphing mechanism can be realized by exploiting the unique properties of the von Mises truss, coupled with a retracting spring.

System design: 20% chord increase can be achieved using the von Mises truss, but this requires a good management of the limited available volume within the blade. Also, the mechanical realization of the prototype produced a complex mechanism, with many moving parts.

Experimental verification: Successful deployment and retraction of the rigid plate was achieved in both bench-top as well as rotor tests. Friction and alignment issues appear to have had a significant influence on system response, affecting the revolutions-per-minute range of actuation.

The design presented in this paper is a first attempt to validate the conceptual approach to passive chord morphing for a rotor blade using revolutions-per-minute variation. The overall analysis has been qualitatively verified. Further efforts should include a locking mechanism to prevent vibrations and a feasibility study on full-scale rotor-blade prototype. The addition of a balancing mass in the leading edge and a sealing system (to avoid unwanted intrusion of sand, water, etc.) should also be taken into account.

Acknowledgments

Support for this work by the U.S. Air Force of Office of Scientific Research (grant FA9550-11-1-0159, with David Stargel as Program Manager) is gratefully acknowledged. The authors greatly appreciate the contributions of Eric Hayden and Mihir Mistry both at the design stage and during experiments, as well as the assistance of Jose Palacios with the rotor tests at the AERTS at Penn State.

References

[1] Leon, O., Hayden, E., and Gandhi, F., "Rotorcraft Operating Envelope Expansion Using Extendable Chord Sections," *Proceedings of the 65th Annual Forum*, Vol. 1, American Helicopter Society (AHS), May 2009, pp. 1940–1953.

[2] Khoshlahjeh, M., Bae, E.-S., and Gandhi, F., "Helicopter Performance Improvement with Variable Chord Morphing Rotors," *Proceedings of the 36th European Rotorcraft Forum (ERF)*, Paris, Sept. 2010, Paper 92.

[3] Khoshlahjeh, M., and Gandhi, F., "Extendable Chord Rotors for Helicopter Envelope Expansion and Performance Improvement," *Journal of the American Helicopter Society*, Vol. 59, No. 1, 2014, pp. 1–10. doi:10.4050/JAHS.59.012007.

[4] Barbarino, S., Gandhi, F., and Webster, S. D., "Design of Extendable Chord Sections for Morphing Helicopter Rotor Blades," *Journal of Intelligent Material Systems and Structures*, Vol. 22, No. 9, 2011, pp. 891–905. doi:10.1177/1045389X11414077

[5] Bae, E.-S., and Gandhi, F., "CFD Analysis of High-Lift Devices on the SC-1094R8 Airfoil," *Proceedings of the 67th Annual Forum*, Vol. 1, American Helicopter Society (AHS), May 2011, pp. 106–123.

[6] Johnson, T., "Bistable Devices for Morphing Rotor Blades," Ph.D. Thesis, Pennsylvania State Univ., University Park, PA, 2010.

[7] Prabhakar, T., Gandhi, F., and McLaughlin, D., "A Centrifugal Force Actuated Variable Span Morphing Helicopter Rotor," *Proceedings of the 63rd Annual Forum*, Vol. 63, American Helicopter Society (AHS), May 2007, pp. 710–724.

[8] von Mises, R., "Über die Stabilitätsprobleme der Elastizitätstheorie," *Zeitschrift für Angewandte Mathematik und Mechanik*, Vol. 3, No. 6, 1923, pp. 406–422.

[9] Murray, G. J., and Gandhi, F., "The Use of Damping to Mitigate Violent Snap Through of Bistable Systems," *Proceedings of the ASME Conference on Smart Materials, Adaptive Structures and Intelligent Systems*, Vol. 1, SMASIS Paper 2011-4997, Sept. 2011, pp. 541–550.

[10] Barbarino, S., Pontecorvo, M. E., and Gandhi, F., "Energy Dissipation of a Bi-Stable von-Mises Truss Under Harmonic Excitation," *53rd AIAA/ASME/ASCE/AHS/ASC Structures, Structural Dynamics, and Materials Conference*, AIAA Paper 2012-1712, April 2012.

[11] Howlett, J. J., "UH-60A Black Hawk Engineering Simulation Program: Mathematical Model," NASA CR-166309, Dec. 1981.

Proceedings of the ASME 2013 Conference on Smart Materials, Adaptive Structures and Intelligent Systems
SMASIS2013
September 16-18, 2013, Snowbird, Utah, USA

SMASIS2013-3062

A BI-STABLE VON-MISES TRUSS FOR MORPHING APPLICATIONS ACTUATED USING SHAPE MEMORY ALLOYS

Silvestro Barbarino **Farhan S. Gandhi** **Rodolphe Visdeloup**

Mechanical, Aerospace and Nuclear Engineering Department, Rensselaer Polytechnic Institute, Troy, NY 12180, USA

Supmeca - Superior Engineering Institute of Paris, Toulon, France

ABSTRACT

The present study focuses on a bi-stable von-Mises truss (VMT), with integrated Shape Memory Alloy (SMA) wires which are resistively heated to provide the actuation force to transition the VMT from one stable equilibrium condition to the other, and back. This coupled VMT-SMA system can potentially be used in structural morphing applications. The paper considers in detail the design of the system, equilibrium between the VMT and the SMA wires, the initial pre-stress required in the two SMA wires, explains how the active (heated) SMA wire drives the VMT beyond the unstable equilibrium state, and the VMT in moving to the second stable equilibrium state pre-stresses the passive (unheated) SMA wire. The two SMA wires switch roles in moving the VMT back from the second to the first stable equilibrium state. A prototype is designed and fabricated and the transition of the VMT from one equilibrium state to the other, and back, is experimentally demonstrated. The governing differential equation representing the VMT behavior is coupled with equations representing the SMA behavior based on the Brinson thermo-mechanical model. The numerical predictions of system displacements versus temperature and time show good correlation with experimental results.

INTRODUCTION

Bi-stable or multi-stable structures, which can undergo large deformation as they transition between two or more stable equilibrium positions, are of significant interest in morphing applications. A very attractive feature of such structures is that the equilibrium positions require neither any power nor any locking mechanisms to hold. A morphing structure based on a bi-stable system can be designed to have its initial and final configurations corresponding to the first and second equilibrium stable positions. Transitioning between these two stable states, the system passes thru an unstable equilibrium point and undergoes a phenomenon known as snap-through.

Bi-stable and multi-stable systems are of particular interest for morphing applications. Hyer [1] and Cerami and Weaver [2] have investigated using unsymmetric composite laminates to create multi-stable shapes for morphing. The same concept was then adopted by Daynes et al. [3] to create a multi-stable air inlet, and by Diaconu et al. [4] to create a bi-stable plate used to extend the chord of an airfoil. In a similar application of bi-stable unsymmetric composite laminates, Schultz [5] developed a bi-stable airfoil-like device for wing twist morphing. Schultz also found that his device could be bi-stable without the help of unsymmetric laminates, and created a steel version of the same device.

Bi-stable elastic arches have also been considered for helicopter rotor blade morphing in a recent study by Johnson et al. [6,7]. Johnson envisioned that a single bi-stable elastic arch could be used to effectively extend the chord of a rotor blade. Figure 1 shows a schematic of the concept. That study used an arch clamped at both ends, and focused on the design of flexures to avoid high strains, leading to failure, when the arch transitioned from one stable equilibrium condition to the other. Another solution to limit high local strains was presented by Pontecorvo et al. [8], which envisioned a novel cosine profile for the arch to reduce peak stresses. One example of application of their concept for rotor blade chord morphing is shown in Figure 2.

In the present study, a bi-stable system known as a von-Mises truss (VMT) is adopted as replacement for the elastic arch to avoid the build-up of high strains leading to failure. Introduced by von-Mises [9] in 1923, a VMT is dynamically equivalent to a one-term Galerkin expansion of a continuous arch [10]. The VMT has been integrated with Shape Memory Alloys (SMAs) [11] to be used as actuators, exploiting the Shape Memory/Constrained Recovery effect [12]. Shape Memory Alloys have demonstrated their suitability for many

quasi-static applications [13] due to their high structural integration potential and energy density. By coupling the bi-stable von-Mises truss with Shape Memory Alloy actuators to command the snap through, a morphing structural assembly is created with the potential to be incorporated into more complex structures.

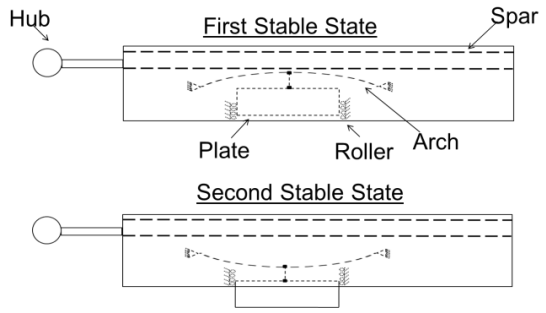

Figure 1. Schematics of bi-stable arch used for chord extension by Johnson et al. [7].

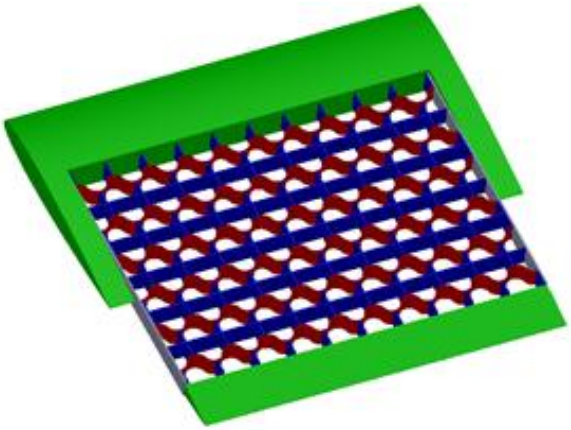

Figure 2. Isometric CAD view of a cellular structure with bi-stable arches (red) used for helicopter rotor blade chord morphing.

This paper focuses on two-way actuation (snap-through and snap-back) of the von-Mises truss. The proposed configuration uses two Shape Memory Alloy wires positioned to take advantage of the symmetric behavior of the von-Mises truss with respect to the unstable equilibrium. These wires are pre-strained by the von-Mises truss in either equilibrium state to achieve cyclic working.

Both numerical and experimental investigations are carried out. A semi-analytical model is developed in Matlab based on the numerical integration of the VMT governing equations capable of predicting the static and dynamic behavior of the VMT. This was then coupled with the Brinson thermo-mechanical model for the Shape Memory Alloys [12], to estimate the activation temperature and stress levels within the alloy required for actuation of the von-Mises truss. A prototype was built and tested. Experiments showed the cyclic, two-way actuation of the device and provided good correlation with the analysis.

CONCEPT

Von-Mises truss

A von-Mises truss bi-stable system is shown in Figure 3. The two planar, pin-jointed truss elements of length L_V are assumed to be rigid. All mass can be concentrated at the vertex of the truss to simplify the analysis. The truss elements are connected at the vertex, which can slide vertically in the x direction, and their free ends are allowed to slide in the horizontal direction z. A spring K_V inter-connects the free ends and provides stiffness for the truss. The initial angle of the truss elements is denoted by θ_0, positive counterclockwise, with the displacement defined positive clockwise and denoted θ. Barbarino et al. [14] derived the equation of motion by writing the kinetic and elastic potential energies of the system and using them in Lagrange's equation. The model was also statically and dynamically validated using ANSYS Finite Element analysis.

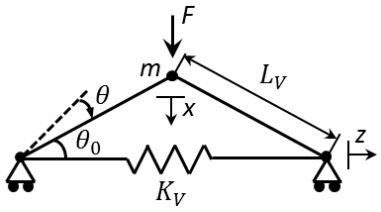

Figure 3. Diagram of a von-Mises truss system.

The static equation for such system is reported in Eq.1:

$$\frac{\left\{2K_V\left[sin(\theta_0)-\frac{x}{L_V}\right]\left[2L_V\sqrt{1-\left(sin(\theta_0)-\frac{x}{L_V}\right)^2}-2L_V cos(\theta_0)\right]\right\}}{\sqrt{1-\left(sin(\theta_0)-\frac{x}{L_V}\right)^2}}=F \quad (1)$$

The typical static behavior of a von-Mises truss is shown in Figure 4. The full displacement (stroke) of the VMT is defined by its geometry ($2L_V \sin\theta_0$), that is the amount of displacement corresponding to vertex travel from the first stable equilibrium position to the second one. The structure exhibits an initial positive stiffness up to a critical load (called F_{SNAP}). Thereafter, a region with negative stiffness is encountered, in which snap-through can occur. To have bi-stability, the force has to cross the zero level for a non-zero displacement, which always occurs for the von-Mises truss due to its symmetric behavior. In the last portion, the structure again exhibits positive stiffness. The slope of the initial portion of the curve (up to the critical force to induce snap-through) is representative of the stiffness of the VMT system. The initial stiffness of the VMT is useful to carry a static load with relatively small displacements. If a stiffer structure is needed, some parameters of the von-Mises truss such as the spring stiffness K_V or the initial angle θ_0 (or a combination of both) can be increased.

Figure 5 illustrates the force versus vertex displacement behavior of a "bi-stable" von-Mises truss under the conditions

of displacement control (solid line) and force control (dashed line). Under displacement input, it is possible to reproduce the negative stiffness behavior but not the snap-through, as the vertex position is hold during loading. On the other hand, under force input, it is possible to reproduce the snap-through but not the negative stiffness. Snap-through occurs in force control as soon as F_{SNAP} is exceeded and only if the vertex of the VMT is not held. Snap-through will be used in this study to induce large displacements with relatively small force and displacements in the Shape Memory Alloys wires.

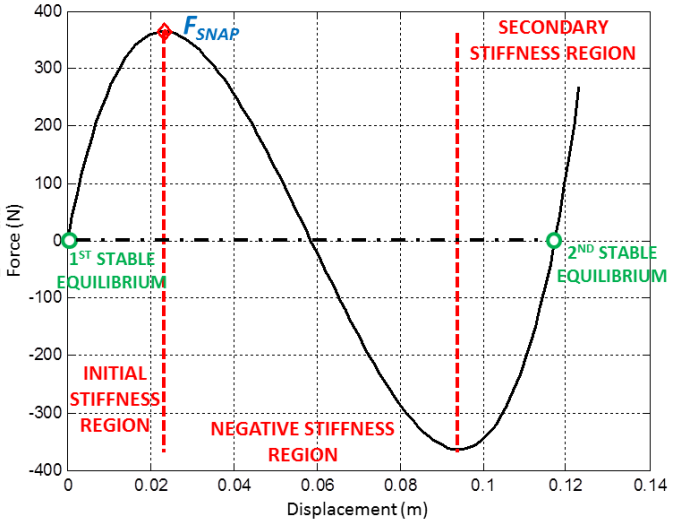

Figure 4. Static behavior of a VMT: markers individuate the force F_{SNAP} required to snap-through and the two stable equilibrium positions.

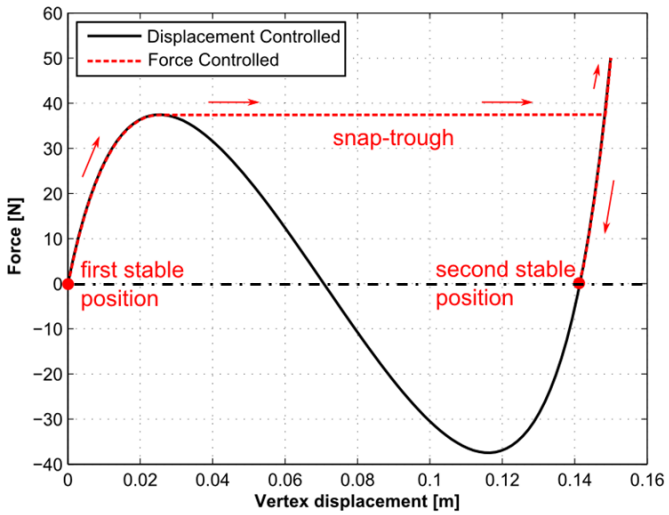

Figure 5. Displacement vs. force input on a bi-stable VMT system.

Shape Memory Alloys

Shape Memory Alloys, first discovered in 1932, are metal alloys (commonly nickel-titanium) that exhibit both the unique characteristics of large recoverable strains and large induced internal forces when exploiting the Shape Memory/Constrained Recovery effect [15].

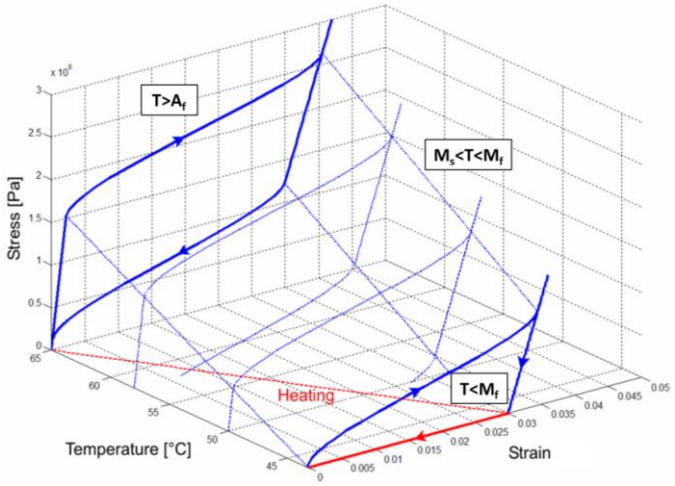

Figure 6. Typical stress-strain-temperature behavior of Shape Memory Alloys.

Aforementioned thermo-mechanical properties of SMAs are due to a crystallographic phase transformation from a body-centered cubic structure (austenite/parent phase, present at high temperatures) to a face-centered cubic structure (martensite/product phase, present at low temperatures), or vice versa. If the austenite temperature is lower than the environmental temperature, the so-called Super-elastic effect is exhibited upon changes in the internal stress state. Otherwise, the high residual strain may be recovered by a temperature change and the Shape Memory effect takes place (Figure 6).

SMAs are ideal for their favorable actuation performance-per-weight ratio, but are limited to low actuation frequencies (quasi-static) due to the thermal inertia. One of the major current drawbacks in engineering applications is the difficulty of fully characterizing their behavior, which is highly non-linear and load history dependent. In this study, the phenomenological model developed by Brinson et al. [12] is used. The basic assumption, inherited from Tanaka [16] and Liang & Rogers' [17] models, is that the thermo-mechanical process is fully described by three state variables: strain ε, temperature T and martensite volume fraction ξ. The martensite volume fraction is intended as a measure of the phase transformation and differentiated into stress induced ξ_S and temperature induced ξ_T, with $\xi = \xi_S + \xi_T$ and $0 < \xi < 1$. Relations for the two terms are derived by the phase kinetics. The constitutive relation for Brinson model is expressed in Eq.2

$$(\sigma - \sigma_0) = D(\xi)(\varepsilon - \varepsilon_0) + \Theta(T - T_0) + \Omega(\xi)(\xi - \xi_{S0}) \qquad (2)$$

where the subscript 0 represents the initial condition, σ is the stress, D is the modulus of elasticity, Θ is the thermal expansion coefficient and Ω is the transformation tensor. This equation shows that the stress consists of three parts (in the order): mechanical, thermal and induced by phase transformation.

Table 1. Selected SMA material properties.

Martensite Young modulus, E_M [GPa]	17
Austenite Young modulus, E_A [GPa]	50
Martensite start temperature, M_S (°C)	50
Martensite finish temperature, M_F (°C)	45
Austenite start temperature, A_S (°C)	60
Austenite finish temperature, A_F (°C)	70
Critical stress de-twinned martensite start [MPa]	75
Critical stress de-twinned martensite finish [MPa]	260
Thermal expansion coefficient Θ [MPa/°C]	0.55
Variation of austenite critical temperatures C_A with stress [MPa/°C]	12
Variation of martensite critical temperatures C_M with stress [MPa/°C]	12
Limit strain ε_L [%]	5.7
Ultimate elongation [%]	8

In this study, SmartFlex05 Ni-Ti wires with 480 μm diameter were provided by SAES Getters and used. The thermo-mechanical properties of the SMA necessary for the Brinson model are reported in Table 1. Some were provided by the manufacturer while others were measured experimentally performing mechanical tests in an Instron 4444 testing machine. Correlation between the Matlab implementation of the Brinson model and the characterization experiments was verified (not reported).

Combined VMT and SMA system

The coupling of the bi-stable von-Mises truss with Shape Memory Alloys as actuators has the potential to create a morphing structural assembly capable of undergoing large displacements with commanded changes in state and not requiring any locking mechanism. This could then be integrated into more complex structures.

Two-way actuation (snap-through and snap-back) was deemed of primary importance for such morphing mechanism. To achieve this goal, the ideal configuration would use heating of a set of pre-strained SMA wires (one or multiple) to actuate the VMT and induce snap-through in one direction. During the transition of the VMT from the first stable position to the other, the heated (martensite to austenite phase transformation) SMA wires can recover their initial pre-strain ε_{init}. This is possible because the SMA wires only need to apply sufficient force to reach the peak F_{SNAP} to initiate snap-through in the VMT. At this point no further action is required from the SMAs, which can be cooled down (austenite to martensite phase transformation). In the meanwhile, the VMT will cross the zero-force level for a non-zero displacement (corresponding to the unstable equilibrium position), and move towards the second stable equilibrium. While approaching this second position, the same SMA wires (or a different set) can be pre-strained again by the von-Mises truss due to its positive stiffness around the stable positions. If the SMA wires are positioned to take advantage of the symmetric behavior of the von-Mises truss with respect to the unstable equilibrium, the process can be inverted and snap-back induced.

This type of solution allows for cyclic, two-way actuation. However, it implies that the SMA wires must be initially attached to the VMT with the desired initial pre-strain. In addition, the VMT must be designed to be able to induce the desired amount of pre-strain in the SMAs. In this study, the VMT is designed to be able to pre-strain the SMAs in correspondence of its peak force F_{SNAP}. This is because after the first cycle the VMT will be able to apply a maximum pre-strain in the SMA wires in correspondence of its peak force. The two stable positions of the overall assembly will differ from the ones of the VMT alone, must be determined, and will be in the surroundings of F_{SNAP}.

For practical purposes, another critical feature of the selected design would include relatively short SMA wires capable of amplifying their recoverable strain to induce much larger displacements in the von-Mises truss. A value of recoverable strain of 3% in length for the SMAs is chosen in this study as a compromise between actuation performance, stability with cycles and fatigue life [18].

Several configurations were considered and then discarded because didn't meet the aforementioned requirements. Initially a configuration with two SMA wires aligned with the vertical motion of the vertex of the VMT, each pulling in one direction, was considered. The length required for this case was several times larger than the length of the links of the VMT and suitable only for very small values of the initial angle θ_0, and therefore was discarded. Another configuration considered SMA wires attached to the vertex and positioned to replicate the geometry of the links of the VMT. In this case, the SMA wires would completely recover their pre-strain upon reaching the horizontal position of the VMT. However, this position corresponds to an unstable equilibrium with zero force to hold, and therefore a source of bifurcation.

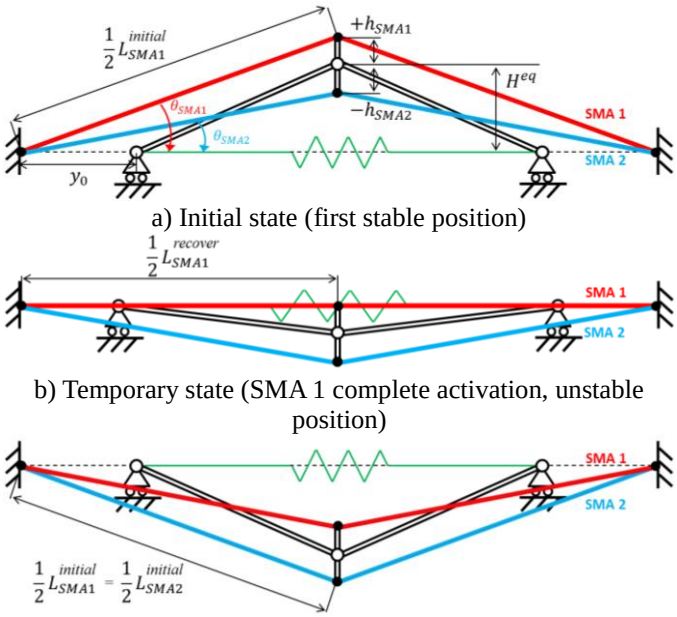

a) Initial state (first stable position)

b) Temporary state (SMA 1 complete activation, unstable position)

c) Final state (second stable position)

Figure 7. Schematics of the proposed combined configuration.

The final proposed solution is shown in Figure 7. It uses two Shape Memory Alloy wires positioned to take advantage of the symmetric behavior of the von-Mises truss with respect to the unstable equilibrium while minimizing their overall length. The SMA wires are constrained at both ends separately from the VMT, whose ends can instead slide horizontally. Connection to the vertex of the VMT is accomplished by means of a positive and negative offset, respectively (Figure 7a). This offset is the key feature allowing for two-way actuation. The SMA wires are heated independently (and not simultaneously) to induce snap-through motion in either direction. When the first (red) SMA wire is heated, the second (blue) stays at its low-temperature state (martensite) and behaves as a passive SMA to be pre-strained. Motion from the first to the second stable position is induced. As the first SMA wire approaches its complete strain recovery, the unstable equilibrium position of the VMT is crossed and the configuration shown in Figure 7b is reached. The presence of the offset allows moving the VMT beyond the unstable position, therefore guiding its motion towards the second stable position in a transient where the first SMA wire has no additional actuation authority. At this point heating of the first SMA is terminated. Both SMA wires are now "passive" and the spring K_V allows the VMT to reach the second stable position (Figure 7c). The process can then be inverted (heating of the second blue SMA wire only) for the snap-back motion.

The stiffness of the VMT must be tailored to the adopted SMA wires. For the two-way actuation to be possible, the VMT must be able to pre-strain both wires to the desired level by applying the required force along the longitudinal direction of each wire. It should be noted that the initial (Figure 7a) and final (Figure 7c) case must be symmetric, with the first and second SMA wires swapping their pre-strain levels in these two configurations. In each state the two wires have different pre-strain levels due to the geometry of the system. This is beneficial to the working of the assembly, as the active SMA possesses larger pre-strain (and actuation authority) than the passive one (which must be passively deformed).

Analysis of the geometry of the combined system allows deriving some useful relationships among the several parameters. Only the snap-through motion is described, as the snap-back is similar and requires inverting the first and second SMA wires as the passive and active one, respectively. One assumption made in the following is that the active SMA wire is expected to be able to fully recover its pre-strain (set to $\varepsilon_{init} = 3\%$ in length) thus reaching the horizontal position and length $L_{SMA}^{recover}$, as shown in Figure 7b and reported in Eq.3:

$$L_{SMA1}^{initial} = (1 + \varepsilon_{init}) L_{SMA}^{recover}. \tag{3}$$

This is due to the VMT exhibiting zero stiffness when approaching the unstable position, which also corresponds to the state of complete actuation for the heated SMA. It should also be noted that $L_{SMA}^{recover}$ is the same for both SMA wires once the completely horizontal position is reached.

The geometry of the VMT (L_V, θ_0) is defined first in the design process of the combined system. This would be set according to the requirements of the morphing structure to be actuated. Note that K_V is not defined at this point. As previously mentioned, the choice of the common working point between the von-Mises truss and the two SMA wires is crucial to the two-way cycling. The VMT must be able to pre-strain cycle after cycle both SMA wires. Therefore, the initial pre-strain in the wires (and associated stress levels) must be compatible with the force and displacement of the vertex of the von-Mises truss. In this study, a clear working point has been identified in the peak force F_{SNAP} of the VMT. This is representative of the maximum force that the VMT can exert on the SMA wires and must be sufficient to pre-strain both. Since the static equation of the VMT is known (Eq.1), the displacement at which this condition of maximum force occurs can be analytically determined (Eq.4)

$$x_{F_{SNAP}} = L_V sin(\theta_0) - \sqrt{[1 - cos(\theta_0)]^{2/3}}\,. \tag{4}$$

Other quantities in the new equilibrium position are:

$$\begin{aligned} H^{eq} &= L_V sin(\theta_0) - x_{F_{SNAP}} \\ \theta_0^{eq} &= sin^{-1}\left(\frac{H^{eq}}{L_V}\right) \\ y_0 &= \frac{L_{SMA}^{recover} - 2L_V cos\left(\theta_0^{eq}\right)}{2} \end{aligned} \tag{5}$$

with H^{eq} the new vertical position of the vertex and y_0 the distance between the free end of each link of the VMT and the grounding of the SMA wires.

Having defined the new initial equilibrium position for the VMT, and having set the amount of offset (h_{SMA1} and h_{SMA2}) for the two wires, the initial angles and lengths of both SMA wires can be found as

$$\begin{aligned} \theta_{SMA1}^{initial} &= cos^{-1}\left(\frac{1}{1 + \varepsilon_{init}}\right) \\ \theta_{SMA2}^{initial} &= tan^{-1}\left(\frac{H^{eq} - h_{SMA2}}{L_{SMA}^{recover}}\right) \\ L_{SMA1}^{initial} &= \frac{H^{eq} + h_{SMA1}}{sin\left(\theta_{SMA1}^{initial}\right)} \\ L_{SMA2}^{initial} &= \frac{H^{eq} - h_{SMA2}}{sin\left(\theta_{SMA2}^{initial}\right)} \end{aligned} \tag{6}$$

Other useful relationships include how the angles at which both SMA wires are mounted and their length changes with the vertical displacement x of the vertex of the von-Mises truss (Eq.7).

$$\theta_{SMA1} = \frac{sin^{-1}[L_V sin(\theta_0) + h_{SMA1} - x]}{\sqrt{[L_V sin(\theta_0) + h_{SMA1} - x]^2 + L_{SMA}^{recover\,2}}} \tag{7}$$

$$\theta_{SMA2} = \frac{sin^{-1}[L_V sin(\theta_0) - h_{SMA2} - x]}{\sqrt{[L_V sin(\theta_0) - h_{SMA2} - x]^2 + L_{SMA}^{recover\,2}}}$$

$$\varepsilon_{SMA1} = \sqrt{\frac{[L_V sin(\theta_0) + h_{SMA1} - x]^2 + L_{SMA}^{recover\,2}}{L_{SMA}^{recover\,2}}} - 1$$

$$\varepsilon_{SMA2} = \sqrt{\frac{[L_V sin(\theta_0) - h_{SMA2} - x]^2 + L_{SMA}^{recover\,2}}{L_{SMA}^{recover\,2}}} - 1$$

Therefore, the initial pre-strain values of both SMA wires are known (calculated for $x = x_{F_{SNAP}}$) and the correspondent necessary pre-stress levels (σ_{SMA1} and σ_{SMA2}) can be determined after characterizing the SMA material (or running the Brinson model with the set of parameters shown in Figure 1). The stress in both SMA wires can then be converted into force along the vertical motion of the vertex of the VMT according to Eq.8

$$\begin{aligned} F_{2SMAs} &= F_{SMA1} + F_{SMA2} \\ &= 2\sigma_{SMA1} A_{SMA1} sin(\theta_{SMA1}) \\ &\quad + 2\sigma_{SMA2} A_{SMA2} sin(\theta_{SMA2}) \end{aligned} \tag{8}$$

where A_{SMA1} and A_{SMA2} are the cross sections of each SMA wire.

Finally, the value of spring stiffness K_V necessary to combine the VMT and the SMA wires so to achieve $F_{SNAP} = F_{2SMA}$ can be determined from the static equation Eq.1 as

$$K_V = \frac{-F_{2SMA} \sqrt[3]{cos(\theta_0)}}{4L_V \left[cos(\theta_0) - \sqrt[3]{cos(\theta_0)}\right] \sqrt{1 - cos(\theta_0)^{2/3}}} \tag{9}$$

ANALYSIS

The static and dynamic behavior of the combined system comprising of a von-Mises truss and two SMA wires, and capable of two-way actuation, is investigated in this section. The geometry of the VMT system was defined first and the other quantities derived according to the design process exposed in the previous section. Table 2 summarizes the main parameters of the designed combined system.

Numerical analysis of the combined system has been carried out using MathWorks MATLAB R2012a. A dynamic equation of motion (Eq.10) has been derived starting from Lagrange's equation. The entire mass m is concentrated at the vertex. The action of the two SMA wires on the VMT system is accounted for in terms of external forces along the vertical motion of the vertex of the von-Mises truss. In particular, the active SMA wire applies a force in the direction of the snap-through motion while the passive one applies a resistive force (acts like a spring). The dynamic equation is numerically integrated using the ordinary differential equation solver ode23tb, based on an explicit Runge-Kutta formula [19]. The solution is obtained incrementally and at each step a function implementing the Brinson's model is used to calculate the evolution in martensite volume fraction, strain and stress (due to increase in temperature) in the SMA wires.

Table 2. Combined VMT and SMA system parameters.

θ_0 [deg]	30
θ_0^{eq} [deg]	18.7
L_V [mm]	100
K_V [N/m]	2100
$x_{F_{SNAP}}$ [mm]	18
F_{SNAP} [N]	22.2
$h_{SMA1} = h_{SMA2}$ [mm]	13
$L_{SMA1}^{initial}$ [mm]	187.9
$L_{SMA2}^{initial}$ [mm]	183.3
$L_{SMA}^{recover}$ [mm]	182.4
A_{SMA} [m^2]	1.96e(-5)
$\theta_{SMA1}^{initial}$	13.9
$\theta_{SMA2}^{initial}$	5.8
$\varepsilon_{SMA1}^{init}$ [%]	3.0
$\varepsilon_{SMA2}^{init}$ [%]	0.5
σ_{SMA1}^{init} [MPa]	201
σ_{SMA2}^{init} [MPa]	82

$$m\ddot{x} - \frac{\left\{2K_V\left[sin(\theta_0) - \frac{x}{L_V}\right]\left[2L_V\sqrt{1 - \left(sin(\theta_0) - \frac{x}{L_V}\right)^2} - 2L_V cos(\theta_0)\right]\right\}}{\sqrt{1 - \left(sin(\theta_0) - \frac{x}{L_V}\right)^2}} + F_{SMA}^{passive} + F_{SMA}^{active} = 0 \tag{10}$$

To distinguish between the snap-through and the snap-back motion, a boolean variable is introduced in the simulation to switch the SMA wire being heated while keeping the other passive (at low, martensitic temperature). Results for the snap-through motion only (one way) are presented in this section, as the snap-back motion is perfectly symmetrical. A single cycle of heating-cooling for the active SMA wire is presented.

Figure 8 shows the vertical displacement of the vertex of the VMT as a function of the activation temperature of the active SMA wire (the other wire is kept at a constant temperature of 20°C). The simulation finds the initial equilibrium position of the combined system to be at 18.3 mm (point A) displacement, close to the 0.018 m originally estimated in the design process ($x_{F_{SNAP}}$ in Table 2). As temperature in the active SMA wire is increased, the VMT snaps-through up to 48 mm (point B). This corresponds to the VMT being almost horizontal and close to its unstable position. In this position both passive and active SMA wires have roughly the same amount of strain and the active SMA has to start pre-straining the passive one. As temperature keeps increasing, the active SMA reaches its horizontal position (x = 63 mm, point C) and has fully recovered its pre-strain, therefore it is not able to apply any additional force. Further increase in temperature does not produce any additional force or motion. Reducing the temperature, on the other hand, allows reaching the second equilibrium position for the combined system (x = 83.4 mm, point D).

The presence of sudden jumps in the displacement of the vertex of the VMT is due to the crossing of the negative stiffness region of the VMT (Figure 9) and the SMA wires alternatively going slack or suddenly undergoing tension. These discontinuities cannot be eliminated and are part of the behavior of the designed system.

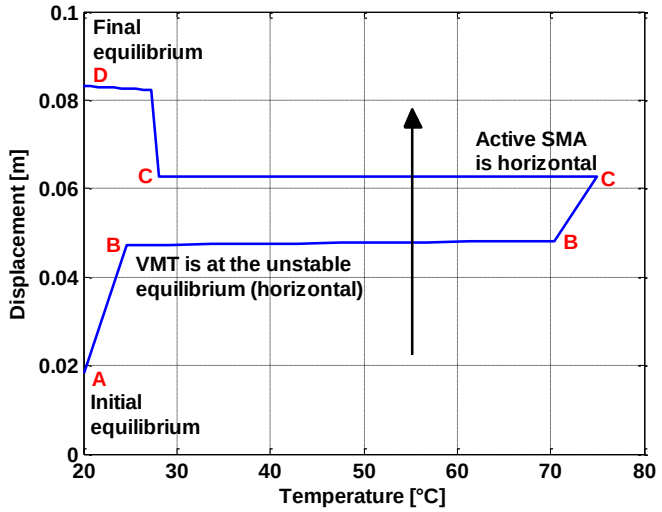

Figure 8. VMT vertex displacement vs. activation temperature of active SMA wire.

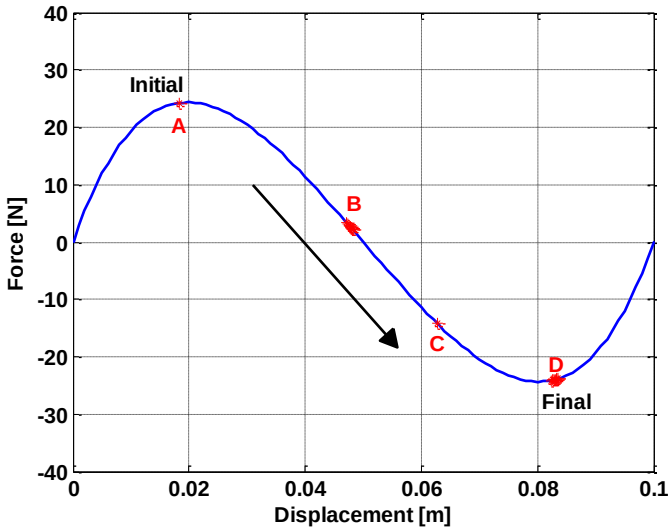

Figure 9. VMT vertex displacement vs. activation temperature of active SMA wire.

Figure 10 shows the evolution of the strain within the SMA wires as a function of the displacement of the vertex of the VMT. The simulation estimates initial pre-strain values for both wires slightly larger than the predictions from the design process ($\varepsilon_{SMA1}^{initial} = 0.032$ and $\varepsilon_{SMA2}^{initial} = 0.006$). The active SMA wire (solid red curve) recovers its pre-strain completely corresponding to 63 mm (point C) vertex vertical displacement, at which point the wire is perfectly horizontal. When the horizontal position is overcome, its strain increases again up to the initial pre-strain value for the passive SMA wire. On the other hand, the passive SMA wire (dashed blue curve) follows a different evolution. As the VMT moves, it becomes loose and its pre-strain does not change. After snap-through occurs, the VMT deforms the passive wire up to the pre-strain level necessary for the snap-back motion.

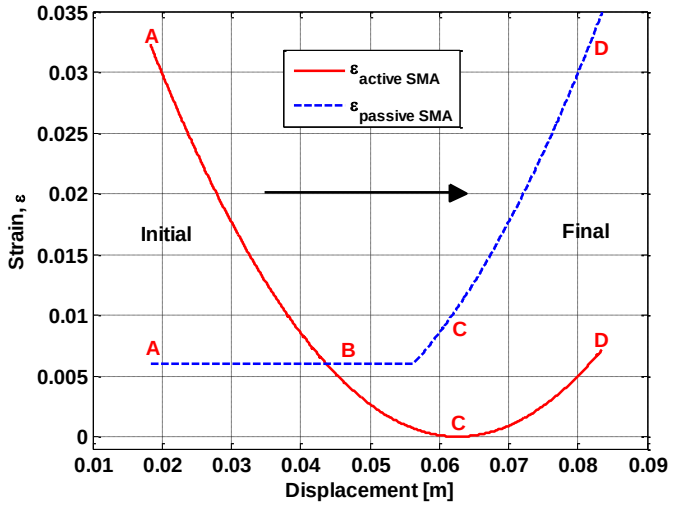

Figure 10. Strain in the SMA wires vs. VMT vertex displacement.

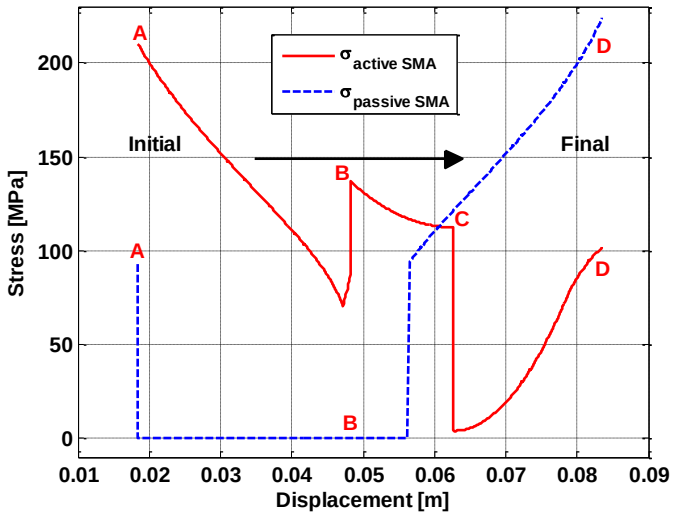

Figure 11. Stress in the SMA wires vs. VMT vertex displacement.

The presence of slack in the SMA wires can be appreciated in Figure 11. Initial stress values in both SMA wires are very close to the ones estimated in the design phase. The passive SMA wire has a straightforward behavior. As soon as the snap-through motion begins, the passive wire becomes loose and its stress level drops. After the horizontal position is crossed and the slack is removed, the stress increases. The active SMA, on the other hand, reduces its stress level from the initial value due to the snap-through behavior of the VMT, which enters the

negative stiffness region and exhibits a reducing resisting force. This terminates around $x = 48$ mm (point B), when the VMT has reached its unstable position but the active SMA must overcome the resistance of the passive wire and start stretching it. At $x = 63$ mm (point C) the active SMA wire is completely horizontal and cannot influence the motion of the VMT any further. Its internal stress levels are close to null as only the passive SMA wire is offering some resistance. From this point and up to $x = 83.4$ mm (point D), the VMT alone is able to stretch both SMA wires, increasing their internal stress level. It should be noted that the final values of internal stress of both SMA wires are similar (and inverted) to their initial stress levels. The stress levels within the active and passive SMA wires can also be converted into the vertical active and resistive force, respectively, acting on the vertex of the von-Mises truss (Figure 12).

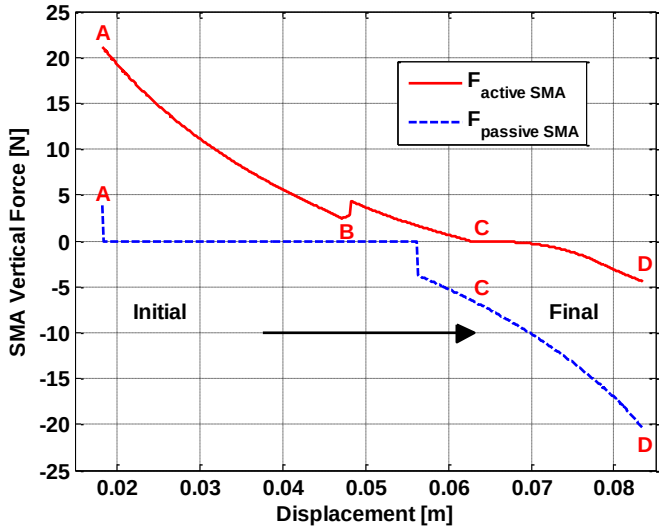

Figure 12. Vertical force in the SMA wires vs. VMT vertex displacement.

As a final note for this section, the Brinson phenomenological model presents some shortcomings when temperature and stress of the SMA wire change simultaneously, as discussed by Elahinia [20]. In the proposed configuration, this occurs when the VMT system transitions between the positive and negative stiffness regions. During heating, the SMA wire actuates the VMT by applying an increasing vertical force to the vertex of the VMT up to F_{SNAP}. As soon as snap-through is induced, the VMT tends to reach the second stable equilibrium and the SMA wire becomes slack, therefore experiencing a drop in internal stress. At the same time, cooling of the SMA begins. The Brinson model is not able to correctly estimate what happens during this phase (between points A and B). However, due to the very fast occurrence of snap-through combined with the SMA wires going alternatively slack during this motion, and the interest in this preliminary study in achieving and demonstrating two-way actuation, this shortcoming has been neglected.

EXPERIMENTS

Prototype

An experimental prototype for the proposed combined VMT and SMA system was built to validate the numerical simulations. The use of commercial off-the-shelf components for ease of use affected the design of the final prototype (Figure 13) and its main parameters are summarized in Table 3.

Table 3. Main parameters of the experimental prototype.

θ_0 [deg]	12
L_V [mm]	100
K_V [N/m]	2086
$h_{SMA1} = h_{SMA2}$ [mm]	13
$L_{SMA1}^{initial}$ [mm]	178.5
$L_{SMA2}^{initial}$ [mm]	174.8
$L_{SMA}^{recover}$ [mm]	174.1
$\varepsilon_{SMA1}^{init}$ [%]	2.5
$\varepsilon_{SMA2}^{init}$ [%]	0.4

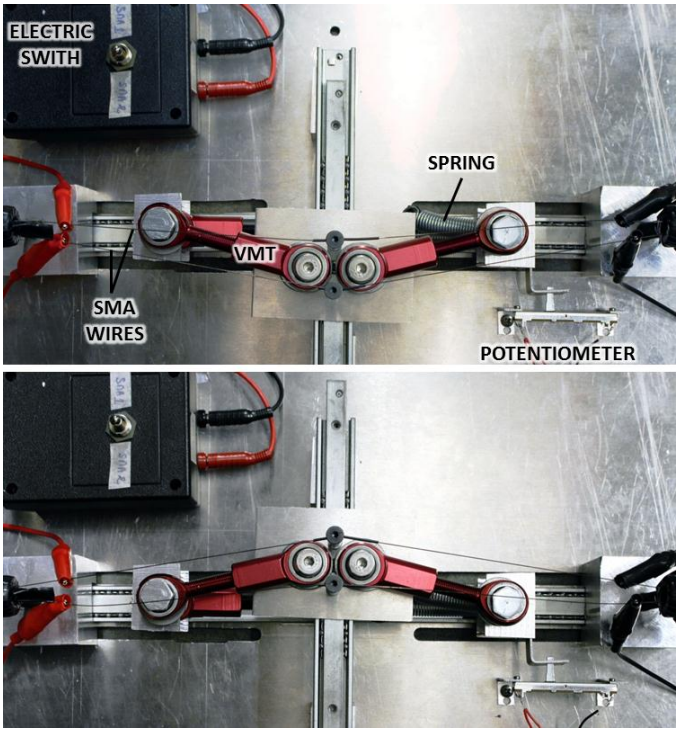

Figure 13. Experimental prototype.

The rigid links of the VMT have built-in pin-joints at both ends. One end of each link can move horizontally on sliders. The other converges in the vertex of the VMT. As opposed to the model, the links don't merge in a single pin-joint but are positioned as close as possible, thus allowing keeping both links in the same plane. The vertex of the VMT is therefore

constituted of a plate which can slide vertically on a rail, connects to the rigid links of the VMT and hosts also the supports for the SMA wires. These supports are bolts with holes that allow the wire to pass-through. Electrical insulation is used when connecting the SMA wires to the rest of the prototype as the heating is achieved by means of Joule effect. Convective cooling is then used to induce the opposite phase transformation. The SMA wires are connected to fixed boundaries at the extreme ends. The stiffness of the VMT is due to a tension spring located underneath the rigid links and connected to their sliding ends by means of a spacer.

Two separate electric circuits are connected to each SMA wire and commanded by an external switch. A Tektronix PWS4000 DC power supply is used as source of electrical current to heat the SMA wires alternatively. The power output and the reading from a K-type thermocouple are sent to a NI DAQ 6212 acquisition system commanded by LabView software. Also, measurements from a linear potentiometer attached to the sliding base of one of the VMT links records the horizontal displacement z. This motion is then related to the vertical displacement of the vertex of the VMT using Eq.11

$$x = L_V sin(\theta_0) - L_V sin\left[cos^{-1}\left(cos(\theta_0) + \frac{z}{L_V}\right)\right]. \quad (11)$$

A 1.3 A electrical current was used during the experiments. This value was chosen as a trade-off between (1) the achievement of the complete activation temperature and (2) actuation time, and (3) the time needed by the thermocouple to read increments in temperature (due to thermal inertia).

Tests and correlations

Experiments showed the occurrence of commanded snap-through and snap-back motion by alternating the Joule heating of the two SMA wires. Two sets of data will be presented in this paper. The first shows the experimental occurrence of the two-way actuation.

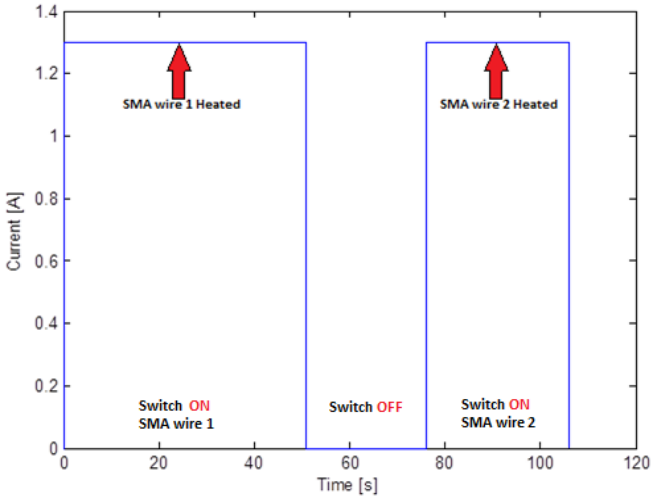

Figure 14. Commanded activation of the SMA wires for two-way actuation.

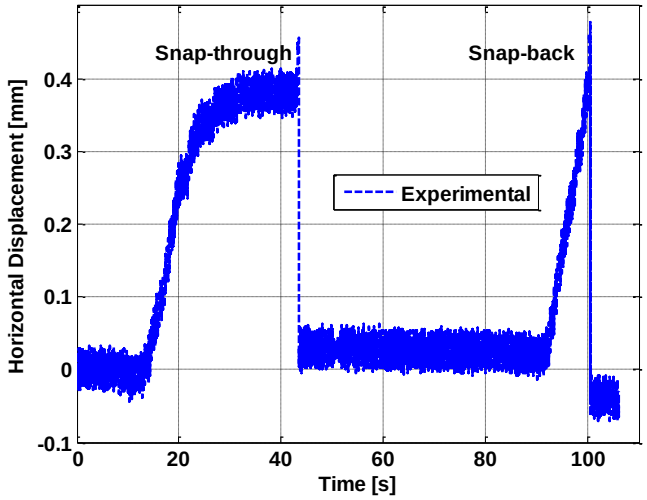

Figure 15. Two-way actuation: potentiometer.

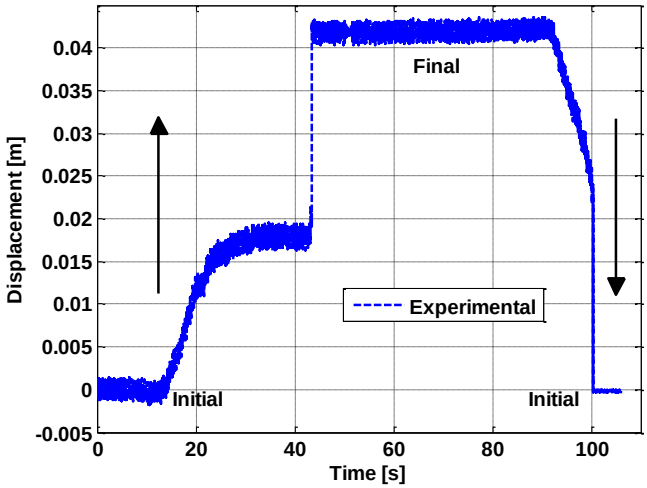

Figure 16. Two-way actuation: VMT vertex displacement.

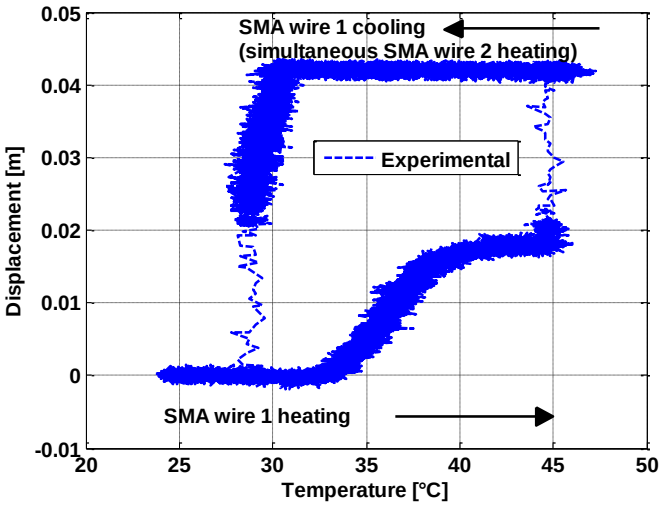

Figure 17. Two-way actuation: VMT vertex motion vs. temperature.

Figure 14 illustrates the commanded activation of the SMA wires, and Figure 15 and 16 the measured horizontal and vertical displacement of the VMT as a function of time, respectively. From these figures it is possible to infer that the experimental snap-back motion is faster than the snap-through one. During the forward motion, the prototype takes roughly 25 seconds (roughly between 15 and 40 seconds in Figure 15) to reach the unstable equilibrium and then snaps-through. It was established that minor fabrication asymmetries led to the prototype not exhibiting a completely symmetrical behavior in the two directions of motion. Figure 17 shows the displacement of the vertex of the VMT as a function of the temperature of the active SMA wire. Note that when the first SMA wire starts cooling, the other SMA wire is heated to induce snap-back.

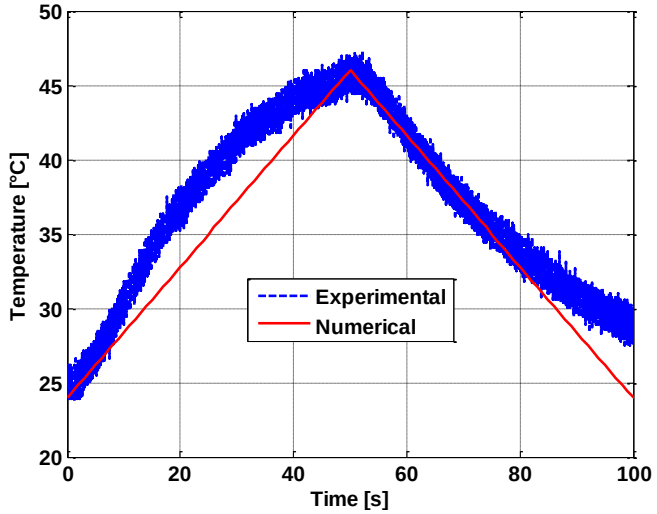

Figure 18. Temperature profile for the active SMA.

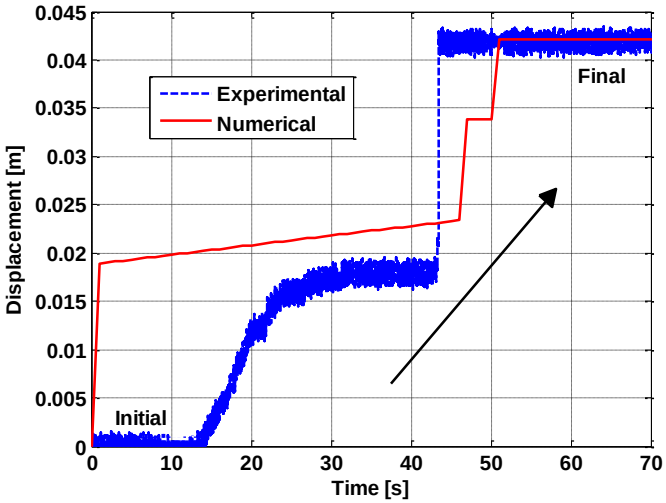

Figure 19. One-way actuation: displacement vs. time.

The second set of data focuses on the one way actuation, which is correlated with the numerical simulation. Figure 18 illustrates the experimental temperature profile for the active SMA wire, as measured by the thermo-couple, and the one modeled in the simulation. Figure 19 and 20 show a good correlation between the model and the experiments in terms of transition temperatures and displacement of the VMT. Discrepancies in the profiles of the initial motion, up to the unstable equilibrium point, are attributed to the asymmetric behavior of the prototype already established in the previous set of tests, and not implemented in the modeling.

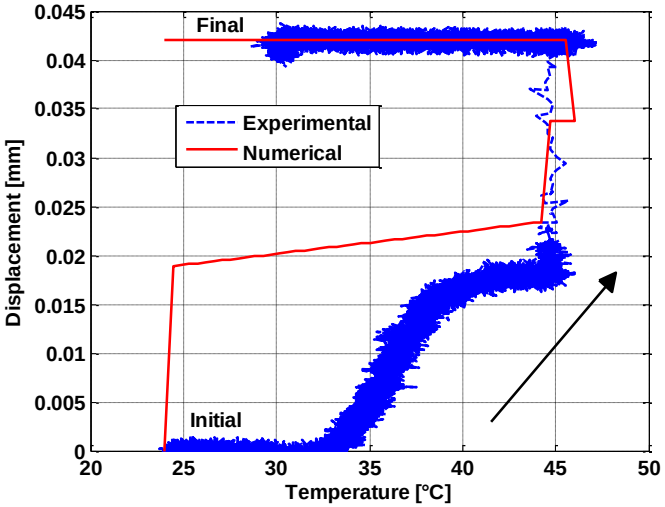

Figure 20. One-way actuation: displacement vs. temperature.

CONCLUSIONS

This paper examines the bi-stable behavior of a von-Mises truss (VMT) combined with Shape Memory Alloys (SMAs) for morphing applications. Shape Memory Alloys command the changes in state of the bi-stable von-Mises truss, inducing snap through in both directions. A morphing structural assembly is created with the potential to be incorporated into more complex structures.

The proposed configuration is a first example in literature of a bi-stable mechanism controlled by SMAs and capable of amplifying their actuation performance. The limited recoverable strain of the SMA is used to induce the snap-through motion of the VMT which produces relatively large displacements. Once in either equilibrium position, the prototype can hold it without a locking mechanism. A working prototype has been built and tested, which showed the occurrence of commanded snap-through and snap-back motion by alternating the activation of two SMA wires. Experiments correlated well with the model and validated the concept presented herein. Further developments will try to optimize the geometry and design of the system to further amplify its overall stroke.

ACKNOWLEDGMENTS

The authors gratefully acknowledge the support for this work by the Air Force of Office of Scientific Research (Grant FA9550-11-1-0159, with Dr. David Stargel as Program Manager).

REFERENCES

[1] Hyer, M.W., "Some Observations on the Cured Shape of Thin Unsymmetric Laminates," Journal of Composite Materials, 15: 175-194, March 1981.

[2] Cerami, M., and Weaver, P.M., "Characterization of Unsymmetric Cross-ply Laminate Deflections Using Orthogonal Polynomials," AIAA Structures, Structural Dynamics, and Materials Conference, April 2008.

[3] Daynes, S., Weaver, P.M., and Trevarthen, J.A., "A Morphing Air Inlet with Multiple Stable Shapes," Journal of Intelligent Material Systems and Structures, 22: 961-973, June 2011.

[4] Diaconu, C.G., Weaver, P.M., and Mattonni, F. "Solutions for Morphing Airfoil Sections Using Bistable Laminated Composite Structures," AIAA Structures, Structural Dynamics, and Materials Conference, April 2007.

[5] Schultz, M.R., "A Concept for Airfoil-like Active Bistable Twisting Structures," Journal of Intelligent Material Systems and Structures, 19: 157-169, February 2008.

[6] Johnson, T., Frecker, M., and Gandhi, F., "A Bistable Mechanisms for Chord Extension Morphing Rotors," Proceedings of the 2009 SPIE Conference on Smart Structures and Materials, San Diego, California, March 8-12, 2009.

[7] Johnson, T., Gandhi, F., and Frecker, M., "Modeling and Experimental Validation of a Bistable Mechanism for Chord Extension Morphing Rotors," Active and Passive Smart Structures and Integrated Systems, SPIE, Vol. 7643, 2010.

[8] Pontecorvo, M.E., Barbarino, S., Murray, G.J., and Gandhi, F., "Bi-stable Arches for Morphing Applications," J. of Intelligent Material Systems and Structures (JIMSS), vol.24, no.4, 2013, pp.274-286.

[9] Mises R., "Uber die Stabilitatsprobleme der Elastizitatstheorie," Zeitschrift Angewandte Mathematik und Mechanik, Vol. 3, 406, 1923.

[10] Blair, K. B., Krousgrill, C. M., and Farris, T. N., "Nonlinear Dynamic Response of Shallow Arches," Proceedings of the 33rd AIAA/ASME/ASCE/ASC Structures, Structural Dynamic and Material Conference, 13-15 April 1992, pp. 2376-2384.

[11] Buehler W.J., Gilfrich J.V., and Wiley R.C., "Effect of low-temperature phase changes on the mechanical properties of alloys near composition TiNi," Journal of Applied Physics, Vol.34, 1963, pp. 1475.

[12] Brinson L.C., Bekker A., and Huang M., "Deformation of Shape Memory Alloys due to Thermo-Induced Transformation", J. of Intelligent Material Systems and Structures, Vol.7, No.1, 1996, pp. 97-107.

[13] Barbarino, S., "Smart Morphing Concepts and Applications for Advanced Lifting Surfaces," Ph.D. Thesis, University of Napoli "Federico II", Napoli, Italy, November 2009.

[14] Murray, G. J., and Gandhi, F. S., "The Use of Damping to Mitigate Violent Snap-through of Bistable Systems," Proceedings of the ASME 2011 Conference on Smart Materials, Adaptive Structures & Intelligent Systems (SMASIS), Phoenix, Arizona, USA, 18 September 2011, paper SMASIS2011-4997.

[15] Kauffman, G.B., and Mayo, I., "The metal with a memory," Invent. & Tech., vol.9, no.2, 1993, pp.18-23.

[16] Tanaka K., "A Thermomechanical Sketch of Shape Memory Effect: One-Dimensional Tensile Behaviour," Res. Mech., vol.18, no.3, 1986, pp.251-263.

[17] Liang, C., and Rogers, C.A., "One-Dimensional Thermomechanical Constitutive Relations for Shape Memory Material," J. of Intelligent Material Systems and Structures, vol.1, no.2, 1990, pp.207-234.

[18] Shimizu, K., and Tadaki, T., "Shape Memory Alloys," Funakubo H. Ed., Gordon and Breach Science Publishers, New York, 1987, 1987, pp.1-60.

[19] The MATHWORKS, Inc., "ode23, ode45, ode113, ode15s, ode23s, ode23t, ode23tb: Function (MATLAB®)", R2010b ed. Natick, MA, February 2010.

[20] Elahinia, M.H., and Ahmadian, M., "An enhanced SMA phenomenological model: I. The shortcomings of the existing models," Smart Materials and Structures. Vol.14, No.6, 2005, pp. 1297-1308.

ICAST2014 #056

Design studies on cellular structures with pneumatic artificial muscle inclusions for modulus variation

Michael E. Pontecorvo, Robert J. Niemiec, Farhan S. Gandhi *

Rensselaer Polytechnic Institute, Troy, NY 12180, USA

Abstract

This paper presents a novel variable modulus cellular structure based on a hexagonal unit cell with pneumatic artificial muscle (PAM) inclusions. The cell considered is pin-jointed, loaded in the horizontal direction, with three PAMs (one vertical PAM and two horizontal PAMs) oriented in an "H" configuration between the vertices of the cell. A method for calculation of the hexagonal cell modulus is introduced, as is an expression for the balance of tensile forces between the horizontal and vertical PAMs. An aluminum hexagonal unit cell is fabricated and simulation of the hexagonal cell with PAM inclusions is then compared to experimental measurement of the unit cell modulus in the horizontal direction over a pressure range up to 682 kPa. An increase in cell modulus of 200% is demonstrated experimentally, with a minimum change in cell geometry. A design study via simulation predicts that differential pressurization of the PAMs up to 1992 kPa can increase the cell modulus in the horizontal direction by a factor of 6.66. A design study considering parametric variation in cell angle, vertical to inclined wall length ratio, and PAM contraction ratios showed that changes in modulus of over 1000% were possible by differential pressurization of the PAMs. Both experiment and simulation show that this concept provides a way to decouple the length change of a PAM from the change in modulus to create a structural unit cell whose in-plane modulus in a given direction can be tuned based on the orientation of PAMs within the cell and the pressure supplied to the individual muscles.

1. INTRODUCTION

A recent study by Pontecorvo et al.[1] proposed a framework in which rigid-link, pin-jointed hexagonal unit cells can be supported internally by a variety of passive inclusions – such as springs[1], buckling beams[2], or dampers[2,3] – in order to tailor the in-plane behavior of the cells to specific functions. It was found that three inclusions between the vertices were necessary for the cell to be statically determinate. In the case of linear spring inclusions, expressions for the modulus of the cell in the vertical and horizontal directions were derived based on the stiffness of the springs[1].

This work builds on the concept proposed by Pontecorvo et al. by including pneumatic artificial muscles (PAMs) as semi-active, variable stiffness springs within the unit cell. PAMs were first patented by Gaylord[4] in 1958 and used by McKibben as orthotic devices in the 1950s[5]. Each PAM consists of a cylindrical flexible rubber bladder surrounded by a braided mesh of fibers that are connected to end

* Corresponding author, E-mail: fgandhi@rpi.edu

fittings. When the bladder is inflated with pressure from a fluid (usually air), the radial expansion tensions the braided fibers and causes the muscle to contract axially. A characteristic of PAMs is that the stiffness of the actuator is directly proportional to pressure. Several researchers have explored using this property to vary the stiffness or elastic modulus of structures. Philen[6-10], for example, has demonstrated experimentally that flexible fluidic matrix composite (F^2MC) tubes can change modulus by a factor of 50. F^2MCs are similar to PAMs but with fibers embedded in the bladder (in place of the external braided mesh) to form a composite cylinder. They are typically filled with high bulk modulus fluid rather than air. Philen[8] and Chen et al.[11] have investigated using F^2MC tubes embedded within an elastomeric matrix to create variable stiffness panels. Kim et al.[12] applied the F^2MC in a similar way to create a variable bending stiffness composite beam.

The current study presents a novel variable modulus structural element by incorporating PAMs within a hexagonal unit cell. Using an orthogonal arrangement of PAMs provides a way to largely decouple the length change of a PAM from the change in modulus to create a structural unit cell whose in-plane modulus in a given direction can be tuned based on the orientation of PAMs within the cell and the pressure supplied to the individual muscles. These unit cells can then be repeated in-plane or stacked in layers to create a composite structure whose modulus and load-deformation coupling can be actively tuned using fluid pressure. The paper describes the fabrication of a pin-jointed hexagonal unit cell with two horizontal PAMs and one vertical PAM arranged in an "H" configuration, as seen in Figure 1. The cell is loaded in the horizontal (x) direction and its modulus (E_x) is measured for increasing values of pressure in the PAMs. The measurements are compared to simulation results and the model is further used to predict the largest changes in modulus that could be achieved through differential pressurization of the horizontal and vertical PAMs. The paper provides an understanding of the mechanisms by which cell modulus change is achieved, and also presents a design study examining achievable modulus change in various cell geometries.

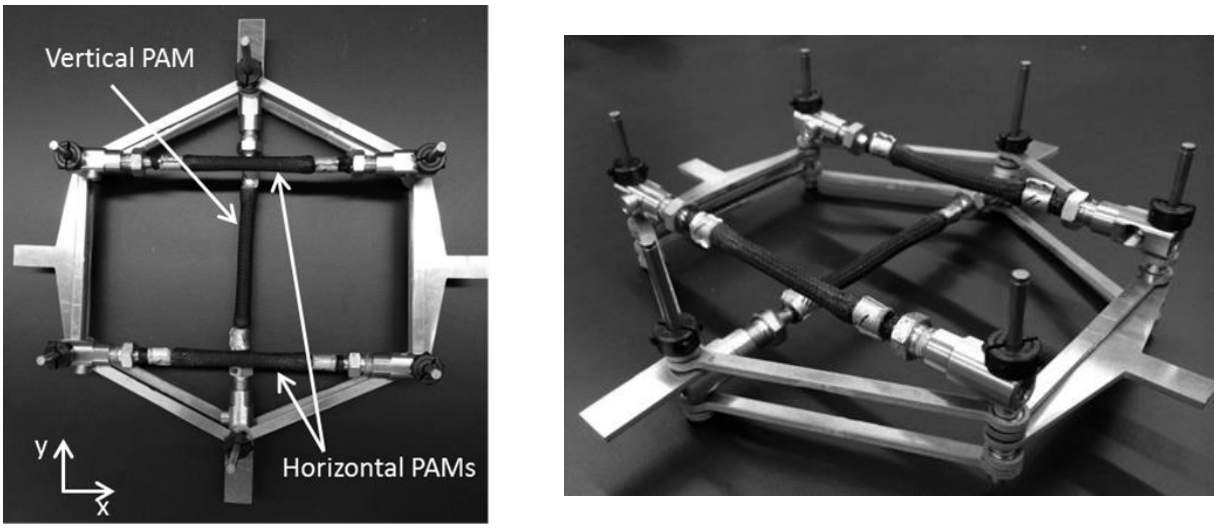

(a) (b)

Figure 1. (a) Top view and (b) isometric view of the prototype hexagonal cell with one vertical PAM and two horizontal PAMs

2. ANALYSIS

2.1 PAM model

The constitutive behavior of an individual PAM was modeled based on the modeling approach for PAMs developed by Kothera et al.[13] A schematic on which their model is based is shown in Figure 2. The PAM comprises a tubular elastomeric bladder of active length L, outer radius R, wall thickness t, and elastic modulus E, over which a single fiber of length b is wrapped N times at an angle θ_b. Kothera et al. assume that the volume of the bladder material, V_b, does not change from its original volume, V_{b0}, as described in Equation 1, and use this relationship to find the bladder wall thickness t at any muscle length L. When pressurized to a pressure P, stresses in the bladder develop in the circumferential direction, σ_c, and in the axial direction, σ_z. The corresponding axial force in the bladder and tension, T, in the fiber are in equilibrium with the applied axial force, F, at the free end of the PAM. The result is Equation 2, which relates the applied axial force to the length of the PAM for a given pressure. This equation is used throughout the current work to simulate the force-displacement behavior of the individual PAMs and is integrated into the hexagonal unit cell to calculate its modulus. A non-cylindrical tip-shape correction was not applied to Equation 2 because it was not found to improve the correlation of the simulation with experiment, nor was friction included in the model.

$$V_b = L(\pi R^2 - \pi(R-t)^2) = V_{b0} = L_0\left(\pi {R_0}^2 - \pi(R_0 - t_0)^2\right) \quad (1)$$

$$F = \frac{P\left(3L^2 - b^2\right)}{4N^2\pi} + EV_b\left(\frac{1}{L_0} - \frac{1}{L}\right) + P\left(\frac{V_b}{L} - \frac{tL^2}{2\pi RN^2}\right) + \frac{EL}{2\pi RN^2}(tL - t_0L_0) \quad (2)$$

Before introducing the PAMs into the hexagonal cells, tensile load versus contraction ratio ($\mathrm{CR} = L/L_0$) measurements for individual PAMs were obtained and compared to simulation results based on Equation 2. For the simulation, the two muscle parameters that were measured most precisely – the muscle active length and bladder wall thickness – were directly used as input parameters. Starting with initial estimates, the muscle braid length, b, initial radius, R_0, and bladder elastic modulus, E, were adjusted to best match the experimental results. The values of bladder elastic modulus and initial radius were taken to be the same for both the horizontal muscles and the vertical muscle (since they were fabricated from the same tube). The final values chosen for the simulation are listed with the measured values in Table 1. Owing to the geometry of a regular hexagonal cell, the horizontal PAMs' initial active length, L_0, and braid length, b, are shorter than those of the vertical PAM. The values of b used in the simulation correspond to a braid angle of 53.58° for the vertical PAM and 52.39° for the horizontal PAMs.

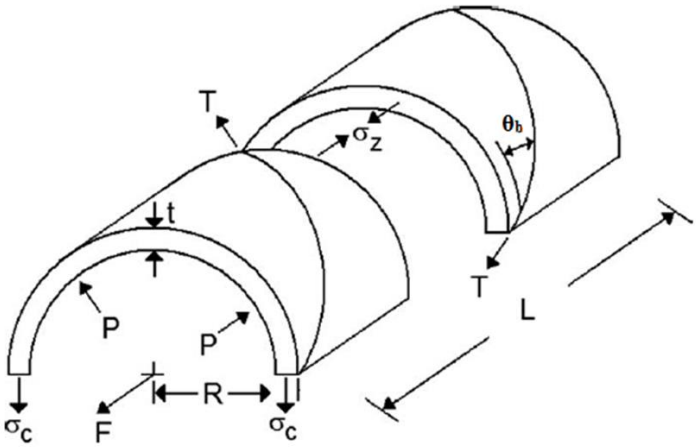

Figure 2. Schematic of Kothera et al.'s PAM force-balance model[13]

Table 1. PAM parameters

Parameter	Vertical PAM		Horizontal PAMs	
	Measured	Simulation	Measured	Simulation
L_0 (m)	0.0909	0.0909	0.0507	0.0507
b (m)	-	0.1130	-	0.0640
t_0 (m)	0.0008	0.0008	0.0008	0.0008
R_0 (m)	0.0043	0.0048	0.0043	0.0048
E (MPa)	-	3	-	3

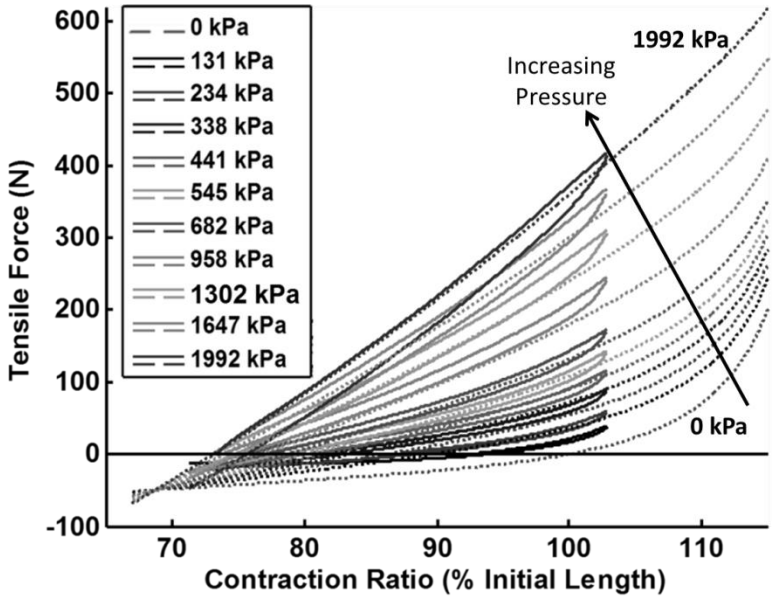

Figure 3. Tensile force versus contraction ratio over a range of pressures for the vertical PAM. Dotted lines represent simulation, solid lines represent measured data.

Figure 3 is a plot of the tensile force as a function of contraction ratio for the vertical PAM over a range of pressures up to 1992 kPa. The solid lines represent measured experimental data obtained from tests conducted in an Instron 4204 machine, and the dotted lines represent the simulation results based on the parameters listed in Table 1. The vertical muscle was tested at pressures from 131 to 1992 kPa up to a contraction ratio of 103%. The simulation is plotted at the same pressures as the experiment with an additional curve at 0 kPa, and up to a contraction ratio of 115%. At pressures below 441 kPa, the simulation slightly overpredicts the tensile force of the actuator vis-à-vis the experimental results. Above 441 kPa the simulations slightly underpredict the experimental curves until the final pressure of 1992 kPa. This spread of the simulation results are sensitive to the chosen simulation parameters and the results presented in Figure 3 reflect the best fit of the simulation to the experiment over the range of pressures. For clarity, Figure 4 shows a comparison of the vertical PAM experimental and simulation results at a single pressure of 682 kPa. Overall, the slope of the simulated curve compares well with the experiment, but the predicted free length (corresponding to zero tensile force) is slightly higher than the experiment, and the simulation shows less nonlinearity (stiffening behavior) at higher contraction ratios. In the current study the PAMs never enter compression when arranged in the hexagonal cell for the range of pressures and displacements investigated.

Results similar to those seen in Figure 3 are presented in Figure 5 for the horizontal PAMs. The experimental data (solid curves) represents the average of the two horizontal PAMs while the simulation results are presented by the dashed curves. The PAM blocked force and free length for increasing pressures (obtained from Figure 3 and 5) are summarized in Figure 6a and 6b, respectively. In Figure 6a,

the blocked force of the vertical PAM is larger than the blocked force of the horizontal PAMs in both simulation (by 11.4% at 1992 kPa) and experiment (by 9.9% at 1992 kPa). Likewise, in Figure 6b, the free length of the vertical PAM is always lower than the free length of the horizontal PAMs. If the initial braid angle, θ_{b0}, of the PAMs were equal, the simulation curves of the vertical and horizontal PAMs would lie on top of each other. The difference then corresponds to the difference in initial braid angle (53.58^o for the vertical muscle, and 52.39^o for the horizontal PAMs), which increases the blocked force and decreases the free length for the vertical PAM over the horizontal PAMs. The braid angle of the prototype PAMs is difficult to measure accurately, but the fact that this same trend is present in the experimental results indicates that the initial braid angle of the vertical PAM as fabricated is likely about a degree higher than the initial braid angle of the horizontal PAMs.

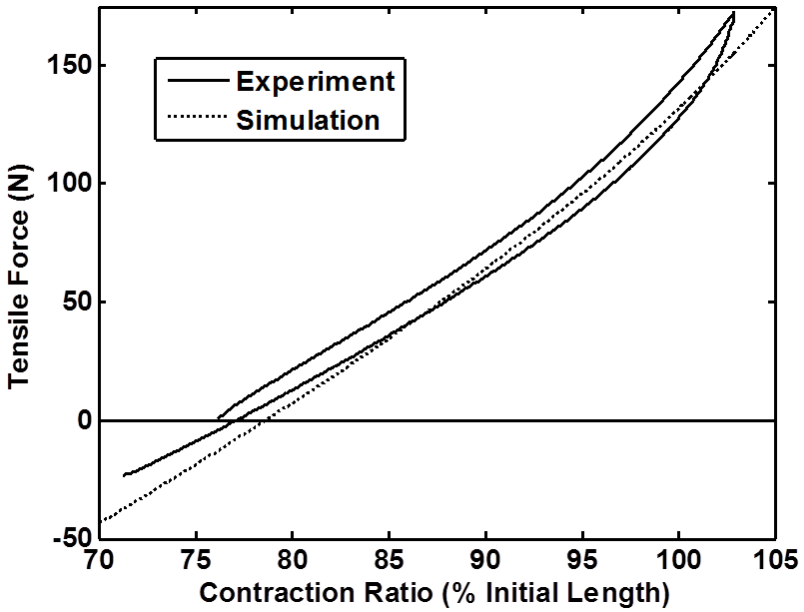

Figure 4. Tensile force versus contraction ratio for the vertical PAM at 682 kPa.

2.2 Hexagonal unit cell analysis and modulus calculation

The pin-jointed hexagonal unit cell used in this study is based on the cell presented in Pontecorvo et al.[1], a schematic of which is shown in Figure 7. The cell walls were rigid links and the pin-joints at the cell vertices highlighted the effects of the internal inclusions as these were not masked by the influence of cell wall bending. The basic unit cell is composed of inclined walls of length L_{link} that form an angle θ with the horizontal, vertical walls of length αL_{link}, and includes half the vertical wall, $\alpha L_{link}/2$, of the adjacent cells above and below the cell. The depth of the cell (into the page) is denoted as γL_{link}. Pontecorvo et al. showed that three spring elements connected between the vertices of the cell were necessary in order for the cell to be statically determinate and derived expressions for the modulus of the cell under both horizontal and vertical loading based on the stiffness of the three springs when arranged in the configuration shown in Figure 7. It was also demonstrated that the total modulus of the cell is given by the sum of the modulus due to the horizontal spring and the modulus due to the vertical spring.

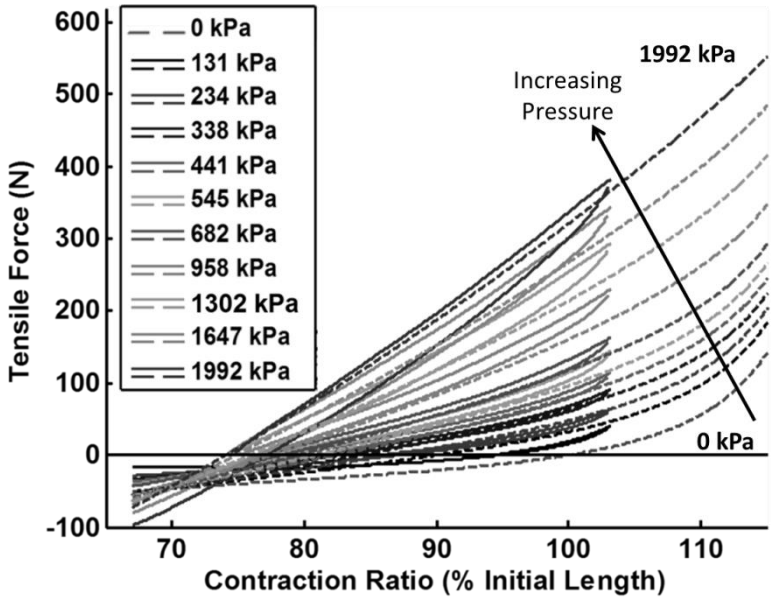

Figure 5. Averaged tensile force versus contraction ratio over a range of pressures for the horizontal PAMs. Dashed lines represent simulation, solid lines represent measured data.

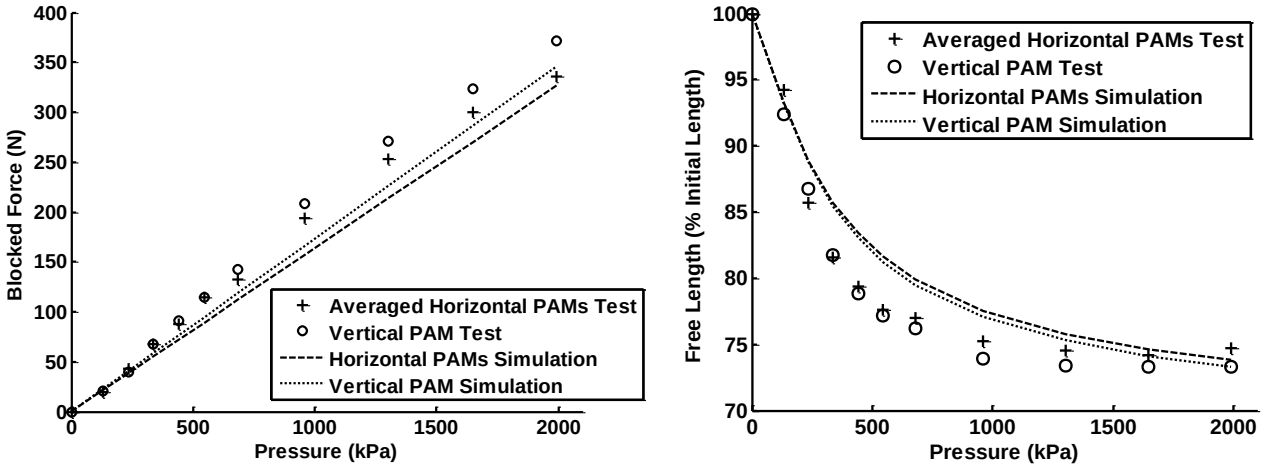

(a) (b)

Figure 6. Comparison of experimental and simulated (a) blocked force and (b) free length of the individual muscles.

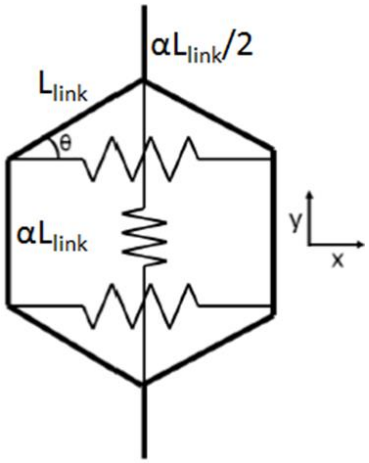

Figure 7. A pin-jointed hexagonal unit cell with three linear spring inclusions (two horizontal and one vertical) oriented in an "H" pattern between the vertices of the cell.[1]

The current study takes a similar approach to the calculation of the cell modulus, where the linear springs of the previous work are replaced by PAMs whose nonlinear behavior is represented by Equation 2. Since the PAMs carry load in tension, they are sufficiently pre-tensioned such that even as the cell is subjected to tensile and compressive loading, the individual PAMs only operate in tension.

To account for the introduction of the PAMs into the unit cell, consider the schematics of the unit cells loaded by an applied stress in the horizontal (x) direction depicted in Figure 8. The expressions for the stress applied in the horizontal direction, σ_x, and the strain in the horizontal direction, ε_x, are given by Equations 3 and 4, respectively. In Figure 8a where the two PAMs in the cell are oriented horizontally, $F_X = 2F_H$, and similarly for Figure 8b where the PAM in the cell is oriented vertically, $F_X = -F_V cot(\theta)$, where F_H and F_V are the tensile forces produced by the horizontal and vertical PAMs calculated using Equation 2. The forces in the PAMs are a function of applied pressure and muscle contraction ratio. F_H and F_V are functions of the active lengths of the horizontal and vertical muscles, which are related to the cell angle θ by Equations 5 and 6, respectively, where $L_{fitting}$ is the length from the cell vertex to the active portion of the PAM.

$$\sigma_X = \frac{F_X}{A_X} = \frac{F_X}{2L_{link}(sin(\theta)+\alpha)\gamma L_{link}} \tag{3}$$

$$\varepsilon_X = \frac{2L_{link}(\cos(\theta)-\cos(\theta_0))}{2L_{link}(\cos(\theta_0))} = \frac{(\cos(\theta)-\cos(\theta_0))}{(\cos(\theta_0))} \tag{4}$$

$$L_H = 2L_{link}cos(\theta) - 2L_{fitting} \tag{5}$$

$$L_V = 2L_{link}sin(\theta) + \alpha L_{link} - 2L_{fitting} \tag{6}$$

$$F_X = 2F_H(\mathrm{P}, CR_H) - F_V(\mathrm{P}, CR_V)\cot(\theta) \tag{7}$$

If all three PAMs are arranged in the cell together, the total applied force in the x-direction is related to the force in the vertical and horizontal PAMs as given in Equation 7. The $2F_H$ term in Equation 7 corresponds to the tensile force applied to the vertical cell walls by the horizontal PAMs which tends to pull the vertical walls together and increase the cell angle. This change in cell shape is resisted by the vertical PAM which applies a tensile force to the top and bottom cell vertices and acts to decrease the cell angle. The tensile force applied by the vertical PAM is transferred to the horizontal direction through the inclined cell walls and corresponds to the $-F_V cot(\theta)$ term in Equation 7.

The equilibrium angle of the cell (θ_0) occurs when the magnitudes of these two opposing terms are equal and can be calculated by setting F_X to zero in Equation 7. Figure 9 illustrates the balance between these two terms for different values of pressure in the horizontal and vertical PAMs from Figures 3 and 5 (ratio of cell vertical to inclined wall length, α, is assumed to be 1). The solid experiment and dotted

simulation curves in Figure 9 labeled "Vertical PAM" are derived from the curves presented in Figure 3 but have been converted to be functions of cell angle using Equation 6, and the force values have been multiplied by $cot(\theta)$. As indicated by the left *y*-axis label, these curves represent the force applied by the vertical muscle in the horizontal direction. Similarly, the solid experiment and dashed simulation curves in Figure 9 labeled "Averaged Horizontal PAMs" are derived from the curves presented in Figure 5, but have also been converted to be functions of cell angle using Equation 5, and the force values have been scaled by a factor of 2. This set of curves, as indicated by the right *y*-axis label, represents the force applied by the horizontal muscles in the horizontal direction. For clarity, hysteresis has been removed from all the experimental curves in Figure 9 by averaging the upper and lower branches of each hysteresis loop to form a single curve.

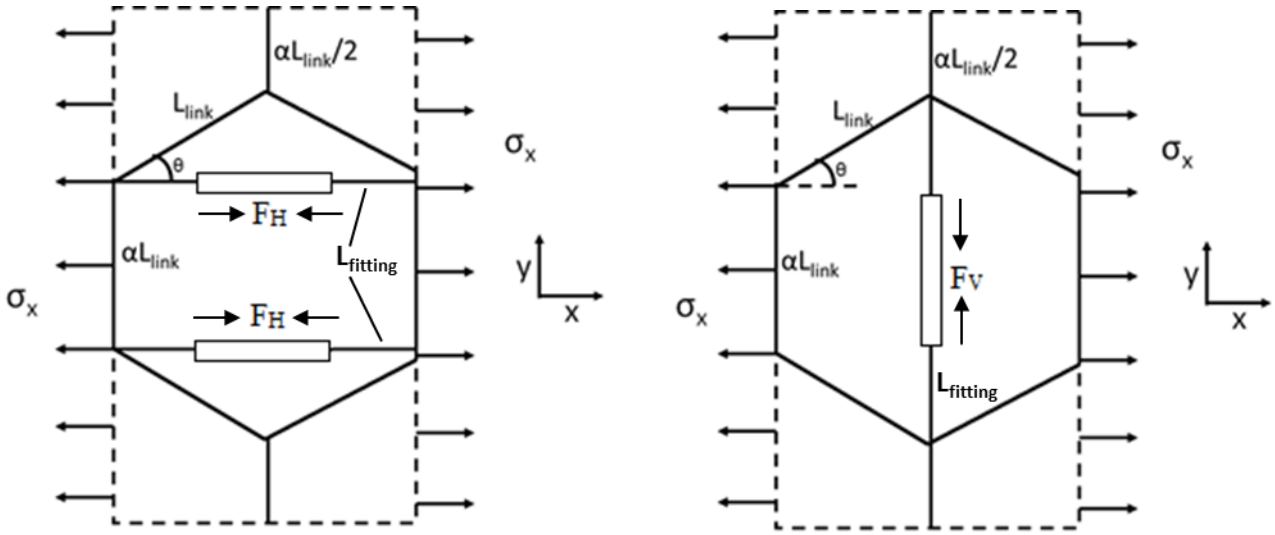

(a) (b)

Figure 8. Schematic of a pin-jointed hexagonal unit cell with (a) two horizontal PAMs and (b) a vertical PAM, with a stress applied to the cell in the horizontal direction[1].

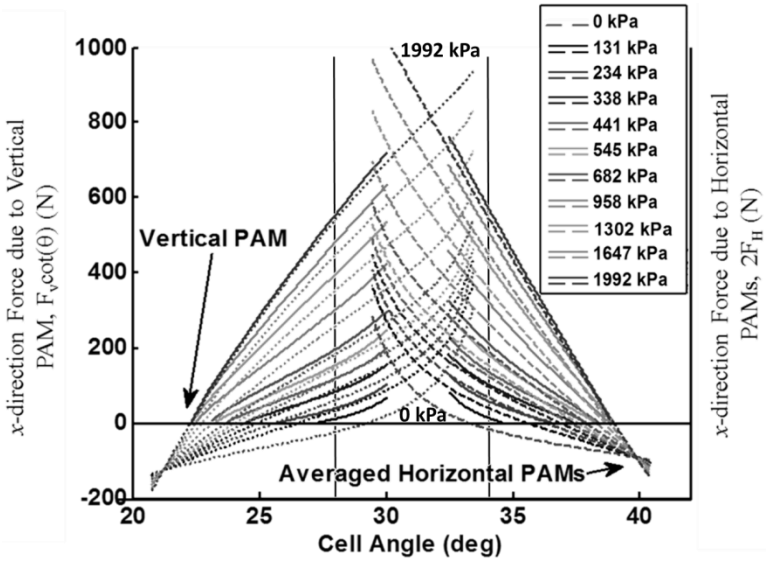

Figure 9. Tensile force versus cell angle in the horizontal direction for the vertical PAM and combined horizontal PAMs: solid curves are averaged experimental data and dashed curves are simulation.

The points in Figure 9 where the simulated curves for the vertical PAM cross those for the horizontal PAMs give the equilibrium angles for the cell (the experimental curves for individual PAMs outside the hexagonal cell were not measured to high enough contraction ratios to cross each other). From the figure it can be observed that when the vertical and horizontal PAMs are pressurized to the same level the change in cell angle is less than a degree with respect to the simulated zero-pressure equilibrium angle of 31.34°.

Even when the vertical and horizontal PAMs are pressurized to unequal pressure levels, the equilibrium cell angles remain between 28° and 34°. Consider as an example the case where the horizontal PAMs have zero pressure and the vertical PAM is pressurized to 682 kPa. The equilibrium cell angle is seen to be 29.6°. Here, the vertical PAM has contracted as a result of being pressurized from an initial contraction ratio of 106.3% to 101.4%, while the horizontal PAMs extend to a high contraction ratio of 114.1% where the tension in the muscle rises rapidly. This nonlinear stiffening in the PAM at high contraction ratios prevents significant changes in equilibrium cell angle from the zero-pressure state even when there is a large difference is pressure between the horizontal and vertical PAMs.

The slope of the force-displacement curve for the PAMs directly influences the modulus of the cell. In this study, cell modulus is calculated as a secant modulus, described by Equation 8, where the subscripts ΔF and $-\Delta F$ indicate a constant positive or negative increment in force applied to the cell about an equilibrium position (θ_0).

$$E_x = \frac{\sigma_{x\Delta F} - \sigma_{x-\Delta F}}{\varepsilon_{x\Delta F} - \varepsilon_{x-\Delta F}} = \frac{\dfrac{F_{x\Delta F}}{2\gamma {L_{link}}^2(sin(\theta_{\Delta F}) + \alpha)} - \dfrac{F_{x-\Delta F}}{2\gamma {L_{link}}^2(sin(\theta_{-\Delta F}) + \alpha)}}{\dfrac{(\cos(\theta_{\Delta F}) - \cos(\theta_0))}{(\cos(\theta_0))} - \dfrac{(\cos(\theta_{-\Delta F}) - \cos(\theta_0))}{(\cos(\theta_0))}} \tag{8}$$

Equation 8 can be simplified to illustrate that the cell modulus is dominated by the slope of the PAM force versus contraction ratio curve, and is influenced secondarily by the equilibrium cell angle. The first step in the simplification is expressed as Equation 9.

$$E_x = \frac{F_{x\Delta F}(sin(\theta_{-\Delta F}) + \alpha) - F_{x-\Delta F}(sin(\theta_{\Delta F}) + \alpha)}{(\cos(\theta_{\Delta F}) - \cos(\theta_{-\Delta F}))} \frac{\cos(\theta_0)}{2\gamma {L_{link}}^2(sin(\theta_{\Delta F}) + \alpha)(sin(\theta_{-\Delta F}) + \alpha)} \tag{9}$$

E_x can be further simplified by redefining $sin(\theta_{\Delta F})$ and $sin(\theta_{-\Delta F})$ in terms of a small increment in cell angle $\Delta\theta$ from the equilibrium position, and simplifying using the small angle assumption:

$$sin(\theta_{\Delta F}) = sin(\theta_0 - \Delta\theta) = sin(\theta_0) - \Delta\theta \cos(\theta_0) \tag{10}$$

$$sin(\theta_{-\Delta F}) = sin(\theta_0 + \Delta\theta) = sin(\theta_0) + \Delta\theta \cos(\theta_0) \tag{11}$$

Substitution of Equations 10 and 11 into Equation 9 yield

$$E_x = \frac{(F_{x\Delta F} - F_{x-\Delta F})(sin(\theta_0) + \alpha) + (F_{x\Delta F} + F_{x-\Delta F})\Delta\theta \cos(\theta_0)}{(\cos(\theta_{\Delta F}) - \cos(\theta_{-\Delta F}))} \frac{\cos(\theta_0)}{2\gamma {L_{link}}^2((sin(\theta_0) + \alpha)^2 - \Delta\theta^2 \cos^2(\theta_0))} \tag{12}$$

Recognizing that $(F_{x\Delta F} + F_{x-\Delta F}) = 0$ and that $\Delta\theta^2 \cos^2(\theta_0) \approx 0$,

$$E_x \approx \frac{(F_{x\Delta F} - F_{x-\Delta F})}{(\cos(\theta_{\Delta F}) - \cos(\theta_{-\Delta F}))} \frac{\cos(\theta_0)}{2\gamma {L_{link}}^2(sin(\theta_0) + \alpha)} \tag{13}$$

The corresponding trigonometric expressions using the small angle assumption for cosine are Equations 14 and 15.

$$cos(\theta_{\Delta F}) = cos(\theta_0 - \Delta\theta) = cos(\theta_0) + \Delta\theta \sin(\theta_0) \tag{14}$$

$$cos(\theta_{-\Delta F}) = cos(\theta_0 + \Delta\theta) = cos(\theta_0) - \Delta\theta \sin(\theta_0) \tag{15}$$

Substituting these expressions into the denominator in Equation 13, and defining $d\theta = 2\Delta\theta$, Equation 13 becomes

$$E_x \approx \frac{F_{x\Delta F} - F_{x-\Delta F}}{d\theta} \frac{\cot(\theta_0)}{2\gamma {L_{link}}^2 (sin(\theta_0) + \alpha)} \tag{16}$$

The numerator of the first term in Equation 16 is expanded by substitution of Equation 7.

$$F_{x\Delta F} - F_{x-\Delta F} = 2(F_{H\Delta F} - F_{H-\Delta F}) - \left(F_{V\Delta F} \cot(\theta_{\Delta F}) - F_{V-\Delta F} \cot(\theta_{-\Delta F})\right) \tag{17}$$

Again, Equations 10, 11, 14, and 15 are used to simplify Equation 17 and higher order terms are discarded.

$$E_x \approx \frac{2(F_{H\Delta F} - F_{H-\Delta F}) - (F_{V\Delta F} - F_{V-\Delta F}) \cot(\theta_0)}{d\theta} \frac{\cot(\theta_0)}{2\gamma {L_{link}}^2 (sin(\theta_0) + \alpha)} \tag{18}$$

The differences in the numerator of the first term are defined as $dF_H = F_{H\Delta F} - F_{H-\Delta F}$ and $dF_V = F_{V\Delta F} - F_{V-\Delta F}$. Differentiating Equations 5 and 6 and denoting the initial horizontal and vertical muscle lengths L_{H0} and L_{V0}, $d\theta$ can be expressed as:

$$d\theta = \frac{L_{H0} dCR_H}{2L_{link} cos(\theta)} = \frac{L_{V0} dCR_V}{2L_{link} cos(\theta)} \tag{19}$$

Equation 18 can thus be expressed in terms of the slope of the individual PAM force versus contraction ratios dF_H/dCR_H and dF_V/dCR_V.

$$E_x \approx \left[\frac{2}{L_{H0}} \frac{dF_H}{dCR_H} - \frac{\cot(\theta_0)}{L_{V0}} \frac{dF_V}{dCR_V}\right] \frac{cos(\theta) \cot(\theta_0)}{\gamma L_{link} (sin(\theta_0) + \alpha)} \tag{20}$$

From Figures 3 and 5 it is observed that the slopes dF_H/dCR_H and dF_V/dCR_V assume high values with increasing pressure or at very high PAM contraction ratios. Furthermore, the modulus is dependent on the interplay between the horizontal and vertical PAMs. The term outside the brackets in Equation 20 shows that the cell modulus also has a dependence on the cell geometry.

3. FABRICATION AND EXPERIMENTAL METHOD

The PAMs are fabricated by bonding 1/8" NPT steel barbed hose fittings inside both ends of a length of 6.35 mm outer diameter, 0.79 mm wall thickness latex tubing. A length of braided polyethylene terephthalate mesh sleeve, containing 120 0.19 mm diameter fibers, is then coated with epoxy at both ends and crimped over the latex tubing onto the end fittings using a 12.7 mm long, 9.34 mm inner diameter, 0.8 mm wall thickness piece of 3003 aluminum tubing.

The lengths of the muscles were designed such that for the same vertical and inclined wall lengths (α = 1) the cell would have an equilibrium angle close to 30°, while pulling the muscles into a slightly pre-tensioned state at zero pressure. This selection was made because hexagonal cellular structures with 30° cell angle and equal wall lengths are by far the most common. Measured values of the unpressurized active lengths of the muscles, L_0, are given in Table 1. When assembled in the cell under no load, the vertical muscle was at a measured contraction ratio of 106.3%, and the two horizontal muscles were at a contraction ratio of 107.6%, giving the unit cell a measured equilibrium angle of 31.34°.

The hexagonal cell itself is fabricated from dogbone-shaped aluminum links pinned together at their endpoints. Each link contains a ball bearing at both ends to decrease friction and further reduce contributions from sources other than the PAM stiffness to the modulus of the cell. Each wall of the hexagonal cell contains two links stacked in an order that allows the cell to be expanded to a multi-cell array if desired. The vertical walls of the cell also contain a third triangular-shaped link with a tab that can be gripped by an Instron machine for experimental testing, as seen in Figure 1. PAMs are connected between the vertices of the cell and supplied with air pressure by modified brass pressure fittings. The length from the pin to the active portion of each muscle ($L_{fitting}$) is listed in Table 2 along with the other cell parameters.

Table 2. Hexagonal unit cell parameters

L_{link} (m)	0.1111
$L_{fitting}$ Horizontal (m)	0.0676
$L_{fitting}$ Vertical (m)	0.0650
α	1
γ	0.4140

Figure 10 shows a photograph of the hexagonal cell with all three PAM inclusions fixed in an Instron model 4204 machine with a 5 kN load transducer. The cell is oriented such that the grips of the machine are holding the vertical walls of the cell to load it in the *x*-direction. Three sets of experiments were performed pressurizing only the two horizontal PAMs, only the vertical PAM, and pressurizing all three PAMs simultaneously. The PAMs were supplied industrial air from a 49L cylinder, pressurized to 17,237 kPa, and regulated by a Harris model 721 pressure regulator. Pressure was measured after the regulator but before the PAMs using an Omega PX4100-1KGV pressure transducer and a National Instruments USB-6212 data acquisition system. At each pressure, the Instron machine pulled the cell in tension to a load of 200 N at a rate of 10 N/s, then reversed direction and applied a compressive load to -100 N, and finally returned to the initial equilibrium position of the cell. The maximum pressure for the experiments with all three PAMs in the cell was limited to 682 kPa to avoid PAM failure, but this limit was likely overly cautious as the individual PAMs performed at 1992 kPa without failure. Thus, high pressure simulation of the hexagonal cell presented in the following sections is plausible.

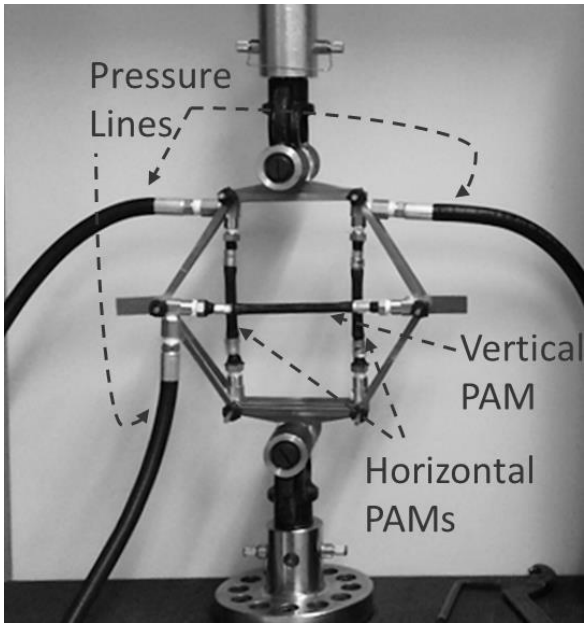

Figure 10. Hexagonal cell with three PAM inclusions fixed in the Instron machine for loading in the horizontal direction.

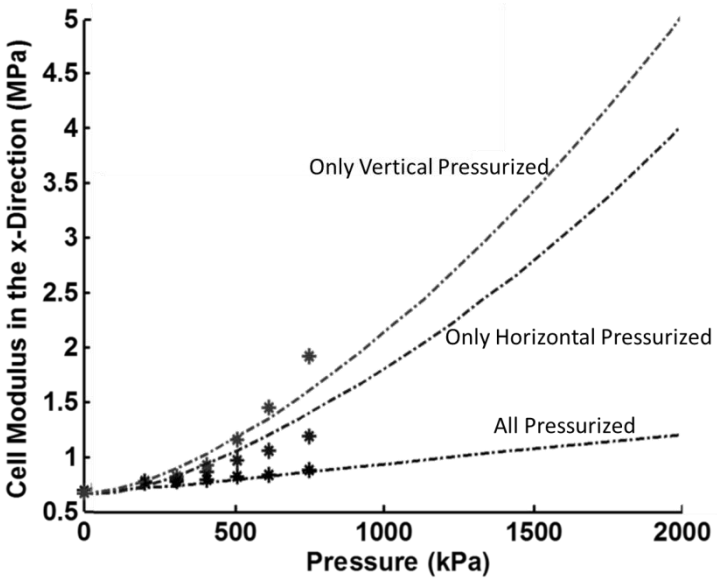

Figure 11. Cell modulus in the horizontal direction as a function of pressure.

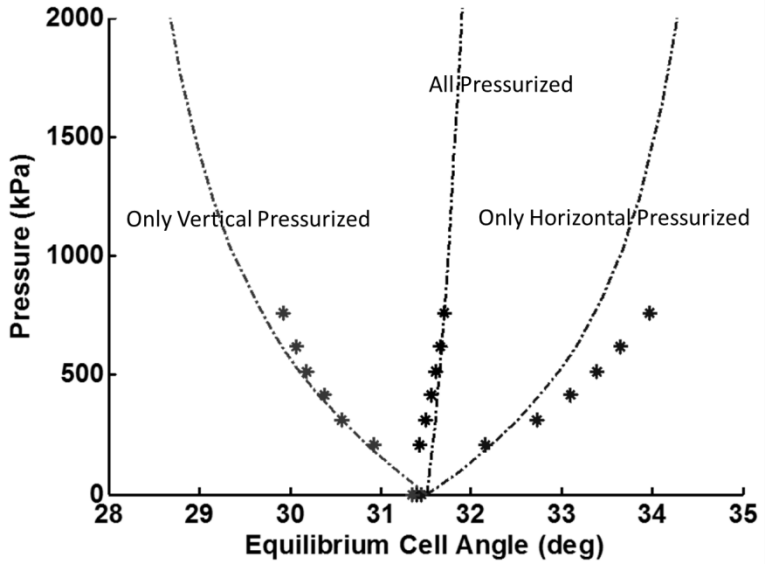

Figure 12. Equilibrium cell angle.

4. RESULTS

Figure 11 shows the variation in the hexagonal cell modulus in the horizontal (*x*) direction with increasing pressure, where the data points are the measured values from experiment and the dashed curves represent the simulation results. There is good agreement between the experiment and simulation when all three PAMs are pressurized together, but the simulation overpredicts modulus by a maximum of 15% at 682 kPa when only the horizontal PAMs are pressurized, and underpredicts modulus by 10% at 682 kPa when only the vertical PAMs are pressurized. As discussed in Section 2.2, the hexagonal cell's initial geometry balances the forces generated by the vertical and horizontal PAMs. Therefore, increasing the pressure in all three PAMs equally is not an effective approach to increasing the modulus of the cell. The data shows that even when all three PAMs are pressurized to 1992 kPa, the increase in modulus is only

80%. Instead, the PAMs must be pressurized differentially to realize larger changes in modulus. The greatest change in modulus is achieved by pressurizing only the vertical PAM. Experimentally, an increase in modulus from 0.65 MPa to 1.95 MPa (a 200% increase) was measured at 682 kPa, and simulation indicates that at 1992 kPa the modulus would increase to 4.98 MPa (a 666% increase). The corresponding change in cell angle is 1.53^{o} for the experimental measurement at 682 kPa, and 2.75^{o} for the simulation at 1992 kPa, as shown in Figure 12.

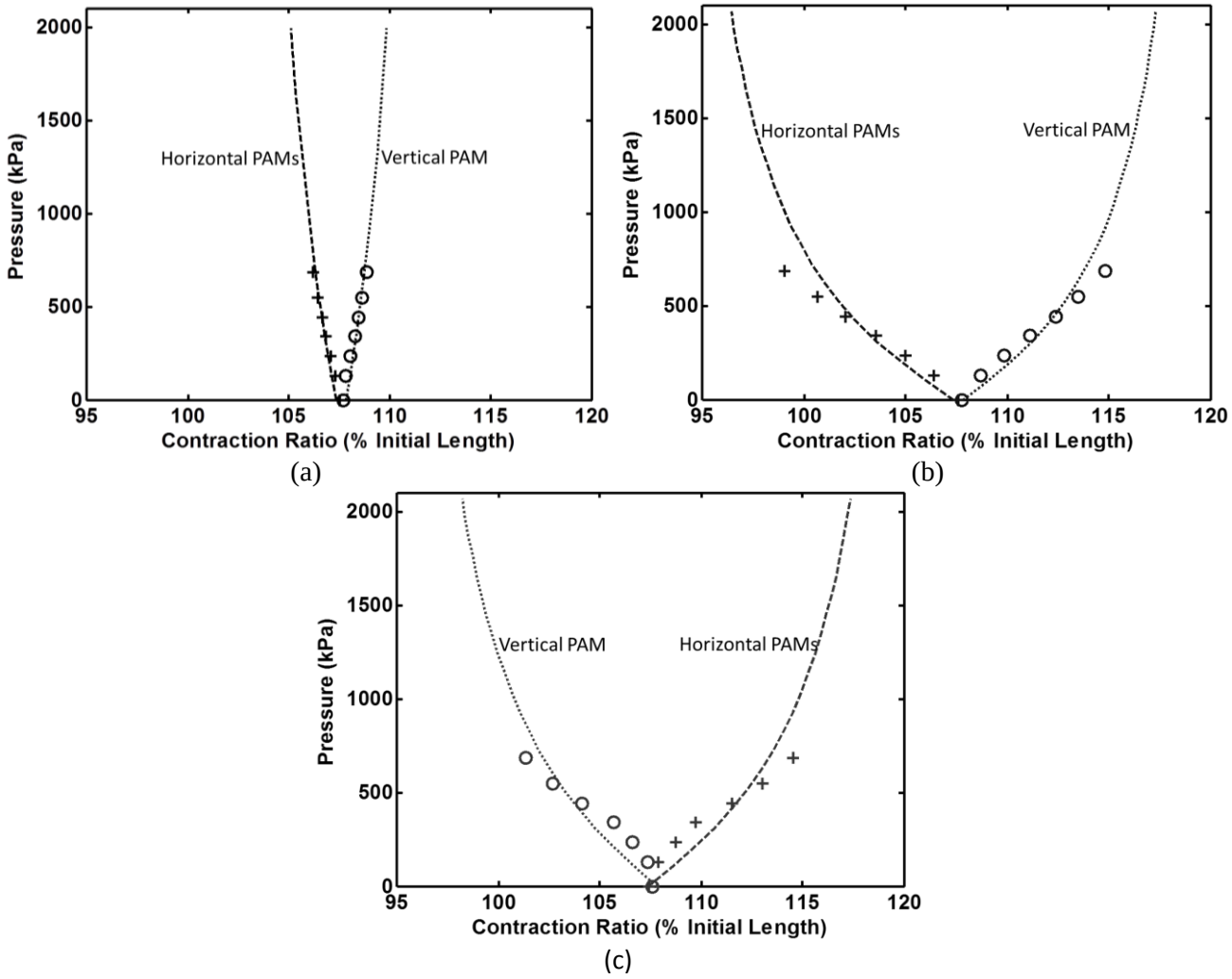

Figure 13. Equilibrium contraction ratio as a function of pressure when (a) all three PAMs are pressurized (b) only the horizontal PAMs are pressurized and (c) only the vertical PAM is pressurized.

Figure 13 shows a comparison of experimental measurements (symbols) and model predictions (dashed or dotted lines) for contraction ratios in the horizontal and vertical PAMs with increasing pressure. Recall from the discussion of Equation 20 that the modulus of the cell is determined by the slope of the individual PAM force versus contraction ratio curves. The highest slopes in Figure 3 and Figure 5 occur where the PAMs are unpressurized but at very high contraction ratios. Thus, the large increase in E_x seen in Figure 11 by pressurizing the vertical PAM is achieved because this stretches the horizontal PAMs to very high contraction ratios. This reasoning is confirmed by Figure 13c, which shows that the highest contraction ratios occur in the horizontal PAMs when the vertical PAM is pressurized. This maximum modulus configuration depends heavily on the relative values of the muscle parameters, especially the initial contraction ratio of the muscles.

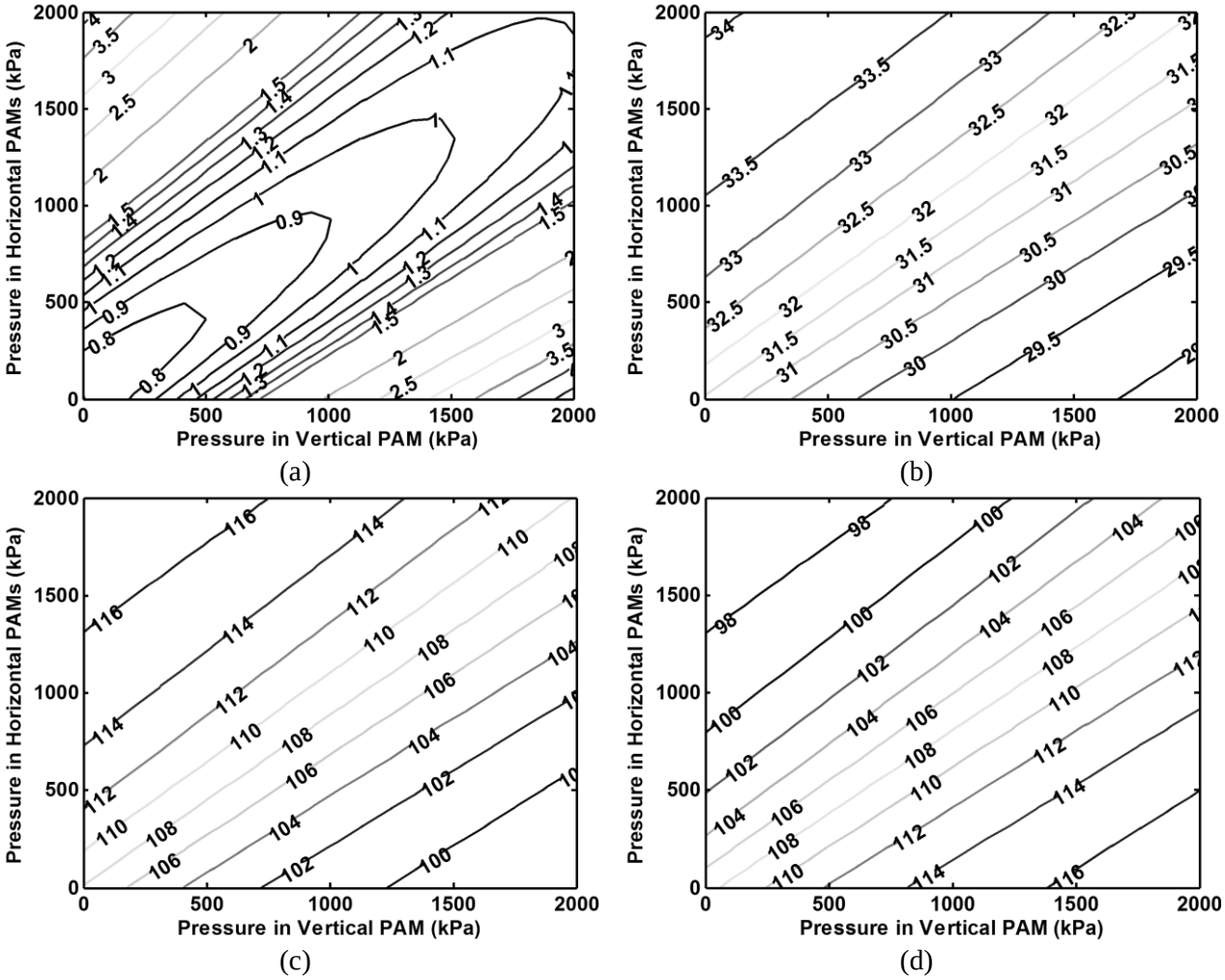

Figure 14. Simulated (a) Cell modulus in the horizontal direction in MPa (b) Equilibrium cell angle in degrees (c) Vertical PAM contraction ratio and (d) Horizontal PAM contraction ratio calculated over a range of differential pressures in the PAMs.

Another point of note is that the simulation in Figure 13a captures the trend that as pressure is increased equally in all three PAMs, the horizontal PAMs produce slightly more force than the vertical PAM, causing the contraction ratio of the horizontal PAMs to decrease, the contraction ratio of the vertical PAM to increase, and the overall cell angle to increase slightly (Figure 12). Although the trends are captured by the simulation, in all pressurization cases there seems to be a vertical offset of approximately 250 kPa in the experiment compared with simulation. This may represent that the physical PAMs required some initial pressure to begin contracting.

Consider Figure 14a, where the pressures in the vertical and horizontal PAMs vary independently from 0 to 1992 kPa and the values of the contours are the cell modulus E_x in MPa. In the simulation and experiments discussed above, only data points along each of the Figure 14a axes and the $y=x$ line were investigated. Figure 14a uses the simulation to fill in the operational space. As expected, the highest values of cell modulus fall far from the $y=x$ line in the upper left and lower right corners of the plot where either the horizontal or the vertical PAMs are completely unpressurized, while the other is fully pressurized. The corresponding cell angles and contraction ratios in the horizontal and vertical muscles are plotted in Figure 14b-d, respectively. In Figure 14b, pressurizing the vertical PAM is seen to decrease the cell angle while pressurizing the horizontal PAMs does the reverse. In Figures 14c and 14d, notice that the contraction ratios for a given muscle are never below 97% when the muscle is unpressurized, which means that the

muscles barely ever enter compression in the design space. In Figure 14c, moving along the *x*-axis, pressurizing the vertical PAM reduces its contraction ratio, but simultaneously pressurizing the horizontal PAM resists this contraction. In fact, high pressure in the horizontal PAMs with low-to-moderate pressure in the vertical PAM will force the vertical PAM to stretch. Similarly, in Figure 14d, moving up the *y*-axis, pressurizing the horizontal PAMs reduces their contraction ratios but simultaneously pressurizing the vertical PAMs resists this contraction. High pressure in the vertical PAMs with low-to-moderate pressure in the horizontal PAMs will force the horizontal PAMs to stretch. Figure 14a shows a maximum change in cell modulus (ΔE_x) of 666% when the vertical PAM is pressurized to 1992 kPa and the horizontal PAM is left unpressurized. The cell angle reduces to 28.59^o from a zero-pressure equilibrium cell angle of 31.34^o. The pressurized vertical PAM contraction ratio is 98.18% (down from a zero pressure contraction ratio of 106.3%) and the unpressured horizontal PAM contraction ratio increases to 117.4% (up from a pressure of 107.6% when no pressure was in the vertical PAMs).

5. DESIGN STUDY

In the previous section, the vertical and inclined walls of the cell had the same length (α=1), and the zero pressure equilibrium cell angle was held close to 30^o. This section examines whether greater changes in modulus may be realized by pressurizing the PAMs in different cell geometries. The vertical to inclined wall length ratio is varied between α=0.5 to 2, and the zero pressure equilibrium cell angle is varied from θ=10^o to 50^o. Further, for any given cell geometry, the PAM contraction ratios are varied as well. Four different values, a minimum of 100%, intermediate values of 104% and 107.6%, and a maximum value of 108.3% are used for the vertical PAM. In comparison, the previous section considered only single values of 106.3% and 107.6% for the vertical and horizontal PAM contraction ratios, respectively.

Figure 15 provides a flow chart of the process used to determine the maximum ΔE_x achievable. For a selected value of cell geometry parameters, α and θ, the four different values of vertical PAM contraction ratio are considered. For each value, the horizontal PAM contraction ratio required for the cell to maintain the selected zero pressure equilibrium angle, θ_o, is calculated. This step assumes that the PAMs have the same initial fiber angles, unpressurized wall thickness, unpressurized radius, and bladder modulus used for simulation of the prototype (Table 1), but the active length changes based on the cell geometry. For a vertical PAM contraction ratio of 100%, the horizontal PAMs are at 100% contraction ratio, as well. But for vertical PAM contraction ratios greater than 100%, the horizontal PAMs need to be pre-stretched as well to balance the forces exerted on the cell by the vertical PAM, and to hold the cell in equilibrium at the desired angle. Figure 16 shows the horizontal PAM contraction ratio versus equilibrium cell angle for increasing values of vertical PAM contraction ratio (marked on the curves). For vertical PAM contraction ratios greater than 100%, the horizontal PAM contraction ratios are equal for cell angles ranging from 30.59^o to 31.58^o. For higher cell angles (steeper cells), the horizontal PAM contraction ratios are lower, while for lower cell angles (shallower cells), the horizontal PAMs are stretched to higher contraction ratios. Note that the results in Figure 16 are independent of α because force produced by a given muscle (which determines equilibrium angle) is dependent only on the contraction ratio, not the physical length of the muscle.

For the current values of cell geometric parameters and PAM contraction ratios, the unstretched length of the vertical and horizontal PAMs is calculated assuming the prototype values of $L_{fitting}$ and L_{link}. Provided the calculated PAM lengths are greater than a minimum threshold value, the cell modulus in the *x*-direction is calculated for the zero pressure and three maximum pressurization cases as described in Section 4 and listed in the 6th step of Figure 15. For the maximum pressure cases a check was instituted to ensure that none of the PAMs within the cell were stretched beyond their physical limit. Equation 21, derived from Equation 1, describes the relationship between contraction ratio of the PAM and the bladder wall thickness.

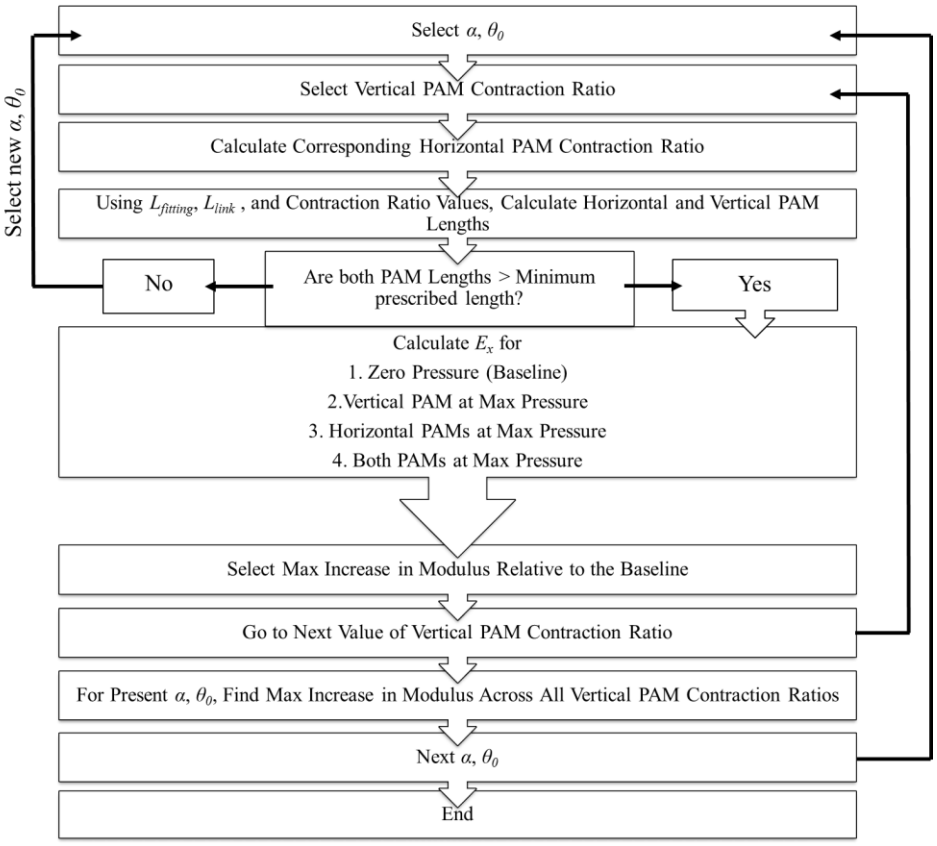

Figure 15. Flow chart of the process used to determine the maximum achievable *x*-direction change in cell modulus over a range of contraction ratios, cell angles, and wall length ratios.

$$t = R - \sqrt{R^2 - \frac{1}{CR}\left({R_0}^2 - (R_0 - t_0)^2\right)} \tag{21}$$

In order for *t* to be real, the quantity under the square root in Equation 21, which depends on contraction ratio, must be greater than zero. This limits the maximum contraction ratio of the vertical muscle to 118.05% and the maximum contraction ratio of the horizontal muscles to 119.68%. If in any of the pressurized equilibrium states of the cell the muscles exceed these limits, that case is eliminated from consideration.

For the feasible cases, the maximum change in cell modulus between the zero pressure state and one of the pressurized states is recorded, and the process is repeated for the next vertical muscle contraction ratio. After all contraction ratios are evaluated, the overall greatest change in cell modulus is determined for that point in the design space. The results of this design study are presented in Figure 17, where the labeled contours represent the maximum percent change in cell modulus relative to the zero pressure case. The gray shaded region in Figure 17 represents areas where maximum change in modulus is realized by pressurizing only the horizontal PAMs. Elsewhere, the maximum change is realized by pressuring only the vertical PAMs. The blacked out region at the extreme bottom left represents an infeasible area of the design space where the vertical PAM length is below a minimum threshold.

Figures 18a and 18b consider a couple of design points in greater detail. For α=1 and θ_0=20.5^o, (in the grey region in Figure 17), Figure 18a plots the cell modulus as a function of pressure. Clearly, the increase in modulus is greater when the horizontal PAMs are pressurized. In comparison, Figure 18b for α=1 and θ_0=41.5^o (in the unshaded region in Figure 17) shows the greatest increase in modulus is achieved by pressuring only the vertical PAM. Another point to note is that although the percent change in modulus for the case in Figure 18b is larger than that in Figure 18a, the magnitude of the maximum modulus in

Figure 18a is over 2.5 times larger than that in Figure 18b. Evidently, the low zero pressure modulus is a strong contributor to a high change in modulus in Figure 18b.

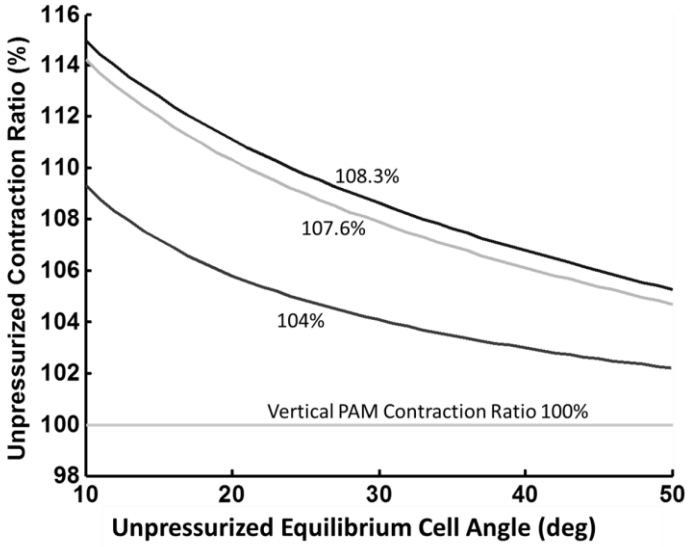

Figure 16. Unpressurized horizontal PAM contraction ratios corresponding to the labeled prescribed values of vertical PAM contraction ratio for a range of equilibrium cell angles.

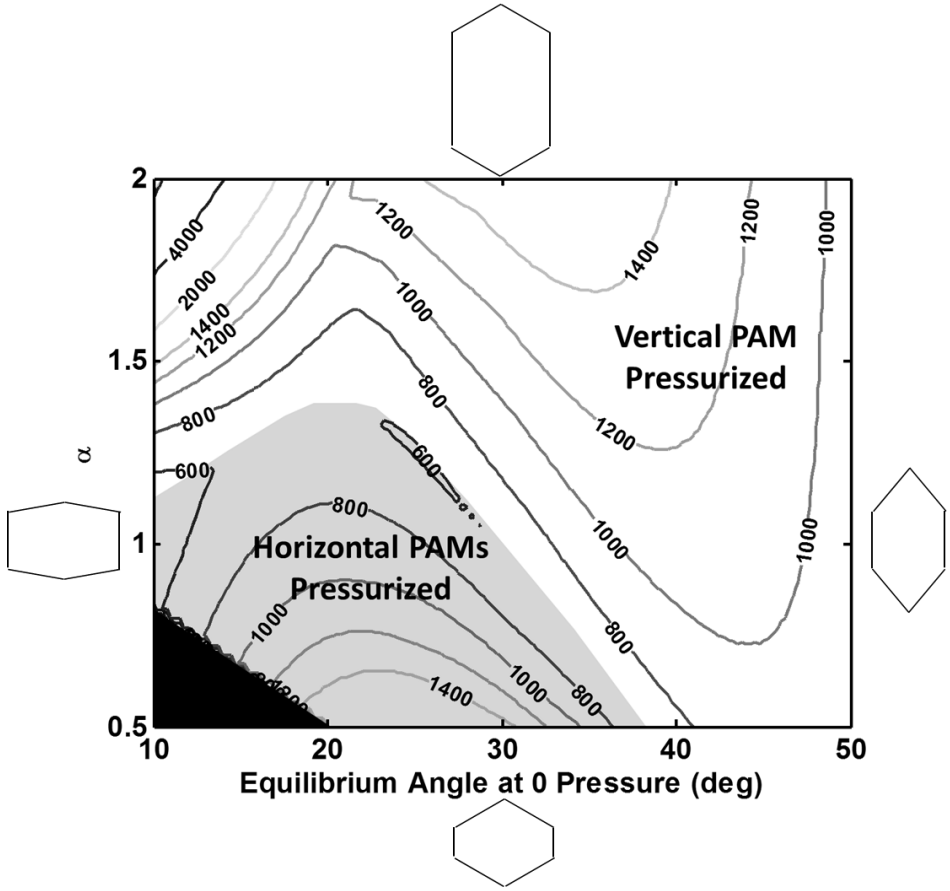

Figure 17. Maximum change in cell modulus (%) as a function of vertical wall length ratio (α) and equilibrium cell angle.

Figure 19a presents the zero pressure modulus with reference to which the maximum increase in modulus in Figure 17 is calculated, and Figure 19b shows the corresponding change in cell angle due to pressurization. These two plots, combined with Figure 17, serve as useful guides for selecting the best cell geometry in the design space that maximizes ΔE_x, while considering other constraints. There are three regions in Figure 17 where ΔE_x exceeds 1400%: the top left region, the top middle region, and the bottom left/middle region. Of those regions, Figure 19b shows that the top left of the plot has the highest changes in cell angle (exceeding 10^o), which is generally undesirable unless active shape change is a design goal. Therefore, the bottom left/middle region and the top middle region are more ideal for generating large changes in cell modulus for low changes in cell angle. Figure 19a shows that of these two regions, the top middle has a lower zero pressure cell modulus of less than 0.2 MPa and therefore also a lower pressurized cell modulus. Thus, the region that achieves the highest absolute cell modulus while also allowing for large ΔE_x and low changes in cell angle is the region below α=0.7 between zero pressure equilibrium cell angles of 20^o and 30^o. The maximum modulus in this region of 414 MPa is achieved at α=0.5 and θ_0=20^o, where the cross-sectional area of the cell in the *x*-direction is at the minimum possible value and the horizontal PAMs are fully pressurized to resist loading in the *x*-direction. In this region, however, the length of the vertical PAM is very short. A more reasonable design point with a feasible muscle length in the same region is α=0.7 and θ_0=25^o. The system parameters associated with this design point are listed in Table 3.

The reason for the distinct regions evident in Figure 19 is the discrete choices for starting vertical PAM contraction ratio used in the iterative loop of the design study. Figure 20a shows the initial contraction ratio of the vertical PAM corresponding to the results presented in Figures 17 and 19. Recall that within the loop, a check was made to eliminate any cell configurations where the pressurization of the PAMs caused the contraction ratio of the orthogonal PAMs to exceed the maximum limit. At high starting contraction ratios of the vertical PAM, all the PAMs within the cell were pre-strained before pressurization and therefore exceeded the contraction ratio limit when pressurized more easily. When this limit was exceeded, the pressurization case was eliminated from consideration. Therefore, the majority of maximum ΔE_x cases occurred at low starting vertical PAM contraction ratios (100% and 104%) because the higher starting contraction ratio cases (107.6% and 108.3%) had exceeded the limits of the muscles.

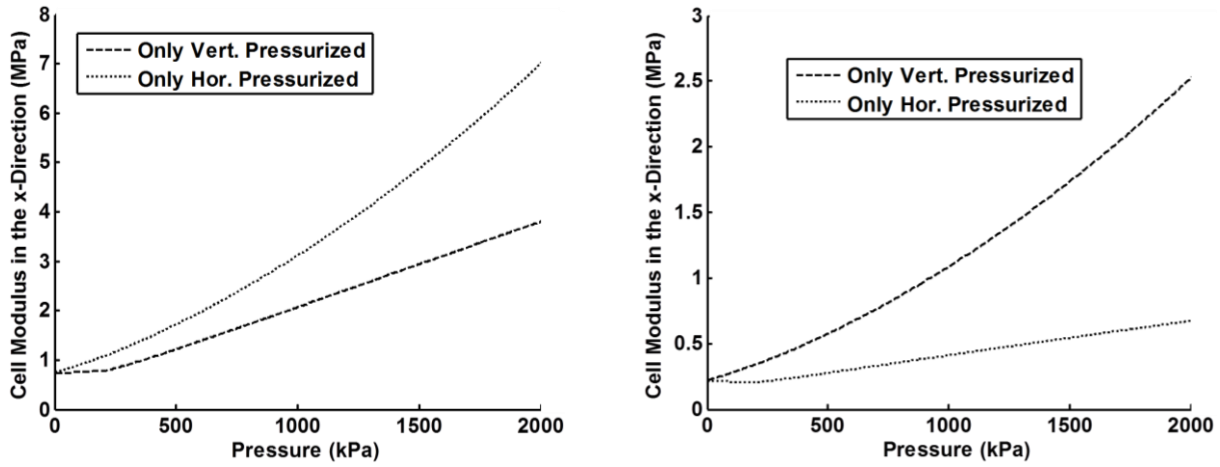

Figure 18. Cell modulus as a function of pressure for (a) α=1 and θ_0=20.5 and (b) α=1 and θ_0=41.5.

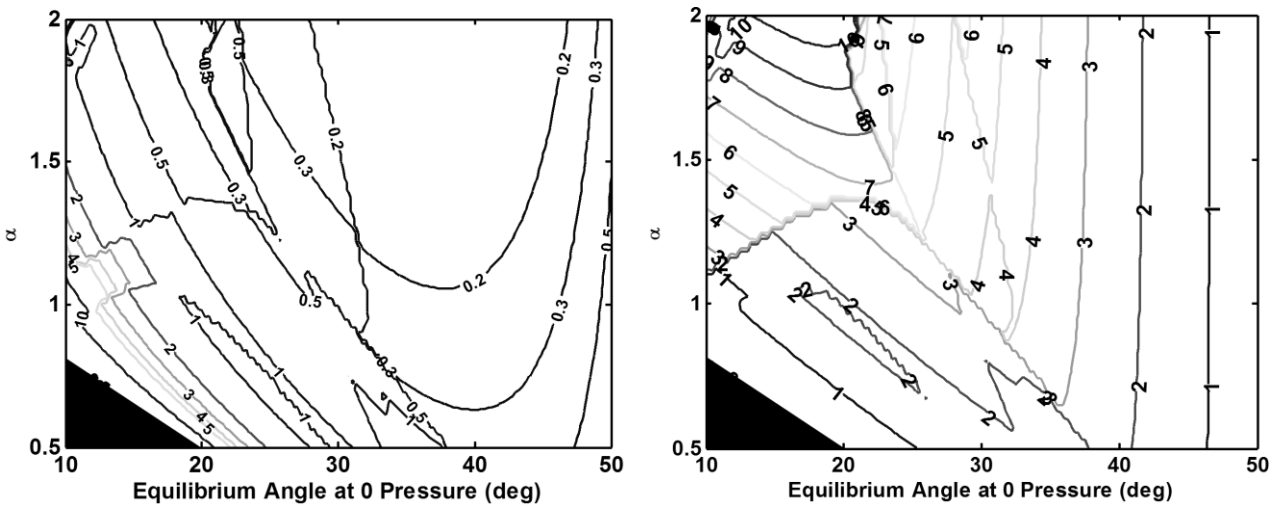

(a) (b)

Figure 19. (a) Zero pressure cell modulus corresponding to the maximum change in cell modulus (MPa) and (b) change in cell angle corresponding to maximum change in cell modulus (deg).

Table 3. System parameters at the design point where α=0.7 and θ_0=25°.

PAM Parameters	
L_H	66.2 mm
L_V	42.7 mm
Horizontal θ_{b0}	52.39°
Vertical θ_{b0}	53.58°
t_0	0.8 mm
R_0	4.8 mm
E	3 MPa
Cell Parameters	
L_{link}	111.1 mm
L_{Hfit}	67.6 mm
L_{Vfit}	64.5 mm
α	0.7
γ	0.4140
θ_0	25°
Resulting System Parameters	
Horizontal PAMs Eq. CR	100%
Vertical PAM Eq. CR	100%
Modulus, 0 kPa	0.81 MPa
Max. Modulus, 1992 kPa (Only Horizontal PAMs Pressurized)	11.00 MPa
Change in Cell Angle	1.96°
Max. Change in Modulus	1258%

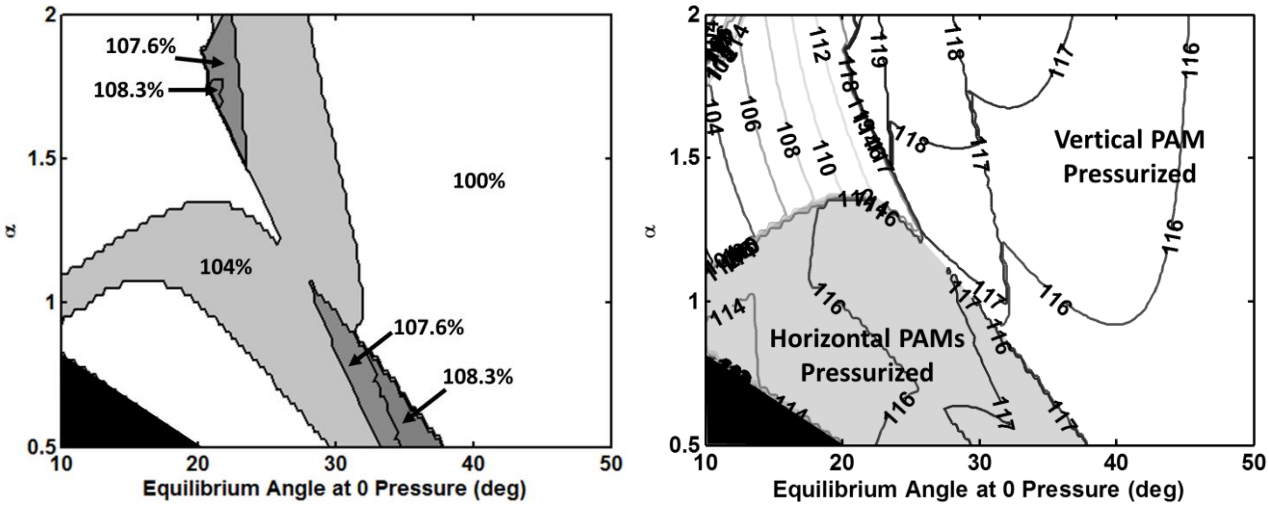

(a) (b)

Figure 20. (a) Unpressurized equilibrium contraction ratio of the vertical PAM corresponding to the maximum change in cell modulus and (b) maximum pressurized equilibrium contraction ratio (%) of any PAM within the cell.

Figure 20b plots the maximum contraction ratio of any PAM within the cell in the pressurized equilibrium state corresponding to the maximum ΔE_x. This figure shows that at the borders of the regions in Figure 20a, the contraction ratio of the PAMs have been pushed to the limit. At the borders of the gray region in Figure 20b, which corresponds to the region where the horizontal PAMs are pressurized to achieve a maximum ΔE_x, the maximum contraction ratio in the vertical PAM does not exceed the 118% limit. In the region where the vertical PAMs are fully pressurized, maximum ΔE_x is achieved by pre-straining the horizontal PAMs as much as possible. Again, at the borders where the zero-pressure vertical PAM contraction ratio changes in Figure 20a, the maximum horizontal PAM contraction ratio has been pushed nearly to its limit of 119.68%. If the parametric study for maximum ΔE_x were performed using smaller increments in vertical PAM contraction ratio values, every value in Figure 20b would be nearly equal to either the horizontal or the vertical PAM contraction ratio limit.

6. SUMMARY AND CONCLUSIONS

This work has presented a novel variable modulus cellular structure comprised of hexagonal unit cells with PAM inclusions. The cell considered is a pin-jointed hexagonal unit cell, loaded in the horizontal direction, with three PAMs oriented in an "H" pattern between the vertices of the cell: one vertical PAM and two horizontal PAMs. A model of the PAMs assuming a constant volume of bladder material was shown to compare well with force-displacement measurements of the individual PAMs used within the cell. A method for calculation of the hexagonal cell modulus based on an approach used for linear springs within the cell was introduced, as was an expression for the balance of tensile forces between the horizontal and vertical PAMs.

An aluminum hexagonal unit cell was fabricated and simulation of the hexagonal cell with PAM inclusions was then compared to experimental measurement of the unit cell modulus in the horizontal direction with the PAMs pressurized over a pressure range up to 682 kPa. An increase in cell modulus by a factor of 2 and a corresponding change in cell angle of only 1.53^o were demonstrated experimentally. A design study via simulation predicts that differential pressurization of the PAMs up to 1992 kPa can increase the cell modulus in the horizontal direction by a factor of 6.66 with a change in cell angle of only 2.75^o, and that by varying the cell geometry changes in modulus greater than 1000% are possible while

maintaining changes in cell angle below 3^o. The experiment and simulation show that this concept provides a way to largely decouple the length change of a PAM from the change in modulus to create a structural unit cell whose in-plane modulus in a given direction can be tuned based on the orientation of PAMs within the cell and the pressure supplied to the individual muscles.

ACKNOWLEDGMENTS

The authors acknowledge funding of these research activities by Dr. David Stargel through the Air Force Office of Scientific Research (grant numbers FA9550-11-1-0159 and 4767-RPI-AFOSR-0159).

REFERENCES

1. Pontecorvo, M.E., Barbarino, S., and Gandhi, F.S., "Cellular honeycomb-like structures with internal inclusions in the unit-cell," Proceedings of the ASME 2012 Conference on Smart Materials, Adaptive Structures and Intelligent Systems, Stone Mountain, Georgia, USA, September 19-21, (2012).
2. Barbarino, S., Pontecorvo, M.E., and Gandhi, F.S., "Cellular honeycomb-like structures with internal buckling and viscous elements for simultaneous load-bearing and dissipative capability," Proceedings of the ASME 2012 Conference on Smart Materials, Adaptive Structures and Intelligent Systems, Stone Mountain, Georgia, USA, September 19-21, (2012).
3. Bland, S.M., Snyder, R.J., Kudva, J.N., Barbarino, S., Pontecorvo, M.E., Gandhi, F.S., and White, E.V., "A novel structural element combining load carrying and energy dissipation capability", Proceedings of the AIAA SciTech 2014 Conference, National Harbor, Maryland, USA, January 13-17, (2014).
4. Gaylord, R., *Fluid actuated motor system and stroking device*, U.S. Patent No. 2,844,126, (1958).
5. Schulte, H., "The characteristics of the McKibben artificial muscle," The Application of External Power in Prosthetics and Orthotics, Publication 874, National Academy of Sciences - National Research Council, Washington DC, Appendix H, pp. 94-115, (1961).
6. Philen, M., "Fluidic flexible matric composite semi-active vibration isolation mounts," Journal of Intelligent Material Systems and Structures, 23, 353-363 (2012).
7. Philen, M., "Force tracking control of fluidic flexible matrix composite variable stiffness structures," Journal of Intelligent Material Systems and Structures, 22, 31-43 (2011).
8. Philen, M., "Tunable modulus structures utilizing fluidic flexible matrix composites: analytical and experimental investigations," 51st AIAA/ASME/ASCE/AHS/ASC Structures, Structural Dynamics, and Materials Conference, (2010).
9. Philen, M., "Sliding mode control of variable modulus structures based upon fluidic flexible matrix composites," 49th AIAA/ASME/ASCE/AHS/ASC Structures, Structural Dynamics, and Materials Conference, (2008).
10. Philen, M., "On the applicability of fluidic flexible matrix composite variable impedance materials for prosthetic and orthotic devices," Smart Materials and Structures, 18 (2009).
11. Chen, Y., Yin, W., Liu, Y. & Leng, J., "Structural design and analysis of morphing skin embedded with pneumatic muscle fibers," Smart Materials and Structures, 20 (2011).
12. Kim, G.-W., Li, S. & Wang, K., Ghasemi-Nejhad, M. N. (Ed.), "Variable stiffness actuator based on fluidic flexible matrix composites and piezoelectric-hydraulic pump," Active and Passive Smart Structures and Integrated Systems, 7643 (2010).
13. Kothera, C. S., Jangid, M., Sirohi, J. & Wereley, N. M., "Experimental characterization and static modeling of McKibben Actuators," *Journal of Mechanical Design,* (2009).

A Bi-Stable Mechanism for Blade Span Extension in Rotary-Wing Micro Aerial Vehicles

Matthew P. Misiorowski[1] Farhan Gandhi[2]

Rotorcraft, Adaptive and Morphing Structures (RAMS) Lab
Department of Mechanical, Aerospace and Nuclear Engineering
Rensselaer Polytechnic Institute, Troy, NY 12180

Michael Pontecorvo[3]

Advanced Concepts, Sikorsky Aircraft Corporation, 6900 Main St, Stratford, CT 06614

Previous studies have shown that rotary-wing micro air vehicles have limited range and endurance due to the high power loading associated with small rotors. A span morphing rotor could provide performance improvements associated with a larger rotor diameter while maintaining the small vehicle footprint in constrained environments. This paper presents a concept where increase in centrifugal force with increasing rotor RPM causes snap-through of a bi-stable mechanism within the blade, resulting in rotor span extension. The design and analysis of such a system is presented and initial rotor tests showed asynchronous extension of the two blades due to dissimilarity. A cable-pulley mechanism was designed and integrated into the prototype to ensure synchronous extension of the two blades. Using high-speed camera footage for measurement of rotor span extension and RPM, the prototype rotor was observed to snap-through at about 950 RPM, over about ¼ rotor revolution (0.015 sec). The snap-through RPM calculated from the high-speed camera was verified using data from a Hall Effect sensor on the rotor hub. Model simulation results of rotor extension versus RPM showed excellent correlation with measurement.

I. Introduction

Hover-capable Micro Aerial Vehicles (MAVs) potentially offer the soldier tremendously improved situational awareness in zones of conflict. However, they are limited by low endurance, range and payload capability. One approach to improving these attributes is through improving the rotor aerodynamic efficiency. The small rotors operating at low Reynolds numbers are known to have a significantly lower Figure of Merit compared to rotors on larger helicopters operating at much higher Reynolds numbers (Refs. 1–5). The rotary-wing MAVs being considered by the US Army for the applications discussed above have a rotor diameter nominally of around 6-9 inches. The small size allows the MAV to maneuver in confined spaces and to be easily stored in the soldier's pack. However, the MAV may not always face the most stringent space constraints during operation. A span-morphing rotor whose diameter can increase when flying in less confined spaces, will operate at a much reduced disk loading, which would in turn significantly improve Power Loading, Figure of Merit and endurance/range/payload capability. While span-extension morphing has been previously considered for large rotors (Refs. 6–9), rotary-wing MAVs have not yet exploited this concept. The key lies in the simple (low-weight, preferably passive) implementation of concept.

The present study focuses on centrifugally enabled micro-rotor span extension based on the use of a bi-stable mechanism. While centrifugally enabled span morphing has previously been considered for large rotors (Ref. 8), coupling with bi-stability has not been previously examined. Bi-stable structures are of interest for morphing applications because they allow a large morphing stroke and do not require a locking mechanism in either configuration since they correspond to stable equilibrium states (Ref. 10). Examples of bi-stable structures for aerospace morphing applications include the work by Weaver et al., (Ref. 11) and Schultz (Ref. 12) on fixed-wing applications, and by Gandhi et al. (Refs. 13-15) on helicopter rotor chord extension morphing. The study in Ref. 15 is particularly relevant as chord extension due to the snap-through of bi-stable elements is centrifugally enabled.

[1] Ph.D. Student, AIAA Student Member.
[2] Rosalind and John J. Redfern Jr. '33 Professor of Aerospace Engineering, AIAA Associate Fellow.
[3] Senior Engineer, Advanced Concepts, AIAA Member.

The following sections describe the design, analysis and fabrication of the mechanism of a variable-span micro-rotor in which increase in centrifugal force with increase in RPM produces snap-through of a bi-stable element and results in span extension. Designed for a two-bladed rotor, a system is developed to synchronize the deployment on both blades to prevent imbalance problems associated with one blade deploying first. The prototype is tested on a hover stand, span extension with increase in RPM is experimentally demonstrated, and analysis results are validated against test.

II. Concept and Analytical Model

The bi-stable mechanism on which rotor blade span extension in the present study is based is the von-Mises truss (VMT), a mechanical system first introduced in 1923 (Ref. 16) to model the stability of a shallow arch. As indicated in Fig. 1a, it consists of two pinned-pinned rigid members whose independent ends slide laterally against a spring restraint when a force is applied to the vertex to transition the VMT from one stable equilibrium condition to the other. Alternatively, variable length links may be used with the restraining springs contained within these links, as indicated in Fig. 1b. This arrangement is particularly useful if motion in the lateral direction is not permissible. Figure 2 (from Ref. 15) shows the implementation of a rotor chord extension morphing system using a VMT. The vertex of the VMT connects to a plate that can retract within the chord of the blade or extend to increase the effective chord length. Such a system, if rotated 90 deg, could be adapted to produce span extension.

To realize span extension in the present study, two changes are introduced to the conceptual design in Ref. 15 in addition to the 90 deg rotation. As indicated in the schematic sketch in Fig. 3, the bi-stable mechanism uses only one-half of the VMT shown in Figs. 1 and 2, or a single link of the truss. Additionally, a variable length link with an internal spring is used. One end is pivoted as indicated in the figure and the other end constrained so motion is purely along the spanwise direction, and the span extension mechanism operates between two parallel tracks.

In Fig. 3 when the bi-stable mechanism is in the first equilibrium state, the uncompressed link length is L_o, and its pinned end forms the angle θ_o. The free end of the link that slides in the spanwise direction is connected to an insert that is contained within the inner fixed section. As the centrifugal force on the insert increases, the link compresses, its free end begins to slide along the spanwise direction (displacement variable, x, is shown on Fig. 3). After going through the unstable equilibrium condition where the link has maximum compression, the link begins to expand again. If the force at the free end is removed, the bi-stable mechanism would settle in its second equilibrium state. In a micro-rotor the centrifugal force persists during operation, and a mechanical stop prevents further extension of the mechanism beyond the geometry corresponding to the second equilibrium state. The stiffness of the compression spring within the variable length link is denoted by k, and the mass of the insert attached to the free end of the link is m.

The equation of motion governing this bi-stable system is derived using Lagrange's equation, as described below.

$$\frac{\partial}{\partial t}\left(\frac{\partial \mathrm{L}}{\partial \dot{x}}\right) - \frac{\partial \mathrm{L}}{\partial x} = F \qquad [1]$$

$$L = T - V \qquad [2]$$

Kinetic energy of the system

$$T = \frac{1}{2} m \dot{x}^2 \qquad [3]$$

Potential energy of the system

$$V = \frac{1}{2} k (\Delta L)^2 = k \left[L_0 - \frac{L_0 cos(\theta_0)}{cos\left(tan^{-1}\left(\frac{L_0 sin(\theta_0) - x}{L_0 cos(\theta_0)} \right) \right)} \right]^2 \qquad [4]$$

$$\frac{\partial}{\partial t}\left(\frac{\partial \mathrm{L}}{\partial \dot{x}}\right) = m\ddot{x} \qquad [5]$$

$$\frac{\partial \mathrm{L}}{\partial x} = k\left(x - L_0 sin(\theta_0)\right) - \frac{k\left(x - L_0 sin(\theta_0)\right)}{cos(\theta_0)\sqrt{\frac{\left(x - L_0 sin(\theta_0)\right)^2}{\left(L_0 cos(\theta_0)\right)^2} + 1}} \qquad [6]$$

$$m\ddot{x} + k\left(x - L_0 sin(\theta_0)\right) - \frac{k\left(x - L_0 sin(\theta_0)\right)}{cos(\theta_0)\sqrt{\frac{\left(x - L_0 sin(\theta_0)\right)^2}{\left(L_0 cos(\theta_0)\right)^2} + 1}} = F \quad [7]$$

In Eq. 7, *F* represents the centrifugal force (CF), and its mathematical representation is provided in section III.

III. Prototype Design and Fabrication

A prototype is designed to demonstrate the bi-stable mechanism described in the previous section transitioning under centrifugal load and resulting in span extension. The present study is focused on the operation of the mechanism, and not the aerodynamic behavior of a variable span rotor. Consequently, a simplified system is designed and fabricated with all the functional components, but without aerodynamic profiles. Instead of designing a variable span rotor blade, per se, the bi-stable mechanisms are contained in an aluminum C-channel, and the inserts representing the extending portions of the blades slide within this channel.

Figure 4 shows one half of the channel on one side of the rotor hub, with the bi-stable mechanism and the attached insert in the compact as well as the extended span configurations. Based on the parameters shown in the figure (offsets δ_1 and δ_2, uncompressed link length, L_o, corresponding angle, θ_o, insert length of L_e, and an overlap length of βL_e in the extended configuration), the radius in the compact configuration can be expressed as:

$$R_c = \delta_1 + L_0 sin\theta_0 + \delta_2 + L_e = \delta_1 + 3L_0 sin\theta_0 + \delta_2 + \beta L_e \quad [8]$$

From the above, the increase in span can be shown to be mathematically equal to the "stroke length" of the bi-stable device.

$$\text{Span extension} = (1 - \beta)L_e = 2L_0 sin\theta_0 = \text{bi-stable mechanism stroke length} \quad [9]$$

And the radius in the extended configuration is:

$$R_e = R_c + (1 - \beta)L_e \quad [10]$$

Based on the capability of the in-house micro-rotor test facility, the value of R_c was selected to be 139 and the value of R_e was 197 mm (a 40% increase), with an overlap parameter of $\beta = 0.1$, in the extended configuration. From Eq. 9 it appears that the span extension can be maximized by increasing $L_0 sin\theta_0$. However, there are practical limits that constrain the maximum extension that can be achieved using a single bi-stable mechanism of the type shown in Figs. 3 and 4. Consider, for example, the case in Fig. 5a where a large stroke length is desired but the width of the channel is relatively small (corresponding to realistic blade aspect ratios). The minimum link length during transition is $L_0 cos\theta_0$ and the compression ratio of the internal spring would be greater than $L_0(1 - cos\theta_0)$. However, springs with significant stiffness generally have limits on maximum achievable compression ratios. Alternatively, Fig. 5b shows a schematic where the same stroke (as in Fig. 5a) is realized using a smaller link angle, θ_0, but a larger link length, L_0. While the required reduction in link length and internal spring compression are smaller, the channel width becomes too large with negative implications on blade aspect ratio (resulting in a very stubby blade). The link initial angle, θ_0, as well as the spring stiffness, *k*, also have a strong impact on the force required to transition the mechanism from the "retracted" to "extended" states. For a specific mass, *m*, of the insert, this determines the rotational speed at which the mechanism deploys.

Reasonable initial approximations are made on the mass of the insert, and deployment is targeted at just a little over 750 RPM (the switch-on RPM of the motor). This was done to avoid the excessive vibration and potential safety issues in the test associated with high RPM deployment. The analytical model in Section II is used to predict the span extension as a function of RPM, with the centrifugal force in Eq. 11 defined as:

$$CF = m \cdot (x_{cm} + x) \cdot \Omega^2 \quad [11]$$

Here x_{cm} is an offset along the insert where the center of mass is located.

An iterative procedure is used to select parameters such as channel width, the offsets, and spring stiffness, while considering constraints such as those discussed above as well as availability of commercial off-the-shelf components such as compression springs. The system parameters from the design process are listed in Table 1.

Table 1: Rotor dimensions and component characteristics used to describe contracted and extended radius as well as centrifugal force acting on inserts.

Extended Radius (R_e)	197 mm
Retracted Radius (R_r)	139 mm
Chord Length	45 mm
θ_0	40°
L_0	44.5 mm
δ_1	16 mm
δ_2	30 mm
L_e	64 mm
$\beta \cdot L_e$	6.4 mm
Spring Stiffness (k)	4.92 N/mm
Blade Mass	0.019 kg
Spanwise Location of CG (x_{cm})	78.7 mm

Based on the specified design, a micro-scale span morphing prototype, pictured in Fig. 6 was fabricated. The system uses a rigid aluminum C-channel, which spins about the central large-diameter bolt, with extendable Delrin inserts attached to variable length links. One end of each link is pinned to the C-channel, and the other is pinned to the Delrin insert. Housed within the variable length links are compression springs responsible for the bi-stability of the mechanism. Although this system cannot generate lift due to the absence of an aerodynamic outer profile, it is adequate to demonstrate span extension achieved through the transition of the bi-stable mechanism due to the centrifugal force acting on the Delrin inserts.

An important design feature of the prototype rotor is the slot that is cut in each of the Delrin inserts, which allows the insert to slide around a pin that is grounded to the c-channel. Contact between the end of the slot and the pin in the fully extended state provides a mechanical stop that prevents the insert from extending past the second stable equilibrium position of the bi-stable mechanism.

IV. Experimental Procedure

Centrifugally enabled span extension in conjunction with the bi-stable mechanism is demonstrated experimentally on the micro-rotor test facility at Rensselaer Polytechnic Institute's Rotorcraft, Adaptive and Morphing Structures (RAMS) Lab. The rotor test stand is powered by a Rimfire 1.20 450 kV electric motor that has been geared down by a ratio of 4:1 using a planetary gearbox (Fig. 7). The prototype is rigidly attached to the output shaft of the gearbox within which is embedded a permanent magnet. The RPM of the rotor is measured by a Hall Effect sensor which detects each rotation of the magnet, and is calculated using a NI USB-6212 data acquisition system. A Phantom V4.3 high speed camera is used to visually detect the occurrence of snap-through, verify the RPM measurements and measure the prototype extension. The high-speed camera software allows stepping through individual frames, and Fig. 8 shows how extension measurements are made by determining the position of the insert in successive frames. The high-speed camera is operated, nominally, at 1000 frames/sec. At a rotational speed of 1000 RPM, the camera would therefore record 60 images over one rotor revolution (at lower rotational speeds of around 900 RPM where snap-through occurs, the number of frames per revolution is even greater).

While the high-speed camera images are excellent for measurement of prototype extension, and the frames can be used to calculate rotor RPM, the Hall Effect sensor provides real-time RPM measurements as well as an indication of snap-through during the test. When snap-through occurs and the prototype very quickly extends, the rapid increase in rotor radius results in a significantly higher rotor rotational moment of inertia. The rotor is observed to momentarily lose speed (as indicated by the Hall Effect sensor and verified by the measurements of the high speed camera). However, the rotor stand is equipped with an RPM governor, and after the initial drop in RPM to conserve momentum, the governor restores RPM to the rate prior to snap-through.

In addition to the procedures described above with regards to the rotor stand experiments, the bi-stable mechanism was tested in an Instron model 4204 material testing machine with a 1 kN load transducer to verify the friction coefficients on the prototype.

V. Friction Measurements, First Rotor Test, and Model Refinement

The bi-stable mechanisms on each half of the channel were tested in the Instron machine under input displacement conditions. In the absence of any friction, the predicted force is symmetric about zero, as shown in Fig. 9. The predicted force is obtained by solving Eq. 7 quasi-statically for *F*, for a prescribed input, *x*. The measured curves for both the bi-stable mechanisms show a higher critical force required for transition to the second equilibrium position, effectively an upward offset of the force/displacement curve. This is attributed primarily to friction. It can be observed in Fig. 9 that the critical force (snap-through force) differs somewhat for the two mechanisms on either side of the channel.

Removing the internal spring from the variable length link, the friction coefficient is measured using an "incline test" (the inclination of the C-channel relative to horizontal is increased incrementally, and the angle at which the insert begins to slide is determined). This is done for both inserts, and the test is repeated several times for each insert and averaged. The experimentally measured friction coefficient values are determined to be 0.254 and 0.372 respectively. It should be noted that these measurements "bundle" friction between the Delrin insert and the Aluminum channel, as well as friction in the variable length link (which also involves Delrin sliding against Aluminum), and at the pin-joints.

The friction force is introduced into the quasi-static governing equation for the bi-stable mechanism, as shown.

$$k\left(x - L_0 sin(\theta_0)\right) - \frac{k\left(x - L_0 sin(\theta_0)\right)}{cos(\theta_0)\sqrt{\frac{\left(x - L_0 sin(\theta_0)\right)^2}{\left(L_0 cos(\theta_0)\right)^2} + 1}} = F - F_{FR} \quad [12]$$

$$\text{where } F_{FR} = \mu N \quad [13]$$

Using the experimentally derived values of friction coefficient, μ, the simulated force versus displacement curves are shown on Fig. 9. The normal force, N, in the simulation comes from the component in the force in the compression spring in the variable length link acting normal to the span, and is calculated as

$$N = k\Delta L \cos(\theta_0 - \theta) \quad [14]$$

A comparison of the simulated curves in Fig. 9 with the experimental data from the Instron test shows excellent correlation of the critical snap-through force, and of the overall behavior prior to the mechanism passing the unstable equilibrium position. Thereafter, the correlation is weaker with the measured force deviating from the simulation results. This is partly attributed to poorer alignment of the insert within the C-channel in the Instron test as the insert emerges from the channel and the overlap region decreases. A better correlation can be achieved using a non-constant friction coefficient model in the simulation, where the coefficient is increased beyond the unstable equilibrium state.

Based on the difference in snap-through force seen in Fig. 9 for the two mechanisms, it can be expected that in a rotor test one of the inserts will extend first and the other one will follow at an increased RPM when the increased centrifugal force is large enough for the second mechanism to snap-through. Introducing friction force on the right hand side of Eq. 7, the dynamic simulation indicates an expected difference of 42 RPM between deployments of the two inserts (Fig. 10). A first rotor test was conducted and using the high-speed camera this event of extension on one side occurring before the other was captured, as shown in still frame Fig. 11. The asynchronous extension results in a highly imbalanced rotor, and power to the motor was immediately cut in the test.

To eliminate the possibility of asynchronous extension, a cable system was designed and introduced into the prototype that ensured synchronous extension of both inserts. Figure 12 shows the prototype rotor with the synchronizing cable mechanism. As seen in the figure a small pulley is introduced coincident to the mechanical stop on each blade section. Cable 1-2-3 connects the inboard ends of the two inserts going around the pulley on the right

blade (at point 2), and cable 3-4-1 connects the inboard ends of the two inserts going around the pulley on the left blade (at point 4). If the section on the left blade starts to deploy first at a lower RPM, cable 1-2-3 (in red on Fig. 12b) is put in tension. This has the effect of holding back the insert on the left blade and preventing it from deploying, while simultaneously pulling forward on the insert on the right blade and assisting its deployment. During this process the cable 3-4-1 goes slack and plays no role, but if the section on the right was to deploy first the roles of the two cables would be reversed.

Denoting x_1 as the direction the leading blade travels and x_2 as the direction of motion for the lagging blade, the simulation model solves the governing equation simultaneously for each blade. If T_c is the cable tension, then the equation for the lagging blade is

$$m\ddot{x}_2 + k\big(x_2 - L_0 sin(\theta_0)\big) - \frac{k\big(x_2 - L_0 sin(\theta_0)\big)}{cos(\theta_0)\sqrt{\frac{\big(x_2 - L_0 sin(\theta_0)\big)^2}{\big(L_0 cos(\theta_0)\big)^2} + 1}} = F_{CF}(x_2) - F_{FR} + T_c \cos\theta_d \quad [15]$$

and that for the leading blade is

$$m\ddot{x}_1 + k\big(x_1 - L_0 sin(\theta_0)\big) - \frac{k\big(x_1 - L_0 sin(\theta_0)\big)}{cos(\theta_0)\sqrt{\frac{\big(x_1 - L_0 sin(\theta_0)\big)^2}{\big(L_0 cos(\theta_0)\big)^2} + 1}} = F_{CF}(x_1) - F_{FR} - T_c \cos\theta_r \quad [16]$$

The angles θ_d and θ_r are shown on Fig. 12b. The appropriate values of friction coefficient are used for the two blades, and the normal force is adjusted to include the effect of cable tension in addition to the force exerted by the compression spring in the link. For the lagging blade,

$$F_{FR} = \mu(x_2)[k\Delta L_2 cos(\theta_0 - \theta_2) - T_c \sin(\theta_d)] \quad [17]$$

and for the leading blade,

$$F_{FR} = \mu(x_1)[k\Delta L_1 cos(\theta_0 - \theta_1) - T_c \sin(\theta_r)] \quad [18]$$

The instantaneous compression in the spring is calculated as

$$\Delta L_{1,2} = L_0 - \frac{L_0 cos\theta_0}{cos\Big(\text{atan}\Big(\frac{L_0 sin\theta_0 - x_{1,2}}{L_0 cos\theta_0}\Big)\Big)} \quad [19]$$

Where the instantaneous link angle is

$$\theta_{1,2} = \theta_0 - \text{acos}\left(\frac{L_0 cos\theta_0}{L_0 - \Delta L_{1,2}}\right) \quad [20]$$

If k_c is the axial stiffness of the cable, and ΔL_c is the extension in the cable, the cable tension is calculated as

$$T_c = k_c \cdot \Delta L_c(x_1, x_2) \quad [21]$$

The extension in the cable is calculated using

$$\Delta L_c = L_c(x_1, x_2) - L_{c0} \quad [22]$$

where the cable initial length, L_{c0}, and instantaneous length, $L_c(x_1, x_2)$, during deformation, are calculated using Fig. 13, as

$$L_{c0} = \sqrt{\big(\delta_p - \delta_1\big)^2 + h_p^2 - r_p^2} + r_p\left(\frac{\theta_w}{2\pi}\right) + \sqrt{\big(\delta_p + \delta_1\big)^2 + \big(L_0 cos\theta_0 - h_p\big)^2 - r_p^2} \quad [23]$$

$$\theta_w(x_1,x_2) = 2\pi - \left[\cos^{-1}\left(\frac{r_p}{\sqrt{\left(\delta_p-\delta_1\right)^2+h_p^2}}\right) + \cos^{-1}\left(\frac{r_p}{\sqrt{\left(\delta_p+\delta_1\right)^2+\left(L_0cos\theta_0-h_p\right)^2}}\right) + \cos^{-1}\left(\frac{\left(\delta_p+\delta_1\right)\left(\delta_p-\delta_1\right)+\left(L_0cos\theta_0-h_p\right)h_p}{\sqrt{\left(\delta_p+\delta_1\right)^2+\left(L_0cos\theta_0-h_p\right)^2}\cdot\sqrt{\left(\delta_p-\delta_1\right)^2+h_p^2}}\right)\right] \quad [24]$$

$$L_c(x_1,x_2) = \sqrt{\left(\delta_p-\delta_1-x_2\right)^2+h_p^2-r_p^2} + r_p\theta_w(x_1,x_2) + \sqrt{\left(\delta_p+\delta_1+x_1\right)^2+\left(L_0cos\theta_0-h_p\right)^2-r_p^2} \quad [25]$$

$$\theta_w(x_1,x_2) = 2\pi - \left[\cos^{-1}\left(\frac{r_p}{\sqrt{\left(\delta_p-\delta_1-x_2\right)^2+h_p^2}}\right) + \cos^{-1}\left(\frac{r_p}{\sqrt{\left(\delta_p+\delta_1+x_1\right)^2+\left(L_0cos\theta_0-h_p\right)^2}}\right) + \cos^{-1}\left(\frac{\left(\delta_p+\delta_1+x_1\right)\left(\delta_p-\delta_1-x_2\right)+\left(L_0cos\theta_0-h_p\right)h_p}{\sqrt{\left(\delta_p+\delta_1+x_1\right)^2+\left(L_0cos\theta_0-h_p\right)^2}\cdot\sqrt{\left(\delta_p-\delta_1-x_2\right)^2+h_p^2}}\right)\right] \quad [26]$$

Using the simulation model described above and solving for extension of both blades simultaneously, the blades were observed to deploy synchronously, as seen in Fig. 14. Figure 15 shows the strain in the two cables as a function of extension. While one of the cables goes slack (negative $\Delta L_c/L_{c0}$, the other is in tension and produces the synchronized extension of the two blades seen in Fig. 14). The maximum tensile strain in the cable for the current configuration is seen to be 6E-4.

VI. Synchronous Extension Test

With the prototype refitted with the cable and pulley mechanisms to ensure synchronous extension another rotor test was carried out. The motor turn on RPM was 750 RPM, and the rotational speed was ramped up at 450 RPM/sec. With a predicted snap-through RPM of around 950, this ensured that the snap-through event and the extension of the rotor would be captured by the high-speed camera recording for 1 second. Using the frames from the high-speed camera, both the extension of the blade as well as the rotor RPM could be calculated. Figure 16 shows the experimentally measured extension versus RPM data, from several tests. Also included on the figure are simulation results for synchronous extension corresponding to a 450 RPM/sec ramp. The simulation results are seen to correlate very well with the high-speed camera data, with snap-through and extension occurring at around 950 RPM.

Figure 17 shows frames from the high-speed camera, and snap-through can be seen to be occurring over about quarter revolution (or 0.015 sec at 950 RPM). Importantly, both blades are seen to be extending in a synchronous manner. Figure 18 shows RPM readings from the Hall Effect sensor. When snap-through occurs, the increase in rotor inertia leads to an instantaneous reduction in rotor RPM. However, the RPM governor compensates and the RPM is quickly restored. The instantaneous reduction in RPM, as captured by the Hall effect sensor between 920 and 950 RPM (in 4 separate runs), corroborates the data obtained from the high-speed camera (presented in Fig. 17). Although not presented, it should be noted that the high-speed camera too recorded an instantaneous dip in RPM, followed by a quick recovery, when snap-through occurred.

VII. Summary and Concluding Remarks

This paper presents the concept of a span morphing blade for rotary-wing micro-aerial vehicle applications. The blades use a bi-stable mechanism that snaps-through when the RPM and centrifugal force increase beyond a critical value. The snap-through of the bi-stable mechanism results in rotor span extension when inserts connected to it and contained within the blade are deployed. The design and analysis of such a mechanism was presented in detail, and

a prototype was fabricated capable of span increase from 139 mm to 197 mm. Due to dissimilarity in friction between the two blades, one of the blades was predicted to extended earlier (about 40 RPM lower) than the other, and rotor test results verified this asynchronous extension.

To avoid imbalance problems associated with asynchronous extension of the two blades, a cable-pulley mechanism was designed and introduced into the prototype, and the simulation model was updated to account for it. The analytical model predicted that the cable-pulley mechanism would ensure synchronous extension of the two blades, with maximum tensile strains in the cable of 6E-4.

A second rotor test was conducted with the cable-pulley mechanism installed, and blade extension measurements were obtained using high-speed camera footage. RPM measurements were obtained from both high-speed camera data as well as from a Hall Effect sensor on the rotor shaft. Rotor test results showed synchronous extension of the two blades at around 950 RPM. From the high-speed camera data it was observed that snap-through occurred over about a ¼ revolution, or about 0.015 sec. The simulation results of rotor extension versus RPM compared well with test data. An instantaneous drop in RPM due to increase in rotor inertia was noted when snap-through occurred, but the RPM governor quickly restored the rotor speed.

A second generation prototype with aerodynamic surfaces and an improved mechanism design (Fig. 19) is currently under fabrication, with plans for testing on the rotor stand.

Acknowledgements

The authors gratefully acknowledge funding of these research activities by the Air Force Office of Scientific Research (grant number FA9550-11-1-0159) with Dr. David Stargel as the program manager. The authors would also like to thank Prof. Yoav Peles in the Mechanical Engineering program at RPI for the use of the high-speed camera during the rotor tests.

References

1. Bohorquez, F., Samuel, P., Sirohi, J., Pines, D., Rudd, L., and Perel, R., "Design Analysis and Hover Performance of a Rotating Wing Micro Air Vehicle," *Journal of American Helicopter Society*, Vol. 48, (2), April 2003, pp. 80–90.
2. Pines, D. J., and Bohorquez, F., "Challenges Facing Future Micro-Air-Vehicle Development," *Journal of Aircraft*, Vol. 43, (2), March–April 2006, pp. 290–305.
3. Chopra, I., "Hovering Micro Air Vehicles: Challenges and Opportunities," Proceedings of the International Forum on Rotorcraft Multidisciplinary Technologies, Oct. 15-17, 2007, Seoul, Korea.
4. Hein, B. R., and Chopra, I., "Hover Performance of a Micro Air Vehicle: Rotors at Low Reynolds Number," *Journal of American Helicopter Society*, Vol. 52, (3), July 2007, pp. 254-262.
5. Ramasamy, M., Johnson, B., Leishman, J. G., "Understanding the Aerodynamic Efficiency of a Hovering Micro-Rotor," *J. of American Helicopter Society*, Vol. 53, (4), Oct. 2008, pp. 412–428.
6. Fradenburgh, E. A., "Application of a Variable Diameter Rotor System to Advanced VTOL Aircraft," *31st American Helicopter Society Forum*, Washington, D.C., May 13-15, 1975.
7. Fradenburgh, E. A., and Matuska, D. G., "Advancing Tiltrotor State-of-the-art with Variable Diameter Rotors," *48th American Helicopter Society Forum*, Washington D.C., June 3-5, 1992.
8. Prabhakar, F. Gandhi, J. Steiner and D. McLaughlin, "A Centrifugal Force Actuated Variable Span Morphing Helicopter Rotor," *63rd Annual AHS International Forum and Technology Display*, Virginia Beach, VA, May 1-3, 2007.
9. Mistry, M., and Gandhi, F., "Helicopter Performance Improvement with Variable Rotor Radius and RPM," *Journal of the American Helicopter Society*, **59**, 042010 (2014).
10. Pontecorvo, M., Barbarino, S., Murray, G., and Gandhi, F., "Bi-Stable Arches for Morphing Applications" *J. of Intelligent Material Systems and Structures*, Vol. 24, No. 3, Feb 2013, DOI: 10.1177/1045389X12457252.
11. Diaconu, C. G., Weaver, P. M., and Mattonni, F., "Solutions for Morphing Airfoil Sections Using Bistable Laminated Compositie Structures," AIAA Structural Dynamics and Materials Conference, 23–26 April 2007, Honolulu, Hawaii.
12. M. Schultz, "A Concept for Airfoil-like Active Bistable Twisting Structures," *Journal of Intelliget Material Systems and Structures*, 2008.

13. Johnson, T., Frecker, M., and Gandhi, F., "A Bistable Mechanisms for Chord Extension Morphing Rotors," *Proc. of the 2009 SPIE Conf. on Smart Structures and Materials*, San Diego, California, March 8-12, 2009.
14. Johnson, T., Gandhi, F., and Frecker, M.,"Modeling and Experimental Validation of a Bistable Mechanism for Chord Extension Morphing Rotors," *Proc. of the 2010 SPIE Conf. on Smart Structures and Materials*, San Diego, California, March 7-11, 2010.
15. Moser, P., Barbarino, S., and Gandhi, F., "Helicopter Rotor Blade Chord Extension Morphing using a Centrifugally Actuated von-Mises Truss," *Journal of Aircraft*, Vol. 51, No. 5 (2014), pp. 1422-1431. doi: 10.2514/1.C032299.
16. Von Mises, R., "Über die Stabilitätsprobleme der Elastizitätstheorie," *Zeitschrift für Angewandte Mathematik und Mechanik*, Vol. 3, No. 6, 1923, pp. 406-422.

Figures

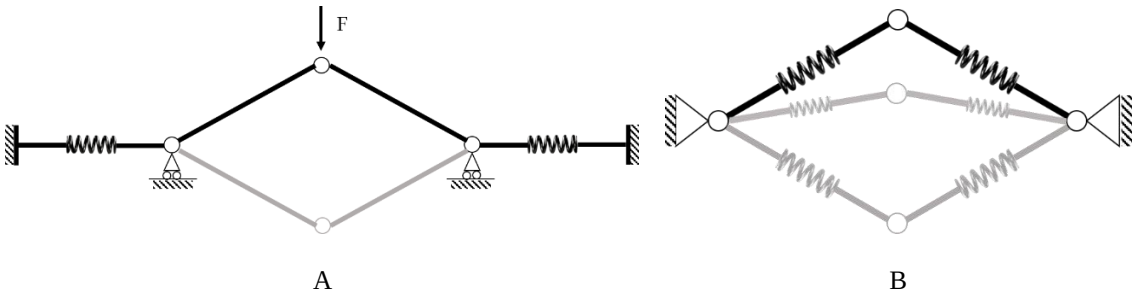

Fig. 1: Von Mises Truss with (A) rigid links, and (B) variable length links showing the first and second stable equilibrium positions.

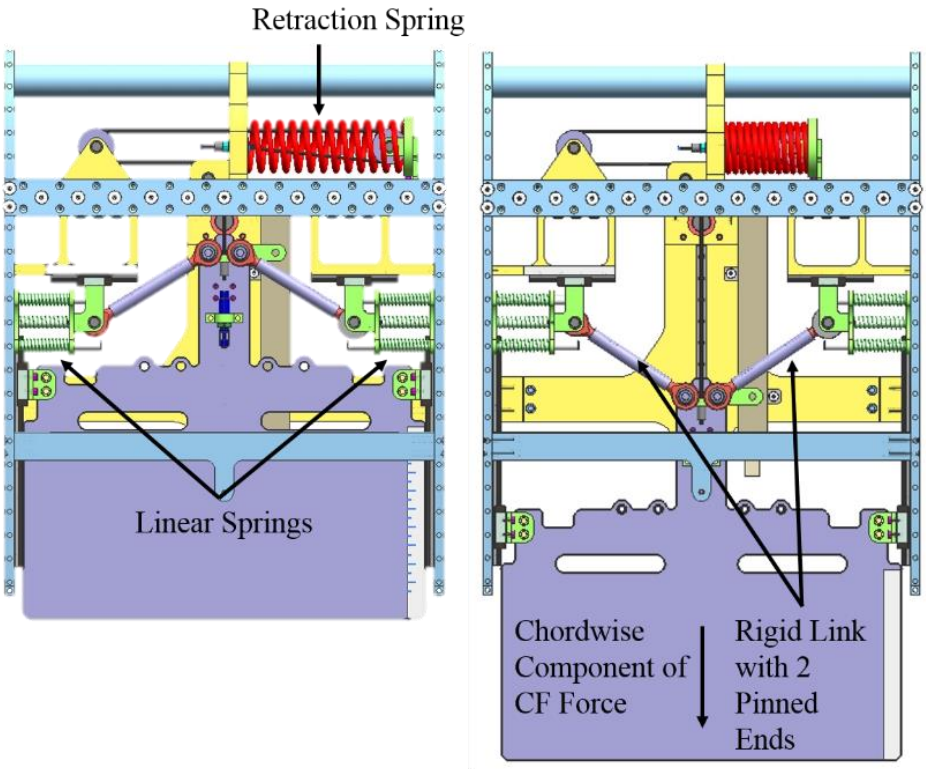

Fig. 2: Bi-stable chord morphing mechanism using Von Mises truss with rigid links (Ref. 15).

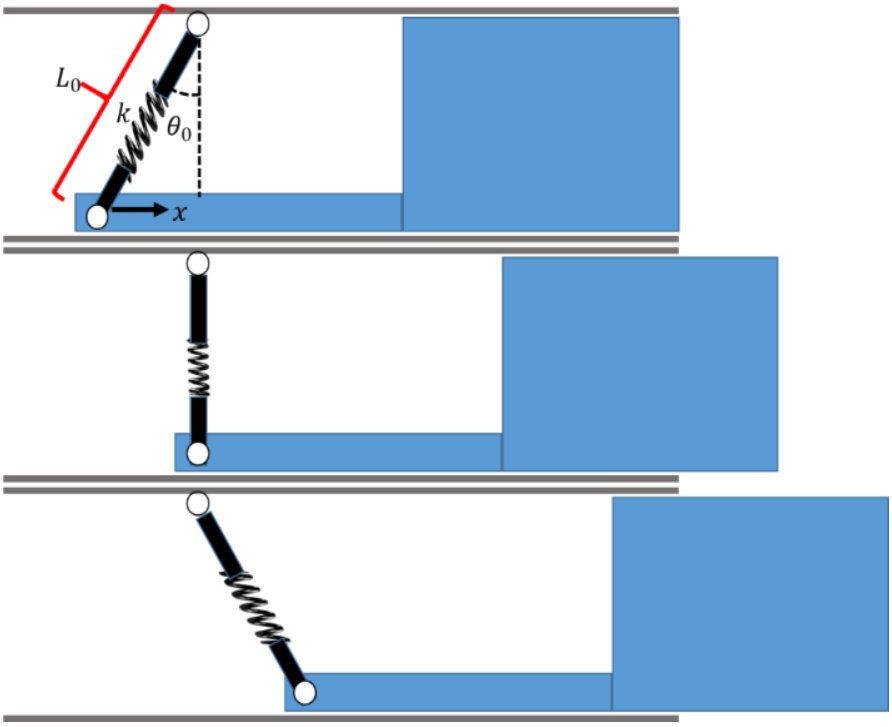

Fig.3: Schematic of bi-stable span morphing mechanism with half VMT.

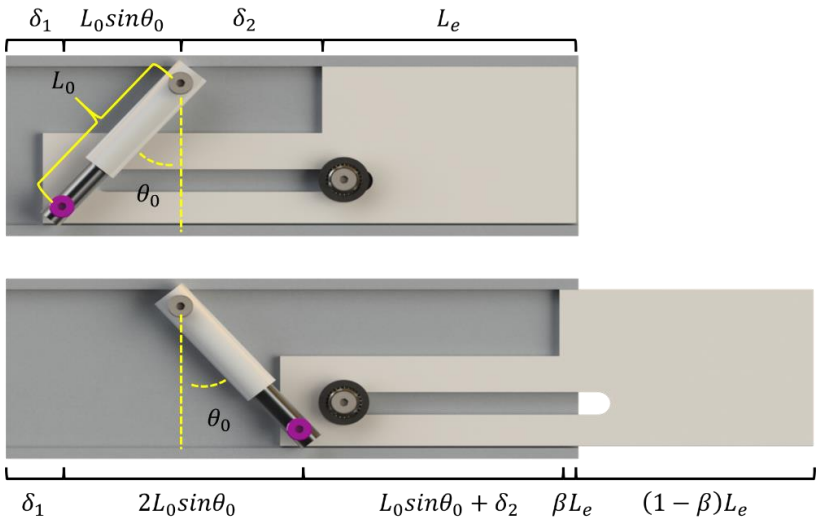

(A)

(B)

Fig. 4: Prototype rotor schematic with dimensions specified to describe the (A) retracted and (B) extended configurations.

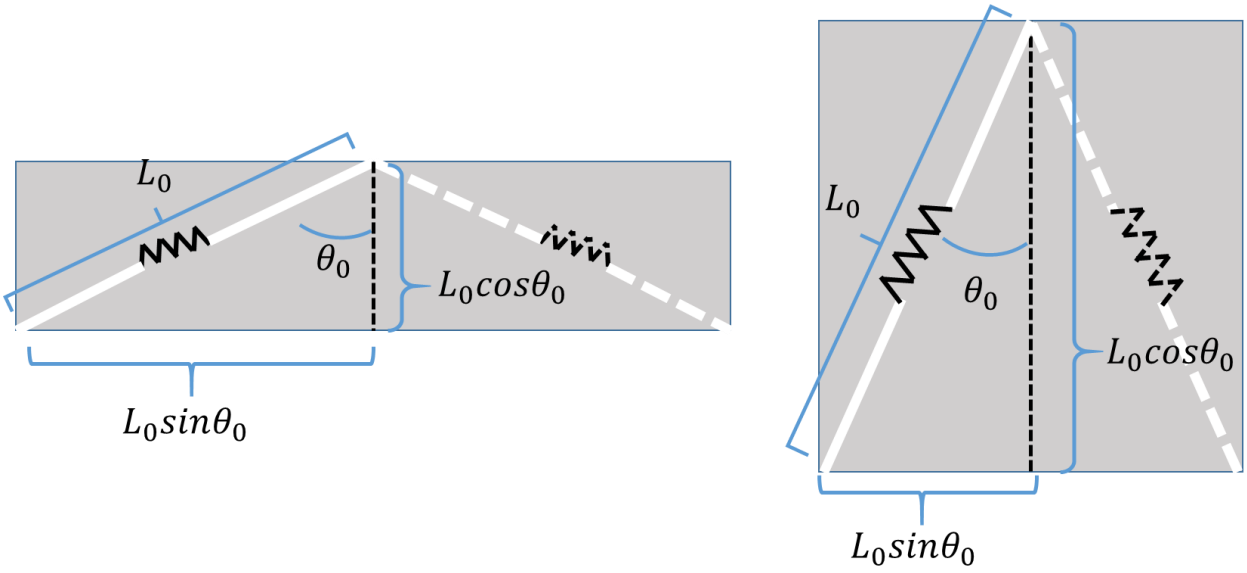

(A) (B)

Fig. 5: Relation of bi-stable mechanism stroke length to (A) internal spring strain and (B) channel width.

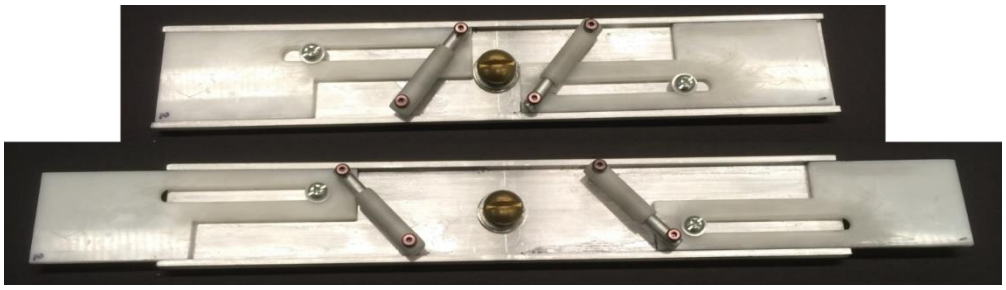

(A)

(B)

Fig. 6: Prototype rotor with inserts in the (A) retracted and (B) extended configuration.

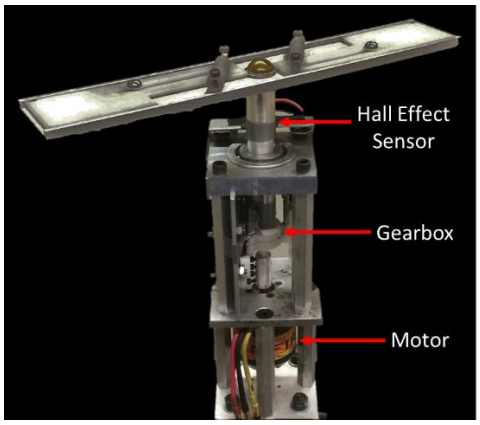

Fig. 7: Rotor test stand with motor, gearbox, RPM sensor, and prototype in compact configuration.

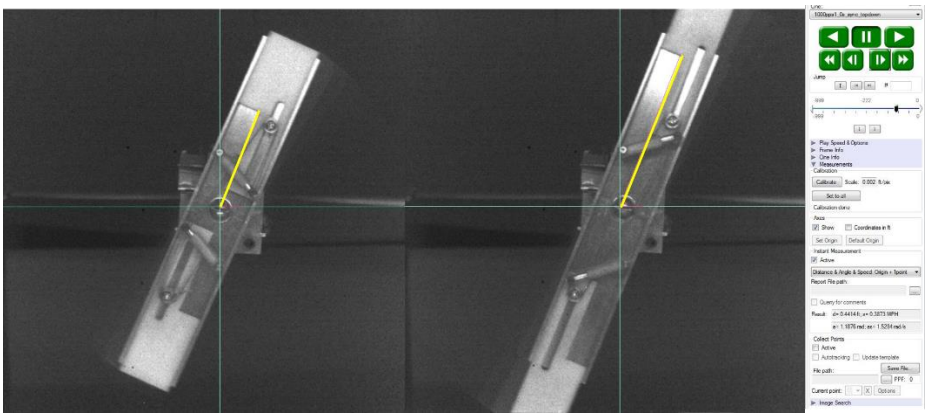

Fig. 8: Span extension measurements from position of insert in specific frames.

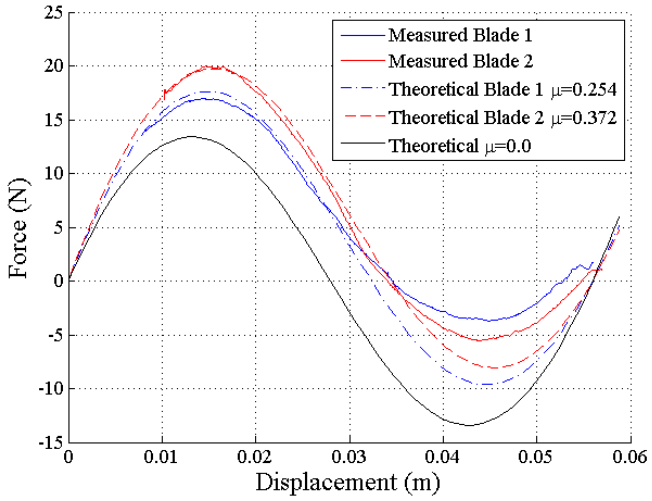

Fig. 9: Quasi-static force versus displacement behavior of the bi-stable mechanisms under displacement input.

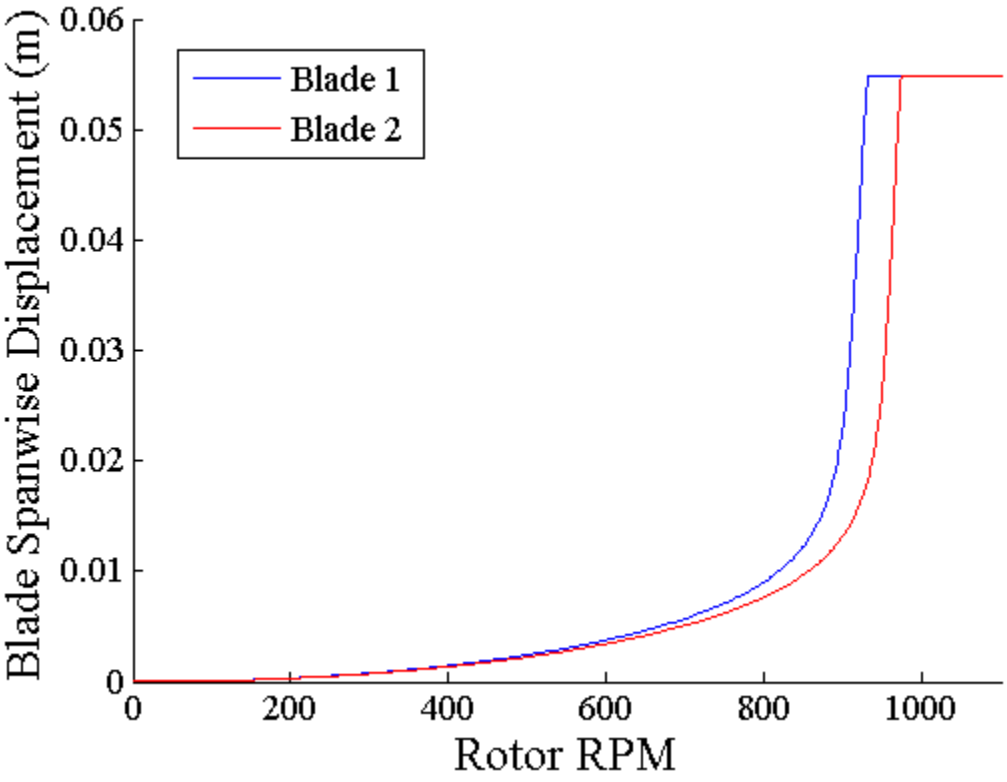

Fig. 10: Predicted extension of the two "blades" as a function of rotor RPM.

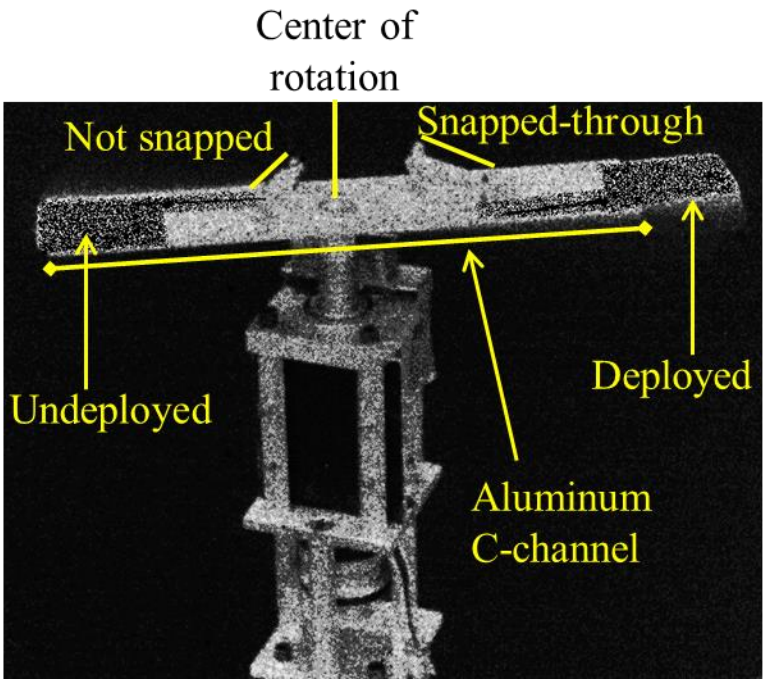

Fig. 11: High speed camera footage capturing asynchronous deployment.

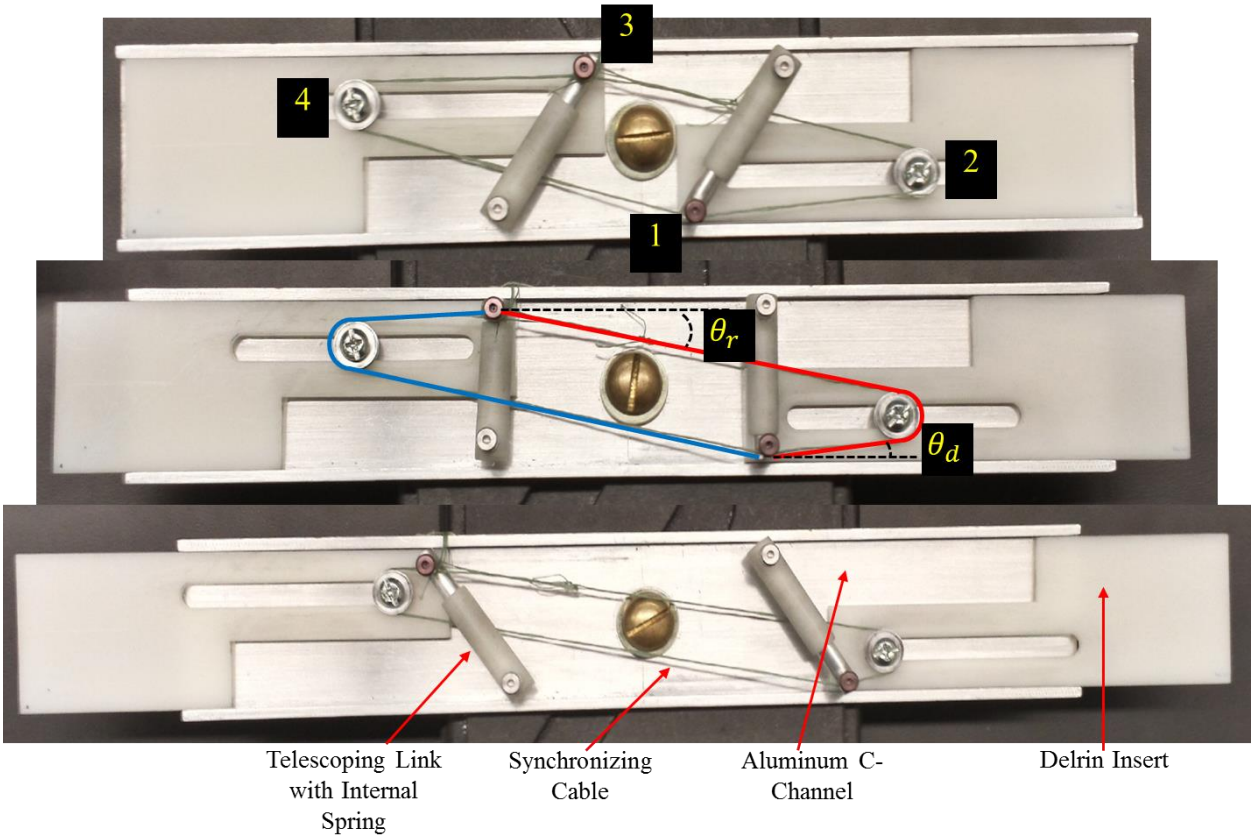

Fig. 12: Prototype with synchronizing cable in (a) retracted, (b) intermediate, and (c) extended configurations.

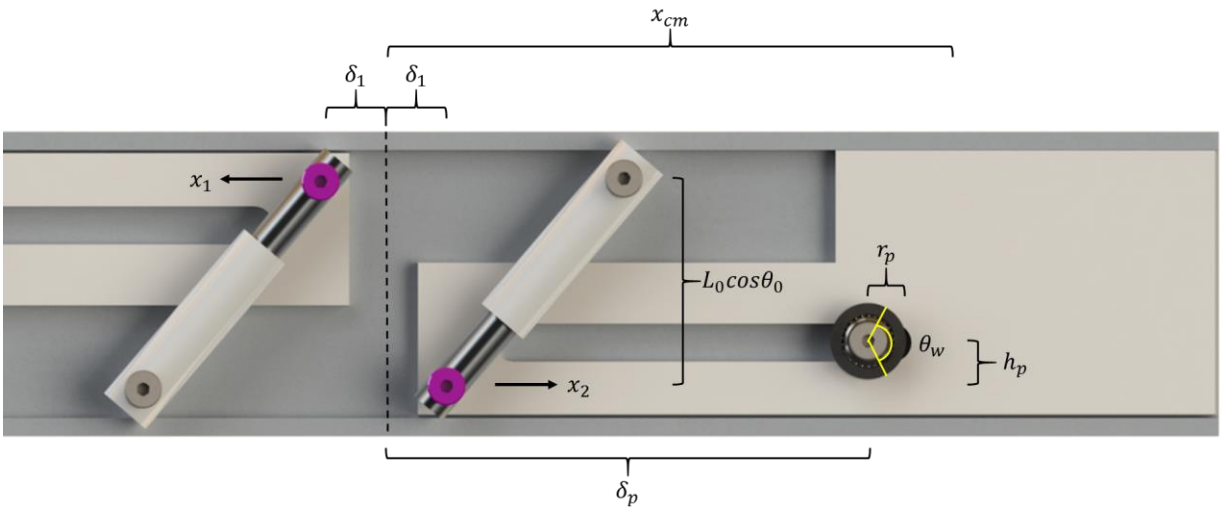

Fig. 13: Prototype rotor schematic with dimensions specified to calculate synchronizing cable length.

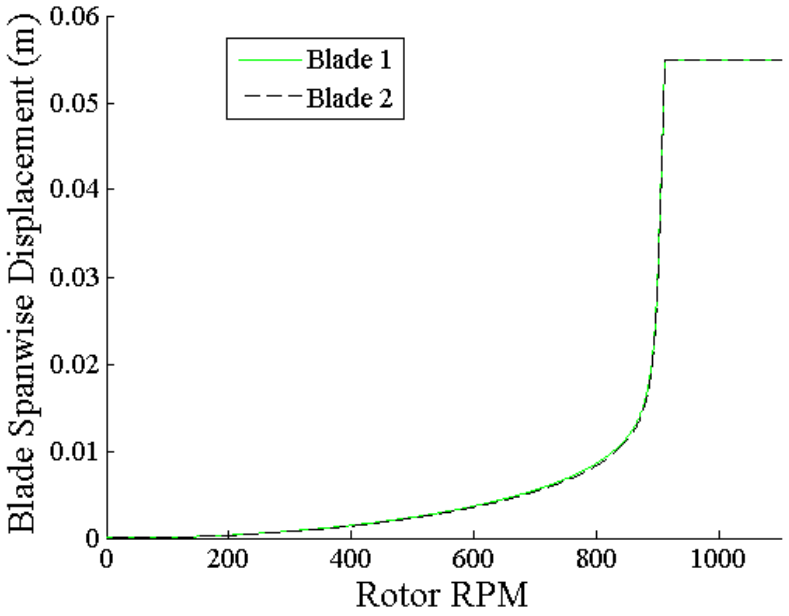

Fig. 14: Model prediction of synchronous extension of the two "blades" as a function of rotor RPM.

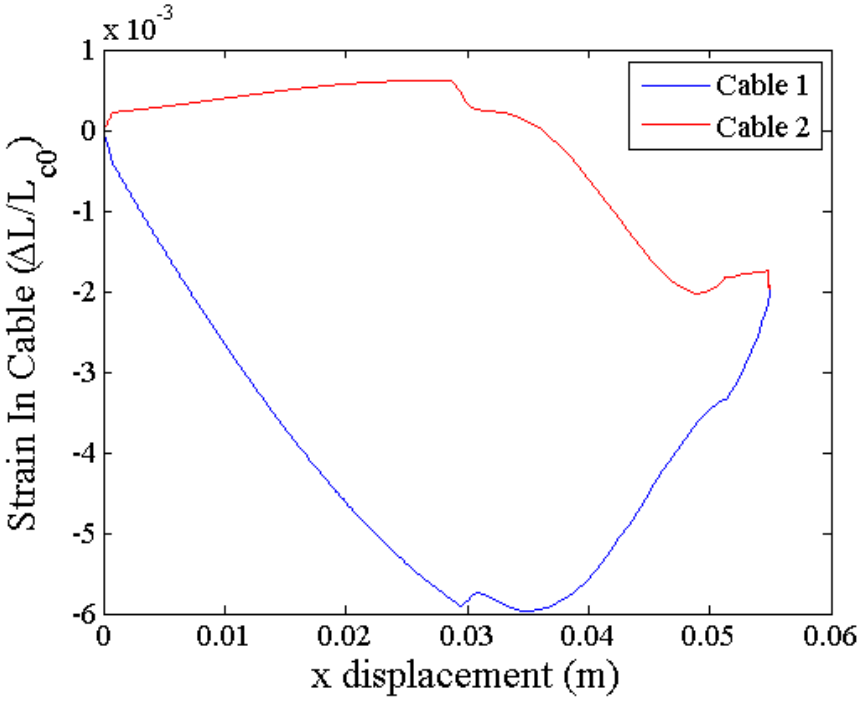

Fig. 15: Strain in the cables, as a function of blade extension.

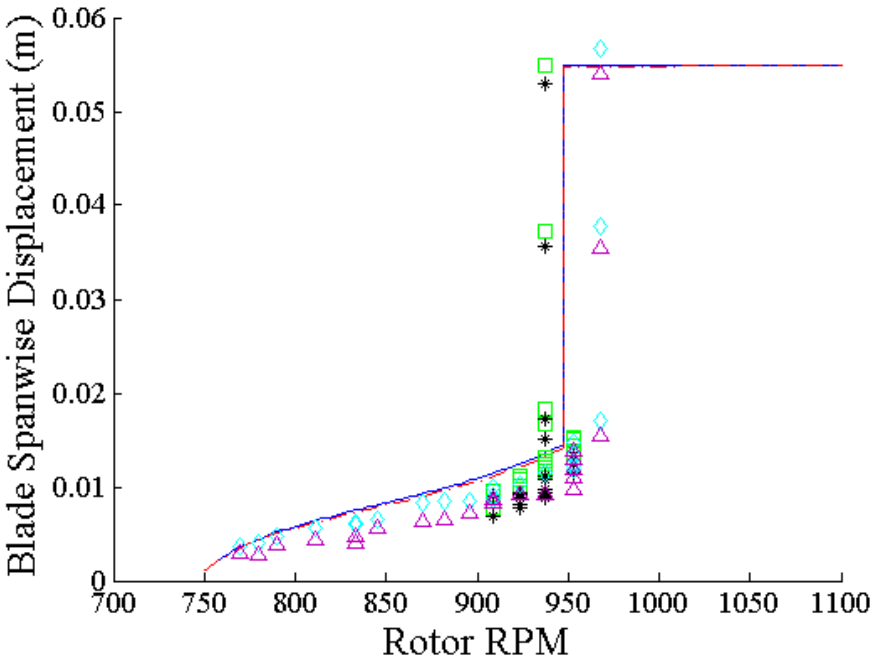

Fig. 16: High speed camera measurements of extension versus RPM, compared with simulation results.

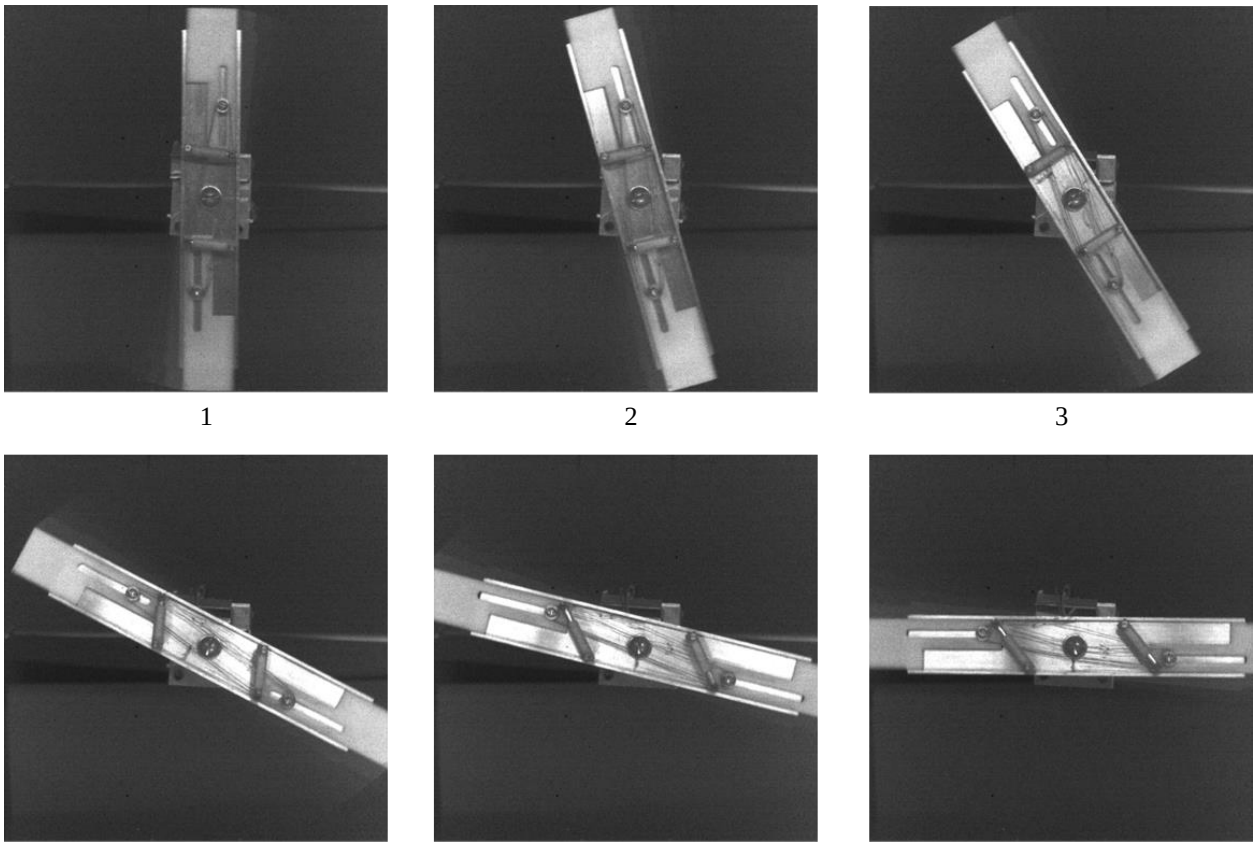

Fig. 17: Images of high-speed camera frames showing synchronous extension occurring over a ¼ revolution.

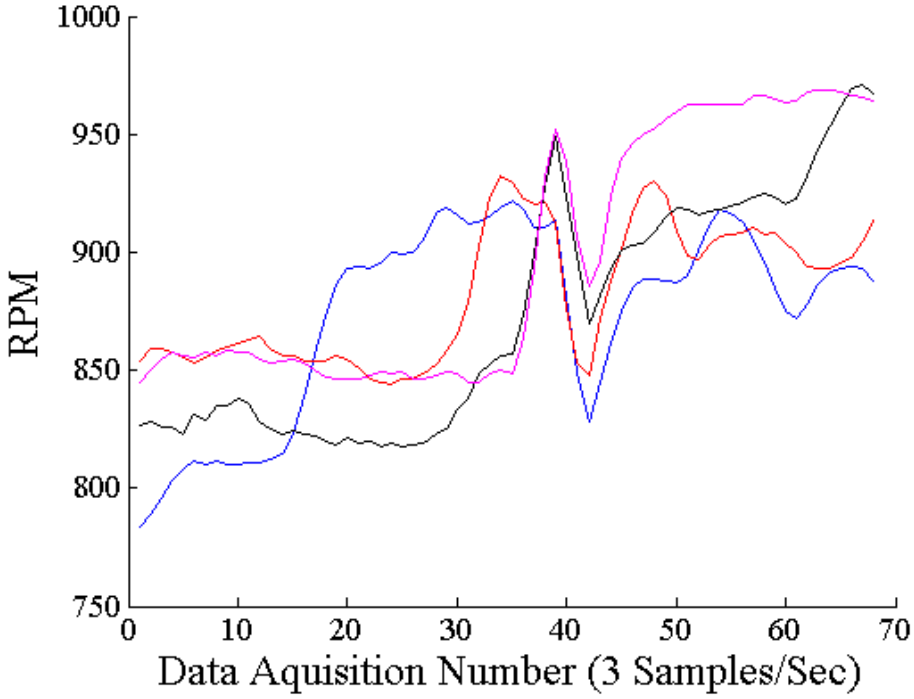

Fig. 18: Hall Effect sensor RPM data showing instantaneous change at snap-through.

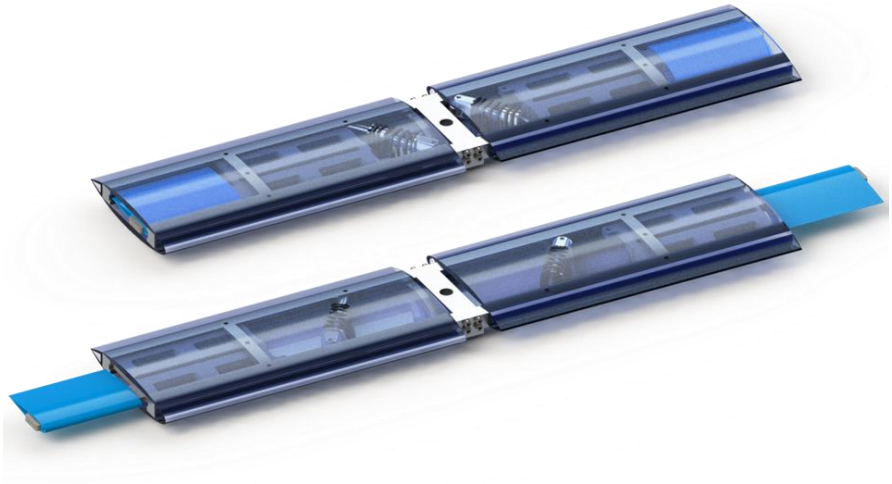

Fig. 19: Generation two span morphing rotor with aerodynamic surfaces

AFOSR Deliverables Submission Survey

Response ID:4575 Data

1.

1. Report Type

Final Report

Primary Contact E-mail
Contact email if there is a problem with the report.

dkm2@psu.edu

Primary Contact Phone Number
Contact phone number if there is a problem with the report

814-865-2560

Organization / Institution name

Pennsylvania State University

Grant/Contract Title
The full title of the funded effort.

Multi-Stable Morphing Cellular Structures

Grant/Contract Number
AFOSR assigned control number. It must begin with "FA9550" or "F49620" or "FA2386".

FA9550-11-1-0159

Principal Investigator Name
The full name of the principal investigator on the grant or contract.

Dennis McLaughlin

Program Manager
The AFOSR Program Manager currently assigned to the award

David Stargel

Reporting Period Start Date

08/15/2011

Reporting Period End Date

02/14/2015

Abstract

The first couple of years of the project focused primarily on three distinct areas. First, on experiments and numerical models toward a fundamental understanding of snap-through behavior of "cosine" arches. Second, on a demonstration of use of bi-stable elements in chord morphing applications. And third, on modeling an experiments focusing on the actuation of bi-stable von-Mises trusses using Shape Memory Alloys. Over the final phase, the project has focused on two specific areas. On the application side, a design of a span morphing system using bi-stable elements was developed, and demonstrated in an experiment. Furthermore, pneumatic artificial muscles were integrated in the unit cell of the cellular lattice for the purpose of modulus variation in one principle direction or another. Through analysis and experiment, the best unit cell geometric parameters that produced the largest change in modulus were identified. It was shown that maximum increase in modulus could be achieved by pressurizing either of the orthogonal muscle sets, rather than all the muscles simultaneously. The

difference in mechanism by which modulus change was realized when pressurizing one set of muscles, or the orthogonal set, were identified.

Distribution Statement
This is block 12 on the SF298 form.

Distribution A - Approved for Public Release

Explanation for Distribution Statement
If this is not approved for public release, please provide a short explanation. E.g., contains proprietary information.

SF298 Form
Please attach your SF298 form. A blank SF298 can be found here. Please do not password protect or secure the PDF The maximum file size for an SF298 is 50MB.

SF298 form filled.pdf

Upload the Report Document. File must be a PDF. Please do not password protect or secure the PDF . The maximum file size for the Report Document is 50MB.

AFOSR FA9550-11-1-0159 Final Report.pdf

Upload a Report Document, if any. The maximum file size for the Report Document is 50MB.

Archival Publications (published) during reporting period:

Pontecorvo, M., Barbarino, S., Murray, G., and Gandhi, F., "Bi-Stable Arches for Morphing Applications" Journal of Intelligent Material Systems and Structures, Vol. 24, No. 3, Feb 2013, DOI: 10.1177/ 1045389X12457252.

Moser, P., Barbarino, S., and Gandhi, F., "Helicopter Rotor Blade Chord Extension Morphing using a Centrifugally Actuated von-Mises Truss," Journal of Aircraft, Vol. 51, No. 5 (2014), pp. 1422-1431. doi: 10.2514/1.C032299.

Changes in research objectives (if any):

Change in AFOSR Program Manager, if any:

Extensions granted or milestones slipped, if any:

Original end-date was 08/14/2014. A 6-month no-cost extension was approved to allow completion of some span morphing work using bi-stable elements.

AFOSR LRIR Number

LRIR Title

Reporting Period

Laboratory Task Manager

Program Officer

Research Objectives

Technical Summary

Funding Summary by Cost Category (by FY, $K)

	Starting FY	FY+1	FY+2
Salary			
Equipment/Facilities			
Supplies			
Total			

Report Document

Report Document - Text Analysis

Report Document - Text Analysis

Appendix Documents

2. Thank You

E-mail user

May 13, 2015 17:41:40 Success: Email Sent to: dkm2@psu.edu